

TURBULENT PSEUDO-SOUND PRODUCTION IN
ATHEROSCLEROTIC ARTERIES

by

Jeffrey Joseph Fredberg

B.S.M.E., Tufts University
(1968)

S.M.M.E., Massachusetts Institute of Technology
(1970)

M.E., Massachusetts Institute of Technology
(1973)

SUBMITTED IN PARTIAL FULFILLMENT OF THE
REQUIREMENTS FOR THE DEGREE OF
DOCTOR OF PHILOSOPHY

at the

MASSACHUSETTS INSTITUTE OF TECHNOLOGY

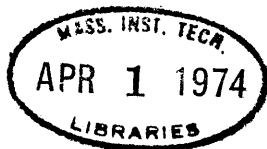
NOVEMBER 1973, *i.e. Feb. 1974*

Signature of Author.....*J.J.F.*.....

Certified by.....*[Signature]*.....

Accepted by.....*[Signature]*.....

Archives



TURBULENT PSEUDO-SOUND PRODUCTION IN
ATHEROSCLEROTIC ARTERIES

by

Jeffrey Joseph Fredberg

Submitted to the Department of Mechanical Engineering
in November, 1973, in partial fulfillment of the
requirements for the degree of Doctor of Philosophy.

ABSTRACT

Sounds and murmurs have long been employed for qualitative diagnosis of cardiovascular disease. However, quantitative diagnosis has been hindered by the lack of understanding of the mechanisms of sound generation and transmission in the human circulation. Clinical phonoangiographic studies have shown that simple assumptions about low frequency sound transmission through tissue surrounding an artery are inadequate for obtaining meaningful quantitative diagnosis. Therefore, a theory is developed which relates internal turbulent flow in diseased peripheral arteries to the tissue vibration observed at the surface of the skin by means of assumptions of similarity and local axial homogeneity of the internal turbulence. It is found that the spectrum of pressure at the wall of the artery is related to the spectrum of the pressure at a no-displacement surface by a filtering factor approximately proportional to ω^{-2} . This arises not because of frequency-dependent volumetric absorption in the surrounding medium, as with ultrasound, but

because of the manner in which stochastic signals add when observed.

In addition, the structure of the turbulent pressure field at the wall of a rigid tube downstream of an orifice was studied. Dependence of mean square pressure and spectral density of pressure at the wall upon Reynolds number and diameter ratio was studied in the ranges of physiological interest. It was found that the mean square pressure has very strong Reynolds number dependence at low Reynolds number, and that spectral density can be expressed as a one parameter (modified Reynolds number) family of curves.

Thesis Supervisor: C. Forbes Dewey, Jr.

Title: Associate Professor of Mechanical Engineering

Acknowledgements

I am deeply indebted to the many people who made the completion of this work possible by their help, suggestions, and encouragement.

My sincere appreciation is extended to Professor C. Forbes Dewey, Jr. for his sincere interest and enthusiasm in the research, and for the direction he provided.

I am also grateful to the other members of the thesis committee, Professors David Hault, Robert Lees, and Richard Lyon for their interest and guidance.

Professors Huw Davies and Erik Mollo-Christensen also provided insights helpful in the development of the theory.

Much gratitude is extended to my associates in the Fluid Mechanics Laboratory who provided a sounding board for ideas as well as helpful suggestions.

Victor Nedzilnitsky of M.I.T.'s Eaton Peabody Laboratory provided invaluable assistance in the transducer calibration procedure.

To my wife, Ellen, son, Joshua, and daughter, Sheryl, I owe a special note of thanks for the inspiration they provided and understanding they showed.

This research was supported by in part by grants from the National Heart and Lung Institute, Grant No. 14209, and the National Dairy Council.

TABLE OF CONTENTS

	Page Number
Title Page-----	1
Abstract-----	2
Acknowledgements-----	4
Table of Contents-----	5
List of Figures-----	7
Nomenclature-----	9
I. Introduction-----	11
II. Theory of Pseudo-Sound Transmission in Tissue-----	20
III. The Experiment-----	36
3.1 Experimental Objectives-----	36
3.2 Similarity Considerations-----	37
3.3 The Fluid Loop-----	46
3.4 The Pressure Transducer-----	54
3.5 Artifact Checks-----	64
3.6 Viscosity-Temperature Calibration-----	65
3.7 Data Collection and Processing-----	66
3.8 Previous Investigations-----	71
IV. Experimental Results-----	77
4.1 Normalization of RMS Data-----	77
4.2 Normalization of Spectral Data-----	84
4.3 Interpretation of Experimental Results-----	97
V. Conclusions-----	102
5.1 Implications for Phonoangiography-----	102
5.2 Onset of Vascular Murmurs-----	111
5.3 Estimate of Mean Square Shear Stress at Arterial Wall-----	112

References-----	114
Appendix A: Exact Solution for Cylinder of Finite Diameter-----	119
Appendix B: Effect of Transducer Size at the Skin Surface-----	122
Appendix C: Formulation of Phonoangiographic Equations-----	127

LIST OF FIGURES

	Page
Fig. 1. Idealized representation of a peripheral stenosed artery below the surface of the skin.	13
Fig. 2. Spectral density of force induced in a stationary transducer at the skin surface over a stenosed carotid artery.	16
Fig. 3. Generalized source region in infinite space.	24
Fig. 4. Artery modelled as a line source of excitation.	26
Fig. 5. A typical space-time correlation.	29
Fig. 6. Intensity integral I for $X/L = 1$.	33
Fig. 7. Idealized geometry of a stenosed artery.	38
Fig. 8. Velocity profile for inviscid flow through a converging channel.	41
Fig. 9. The experimental fluid loop.	47
Fig. 10. Electrical analog of fluid loop.	48
Fig. 11. Mounting of the stenosis in the test section.	50
Fig. 12. Stenosis dimensions.	51
Fig. 13. Pump calibration.	53
Fig. 14. Diagram of pressure sensor.	55
Fig. 15. Transducer calibration procedure.	60
Fig. 16. Transducer calibration.	62
Fig. 17. Transducer mounting in the test section.	63
Fig. 18. Temperature-viscosity relations for the working fluids.	66
Fig. 19. Data processing scheme.	67
Fig. 20. Output voltage of tape recorder divided by input voltage to first (variable gain) preamplifier.	69
Fig. 21. Rms wall pressure vs. downstream distance with 55% area reduction.	78
Fig. 22. Rms wall pressure vs. downstream distance with 64% area reduction.	79
Fig. 23. Rms wall pressure vs. downstream distance with 73% area reduction.	80

Fig. 24.	Rms wall pressure vs. downstream distance with 82% area reduction.	81
Fig. 25.	Rms wall pressure vs. downstream distance with 91% area reduction.	82
Fig. 26.	Spatial maximum of rms wall pressure vs. jet Reynolds number and area reduction.	83
Fig. 27.	Spatial maximum of rms wall pressure vs. modified Reynolds number.	85
Fig. 28.	Distance downstream of orifice at which spatial maximum of rms wall pressure is attained, vs. jet Reynolds number.	86
Fig. 29.	Nondimensional spectral density of wall pressure for 55% area reduction.	87
Fig. 30.	Nondimensional spectral density of wall pressure for 64% area reduction.	88
Fig. 31.	Nondimensional spectral density of wall pressure for 73% area reduction.	89
Fig. 32.	Nondimensional spectral density of wall pressure for 82% area reduction.	90
Fig. 33.	Nondimensional spectral density of wall pressure for 91% area reduction.	91
Fig. 34.	Nondimensional spectral density of wall pressure for all area reductions at high Reynolds number.	93
Fig. 35.	A family of curves representing spectral density of wall pressure at low Reynolds number.	96
Fig. 36.	Distance downstream of orifice at which spatial maximum of rms wall pressure is observed.	99
Fig. 37.	Idealized model of spectral density of a bruit.	106
Fig. 38.	Excitation of a finite transducer by a source region.	123

NOMENCLATURE

a	radius of curvature of a stenosis at minimum cross-section (cm)
$B(\underline{x}, \tau)$	autocorrelation of pressure at the observer ($\text{dynes}^2/\text{cm}^4$)
c	speed of sound in tissue (cm/sec)
d	orifice diameter (cm)
D	arterial diameter (cm)
$E(\omega)$	Spectral density of pressure at the arterial wall ($\frac{\text{dyne}^2 \text{sec}}{\text{cm}^4}$)
$\tilde{E}(f)$	$(E(\omega)/P^2)(U/d)$ nondimensional spectral density of pressure
\tilde{f}	fd/U
$f_i(\underline{x}, t)$	external force/volume (dynes/cm^3)
H	depth of artery beneath skin
l	longitudinal correlation length (cm)
L	characteristic length of turbulent jet
P_{rms}	root mean square wall pressure (dynes/cm^2)
$P(\underline{x}, t)$	average normal stress (dynes/cm^2)
$R(\Delta, \tau)$	homogeneous space-time correlation ($\text{dynes}^2/\text{cm}^2$)
Re	Reynolds number = UD/ν
Re_j	jet Reynolds number $u_j d/\nu$
\tilde{Re}	modified Reynolds number $Re_j (D/d)^{1.5}$
U	mean flow in unobstructed portion of pipe
U_c	convection velocity (cm/sec)
$\xi_i(\underline{x}, \tau)$	displacement (cm)
u_j	jet velocity (cm/sec)

$W(y_1, z_1)$	weighting function (dimensionless)
\underline{x}	position vector (cm)
$\underline{y}, \underline{z}$	dummy position variables (cm)
α	scale of $W(\text{cm}^{-1})$
η	lateral correlation length (cm)
Δ	$y_1 - z_1$ (cm)
θ_i, θ'_i	direction cosines
λ	wavelength (cm)
$\hat{\lambda} \hat{\mu}$	Lame's constants
$\pi(\underline{x}, \omega)$	pressure spectral density at observer ($\frac{\text{dyne}^2 \text{sec}}{\text{cm}^4}$)
ρ	density (gr/cm^3)
τ	time difference (sec)
$\phi(\omega)$	force spectral density on line source ($\frac{\text{dyne}^2 \text{sec}}{\text{cm}^2}$)
ω	frequency (radians/sec)
$\langle \quad \rangle$	ensemble average

Chapter I. Introduction

Arteriosclerosis is a term applied to a number of conditions in which there is general hardening and thickening of the arteries. Atherosclerosis is a form of arteriosclerosis in which there are localized accumulations of material within or beneath the intimal, or inner surface of the arteries. Over a period of years these deposits become calcified atherosclerotic plaques which can severely compromise the arterial diameter. Substantial evidence also exists that the plaques are susceptible to hemorrhage and local thrombosis.

Atherosclerotic deposits are found throughout the human arterial tree, and although the mechanisms by which these deposits are formed remain unidentified, it is known that there are particular regions of the arterial tree which are predisposed to becoming sclerotic, including the coronary arteries, the bifurcation of the aorta at the iliac arteries, the carotids, and the femorals to mention a few.

Most commonly this condition is diagnosed by a method known as X-ray angiography, which involves insertion of a catheter into the artery of interest. X-ray opaque dye is released through the catheter and X-ray cinematography is used to map the arterial lumen and the perfusion of the subject vessel. However, this procedure has a significant risk of morbidity and is non-trivial to perform (Willcutt, 1968). It is therefore of substantial interest to develop noninvasive methods of diagnosing the disease when clinically evident and perhaps more important, in the case of subclinical disease, when angiography may not be warranted. A complete

diagnosis is taken to be the prediction of flow rate through the artery as well as the degree to which the lumen is occluded.

The stenosis can be thought of as a converging-diverging nozzle, or an orifice, (Fig. 1). During systole, the blood immediately proximal to the stenosis undergoes a rapid convective acceleration as it passes from the unobstructed portion of the artery through the converging section of stenosis. At the point of smallest cross-sectional area the mean flow velocity is a maximum, and the hydrostatic pressure is a minimum. As the flow passes through the diverging section of the stenosis the flow separates from the walls due to its inability to overcome the adverse pressure gradient. At the boundary between the high velocity separated jet and the slower moving fluid in the recirculating separation zone, a shear layer is created which is susceptible to shear instabilities. This shear layer provides a source from which these instabilities can extract energy from the mean flow.

This energy extraction process proceeds at a sufficiently rapid rate that before systole has ended the instabilities break down into fully turbulent motion provided the jet Reynolds number is high enough (the jet Reynolds number is $Re_j = \frac{u_j d}{\nu}$, where u_j = mean jet velocity, d = jet diameter, ν = kinematic viscosity of the fluid. Smith et al (1972) has observed turbulence in blood distal to stenosis at jet Reynolds numbers as low as 450). The turbulence continues to extract energy from the mean flow as the jet expands to fill the artery. Once the jet fills the artery the turbulence is no longer able to sustain itself by extraction of energy

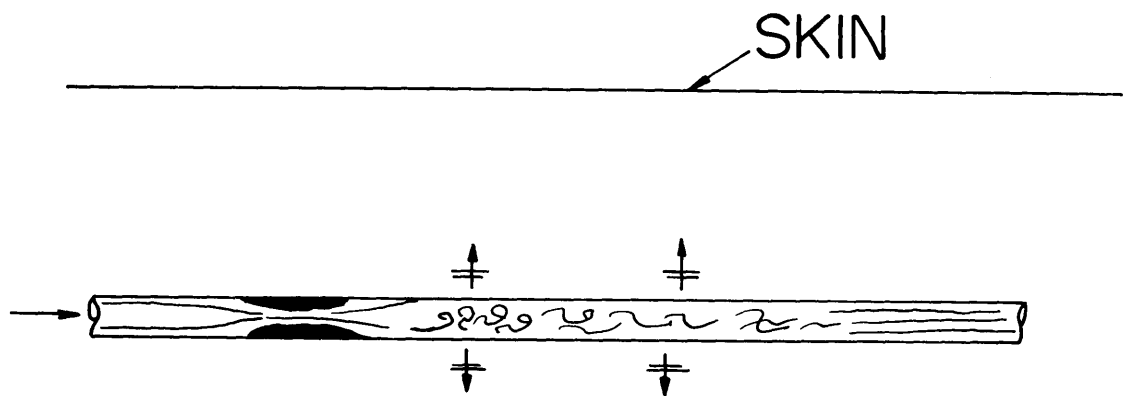


Fig. 1. Idealized representation of a peripheral stenosed artery below the surface of the skin.

from the mean flow because the artery Reynolds number ($Re = Re_j \frac{d}{D} < 1000$) is typically below the critical Reynolds number necessary to achieve sustained turbulent flow in a straight pipe ($Re \approx 2000$). At this point inertial mixing processes dominate the production of turbulent energy and the turbulent intensity rapidly decays.

Between the stenosis and the region where turbulence has significantly decayed, the turbulent intensities can be quite large, and the wall of the artery can be subjected to large fluctuating stresses imposed by the turbulent flow.

It has long been known that systolic "sounds", or more accurately, tissue vibrations, are often generated by the fluctuating wall stress at the site of these partial occlusions, and can be detected at the surface of the skin with an ordinary stethoscope (McKusick, 1954). It was the hypothesis of Lees and Dewey (1970) that since the quantitative nature of these sounds (bruits in medical parlance) must be dependent upon the local flow physics and local geometries at the site of these occlusions, one might be able to recover the parameters of interest by quantitative analysis of these "sounds" utilizing a first principles cause-and-effect relationship.

Traces of the voltage time output of a pressure transducer at the skin surface near an arterial stenosis are presented by Klitzner (1972). The onset of the bruit is characterized by a deterministic (reproducible from beat to beat) signature for the first 10 to 20% of systole. At that time the signal becomes stochastic in nature, with a characteristic crescendo-descrescendo intensity time profile. During diastole the signal

is dominated by ambient noise not radiating from the artery. For further description of bruits and the transduction process, see Klitzner (1972). The spectral content of a typical bruit recorded at the skin surface at peak systole is shown in Fig. 2.

In vivo studies correlating the power spectra of pressure fluctuations at the surface of the skin with wall pressure fluctuations in a fully turbulent pipe flow at high Reynolds number demonstrated remarkable similarities (Lees and Dewey, 1970; Fredberg, 1970).

A discussion of turbulence in arteries and the methods by which information can be extracted from the sounds they generate is given by Lees and Dewey (1970). McDonald (1960) and McKusick (1958) also discuss the origins and diagnostic techniques of cardiovascular sounds and murmurs. However, the physical mechanism by which the tissue vibration at the surface of the skin is related to the internal turbulent flow has been poorly understood.

Clinically, and with dog experiments, Gurll (to be published) has in large confirmed the scaling laws derived by Lees and Dewey (1970). However, predictions of the flow rate, carried out as prescribed by Lees and Dewey (1970), were consistently low by a factor of two to four. It was this curious result which threw into question the assumptions of Lees and Dewey (1970) that a) the spectral distribution of energy remained unchanged in transmission through the interlying tissue; b) that a constant fraction of jet kinetic energy is converted into turbulence independent of Reynolds number c) that the structure of the turbulent pressure field was essentially the same as in fully turbulent pipe flow.

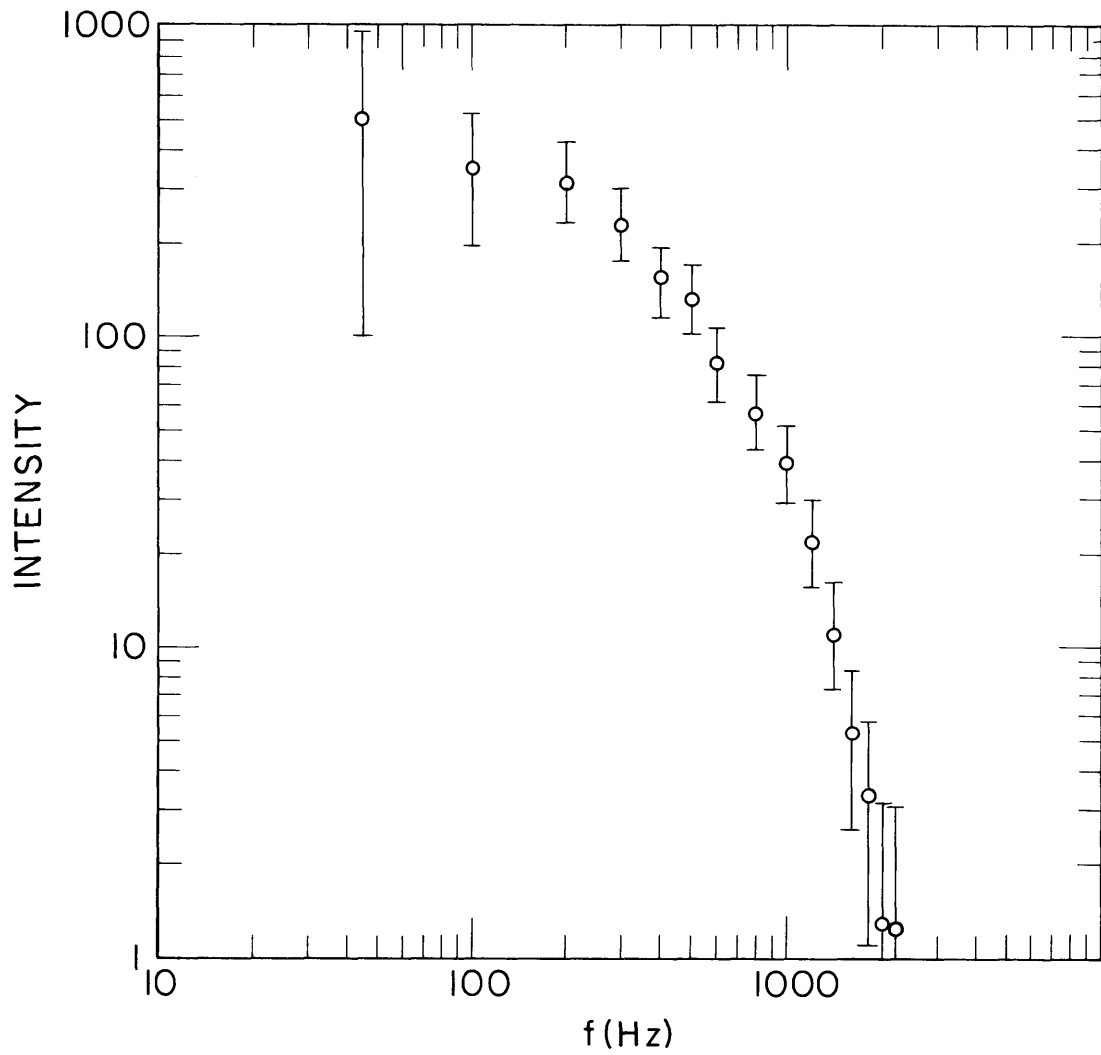


Fig.2. Spectral density of force induced in a stationary transducer at the skin surface over a stenosed carotid artery.

It is the objective of Chapter II to study the physics of transmission of these "sounds" from the arterial wall through the surrounding tissue to the surface of the skin in order to clarify the ambiguities of interpreting data obtained in vivo. While leaving the statistical description of the turbulent pressure field as general as possible (i.e. without describing the power spectral density of pressure at the arterial wall, $E(\omega)$, in terms of flow parameters) it is intended to derive a functional relationship between $E(\omega)$ and $\pi(\underline{x},\omega)$, the spectral density of pressure at the observer point \underline{x} , thus relating the physiological observable $\pi(\underline{x},\omega)$ with the desired unknown $E(\omega)$. A result of particular importance is that the disturbances observed at the surface of the skin have much lower amplitude high frequency components than the turbulent fluctuations themselves. This high frequency attenuation is not to be confused with volumetric absorption in the interlying tissue, as is the case in ultrasound, but is caused by the manner in which stochastic signals add when observed. (In the frequency range of interest for phonoangiography (< 1000 Hz), volumetric absorption is negligible.) The effect predicted in Chapter II reduces the error found by Gurll to within his scatter.

Sections III and IV report the procedure and results of an experiment whose objective was to study the structure of the turbulent pressure field at the wall downstream of a constriction. The principal objectives of this experiment were to investigate the spatial dependence of the mean square pressure at the wall and to obtain a universal description of the spectral density of pressure at the wall as degree of obstruction and Reynolds number vary.

Section IV includes an interpretation of the experimental results of Section III, while Section V includes a summary and discussion of the implications of present findings upon the clinical phonoangiographic procedure.

Chapter II. Theory of Pseudo-Sound Transmission in Tissue

The problem of relating the quantitative nature of the tissue vibrations at the skin surface with the flow parameters of interest, such as obstructed diameter and flow rate, requires 1) the knowledge of the stress field imposed on the wall by the turbulent flow, and 2) how this stress field is transmitted to the skin surface. The first of these subjects is discussed in later chapters dealing with the experiments which were performed. The second subject is discussed in this chapter. The objective of this chapter is to develop a theory which relates the stress at a point at the skin surface constrained to no displacement with the turbulent stress field at the wall of a diseased artery. With a very simple physical model it is found that strong filtering occurs in transmission of the stress field due to the stochastic nature of turbulent excitation.

Procedure

In order to make the direction of the derivation clear, a brief summary of the model and the principle assumptions is presented here.

The tissue surrounding the artery is modelled as an extended isotropic elastic medium in which the turbulent pressure field is represented as a distributed source of force (Eq. 2.1). Noting that in the relevant frequency range the wavelengths are long compared to other characteristic lengths, the tissue can be treated as a stiffness-controlled medium (Eq. 2.10) in which inertial forces (time derivatives) are negligible.

Representation of the source as a line distribution (Eq. 2.14), assumption of similarity (Eq. 2.17), and small correlation length of the

turbulent field (Eq. 2.24) permits the reduction of a sixfold frequency-dependent integral (Eq. 2.13) to a single frequency-independent geometrical integral (Eq. 2.22). The final result (Eq. 2.23) provides the desired relationship.

Model

It is assumed that the origin of the bruit is a time stationary turbulent pressure field at the wall of the artery. Because the turbulent time scale is much less than systolic time scale the flow can be assumed to be quasi-steady at systole (see Section III.2). The artery is modelled as a source region imbedded in a homogeneous, isotropic, elastic medium. At a cross-section of an artery with internal turbulent flow, the pressure at the wall is not well correlated over the circumference. For simplicity, one can replace this circumferential pressure distribution by the resultant force. This resultant force will be a random function of time, and extending this idea, we replace the artery by a line source of forces.

It is further assumed that the turbulent field, while it is the source that excites the surrounding elastic medium, is not coupled to its motion; i.e., the fluid motion within the artery is not significantly effected by motion of the arterial wall.

Equations of Motion

Newton's law for a homogeneous isotropic elastic (non-absorbing) medium with infinitesimal strains is expressed by Navier's equation (e.g. Fung, 1965)

$$\hat{\mu} \frac{\partial^2 \xi_i}{\partial x_j \partial x_j} + (\hat{\mu} + \hat{\lambda}) \frac{\partial^2 \xi_m}{\partial x_m \partial x_i} + f_i = \rho \frac{\partial^2 \xi_i}{\partial t^2} \quad (2.1)$$

where $\xi_i(\underline{x}, t)$ are displacements $\hat{\lambda}$ and $\hat{\mu}$ are Lamé's constants, ρ is the material density, and $f_i(\underline{x}, t)$ are the external forces.[†] From the divergence of (2.1) one obtains the dilatational wave equation,

$$\frac{1}{c^2} \frac{\partial^2 \epsilon}{\partial t^2} - \frac{\partial^2 \epsilon}{\partial x_i \partial x_i} = \frac{1}{2\hat{\mu} + \hat{\lambda}} \frac{\partial f_i}{\partial x_i} \quad (2.2)$$

where

$$\epsilon = \frac{\partial \xi_i}{\partial x_i} \quad (2.3)$$

$$c^2 = \frac{2\hat{\mu} + \hat{\lambda}}{\rho} \quad (2.4)$$

The stress in this system is given by

$$\sigma_{ij} = 2\hat{\mu} \epsilon_{ij} + \hat{\lambda} \delta_{ij} \epsilon_{kk} \quad (2.5)$$

where ϵ_{ij} is the strain tensor

$$\epsilon_{ij} = \frac{1}{2} \left[\frac{\partial \xi_i}{\partial x_j} + \frac{\partial \xi_j}{\partial x_i} \right] \quad (2.6)$$

Using (2.5) and (2.6) one can rewrite (2.2) in terms of the average normal stress P ,

$$\frac{1}{c^2} \frac{\partial^2 P}{\partial t^2} - \frac{\partial^2 P}{\partial x_i \partial x_i} = \frac{1}{3} \left(\frac{2\hat{\mu} + 3\hat{\lambda}}{2\hat{\mu} + \hat{\lambda}} \right) \frac{\partial f_i}{\partial x_i} \quad (2.7)$$

[†] The summation convention for repeated indices is used here.

where

$$P = \frac{\sigma_{\ell\ell}}{3} = \frac{\epsilon(2\hat{\mu} + 3\hat{\lambda})}{3} \quad (2.8)$$

Consider a source region in an infinite medium. If H is a typical dimension from the observer to the source, and λ is a typical wavelength then

$$\frac{\partial^2 P}{\partial x_i \partial x_i} - \frac{1}{c^2} \frac{\partial^2 P}{\partial t^2} = O\left(\frac{\lambda^2}{H^2}\right) \quad (2.9)$$

In this case $\lambda^2/H^2 \gg 1$, so (2.8) can be rewritten as the near field approximation**

$$-\frac{\partial^2 P}{\partial x_i \partial x_i}(\underline{x}, t) = \frac{1}{3} \left(\frac{2\hat{\mu} + 3\hat{\lambda}}{2\hat{\mu} + \hat{\lambda}} \right) \frac{\partial f_i}{\partial x_i}(\underline{x}, t) \quad (2.10)$$

In the near field of the source (much closer than one wavelength) the dilatational propagation speed appears infinite, and therefore the material behaves as an incompressible medium. The kinetic energy in the near field is "attached" to the source and cannot propagate because the near field pressure and velocity are always out of phase; this guarantees zero net energy flux through any closed surface surrounding the source.

Because near-field pressure fluctuations cannot propagate (Eq. 2.10 is elliptic) we refer to these sounds as pseudo-sounds.

Boundary Conditions

A typical geometry for a carotid or femoral artery is depicted in

** Most of the energy in bruits is contained below 1000 Hz, which would correspond to a minimum wavelength the order of a meter.

Fig. 1. A pressure transducer is mounted in a rigid plate in contact with the skin. Thus, the boundary condition at the skin-plate interface will be $\xi = 0$, no displacement.* If the curvature of the plate is small, the method of images can be employed with the no-displacement boundary condition to create an image source. Thus the problem can be treated as two symmetrical (about the rigid boundary) sources in an infinite medium. This will lead to pressure doubling at the skin surface.

Solution

The Green's function associated with Poisson's equation in infinite space is $(4\pi|\underline{x} - \underline{y}|)^{-1}$ (Garabedian, 1967). Therefore, in the geometry depicted in Fig. 3 the general solution to Eq. (2.10) is given by

$$P(\underline{x}, t) = \hat{E} \int_{-\infty}^{\infty} \frac{\partial f_i / \partial y_i (\underline{y}, t)}{|\underline{x} - \underline{y}|} d\underline{y} \quad (2.11)$$

where

$$\hat{E} = \frac{1}{12\pi} \left(\frac{2\hat{\mu} + 3\hat{\lambda}}{2\hat{\mu} + \hat{\lambda}} \right)$$

and the integral (2.11) extends over three dimensions. The function f now represents the original source, and its image source. Equivalently, integration by parts of (2.11) yields

$$P(\underline{x}, t) = \hat{E} \int_{-\infty}^{\infty} \frac{\cos \theta_i f_i (\underline{y}, t)}{r^2} d\underline{y} \quad (2.12)$$

* This is somewhat arbitrary, depending upon measuring device, e.g., a pressure transducer with no displacement, or a displacement transducer with a pressure release condition. Klitzner (1972) demonstrated that a Hewlett-Packard 2050 heart sounds microphone (piezo-electric) in contact with the skin provided a no displacement boundary condition due to the large mechanical impedance of the microphone compared with the tissue impedance. Thus while the skin is usually thought of as a pressure release surface, a force is induced at the surface by a stationary transducer.

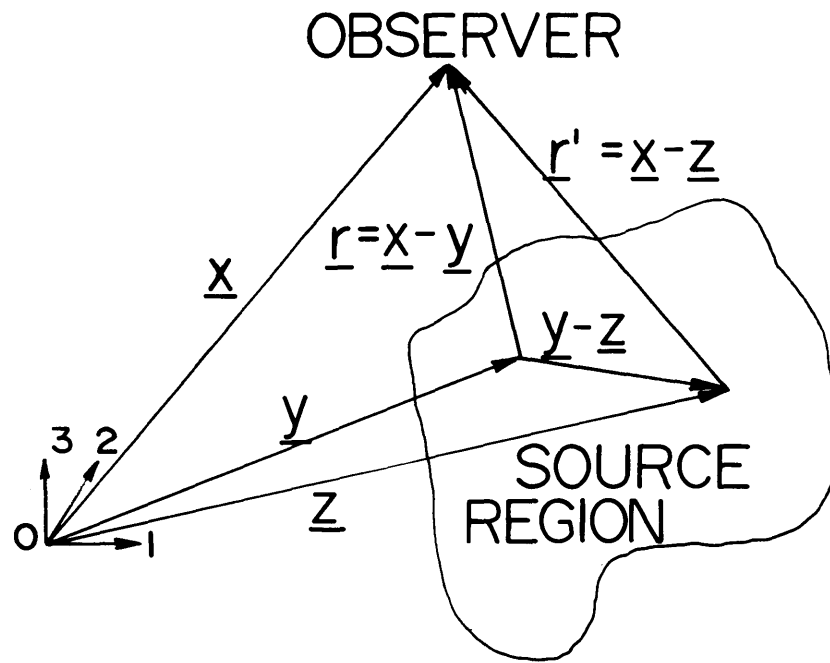


Fig. 3. Generalized source region in infinite space.

where $r = |\underline{x} - \underline{y}|$ and $\frac{\partial r}{\partial x_i} = -\frac{\partial r}{\partial y_i} = \cos \theta_i$.

Forming the autocorrelation of the signal at the observer

$$\langle P(\underline{x}, t) P(\underline{x}, t + \tau) \rangle = B(\underline{x}, \tau) ,$$

$$B(\underline{x}, \tau) = \hat{E}^2 \int_{-\infty}^{\infty} \int_{-\infty}^{\infty} \left\{ \frac{\cos \theta_i \cos \theta'_j}{r^2 r'^2} \right. \quad (2.13)$$

$$\left. \langle f_i(\underline{y}, t) f_j(\underline{z}, t + \tau) \rangle \right\} d\underline{y} d\underline{z}$$

where $\langle \rangle$ denotes a time or ensemble average, $r' = |\underline{x} - \underline{z}|$, $\cos \theta'_j = \frac{\partial r'}{\partial x_j}$, and $\langle f_i(\underline{y}, t) f_j(\underline{z}, t + \tau) \rangle$ is the space-time correlation. Fig. 4 represents the artery collapsed to a line along the "1" axis. The stenosis is assumed to be located at the origin, and H represents the depth of the artery below the surface of the skin.

Representing the artery as a line source and its image, Eq. (2.13), reduces from a six-fold to a two-fold integral over the original source,

$$B(\underline{x}, \tau) = 4\hat{E}^2 \int_0^{\infty} \int_0^{\infty} \left\{ \frac{\cos \theta_i \cos \theta'_j}{r^2 r'^2} \right. \quad (2.14)$$

$$\left. \langle f_i(y_1, t) f_j(z_1, t + \tau) \rangle \right\} dy_1 dz_1$$

The factor of 4 arises because the image source causes pressure doubling at the boundary. The function $f_i(y_1, t)$ now represents the force per unit length.

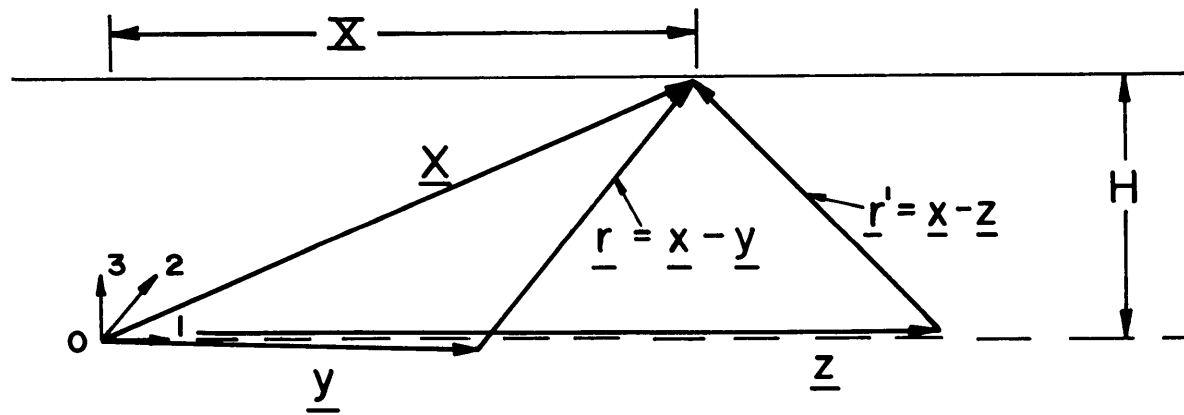


Fig.4. Artery modelled as a line source of excitation.

Because the jet is not axially homogeneous the remaining correlation $\langle f_i(y_1, t) f_j(z_1, t + \tau) \rangle$ is stationary but not homogeneous. It is very convenient to assume that the inhomogeneous tensor can be split into inhomogeneous and homogeneous parts in the following manner:

$$\langle f_i(y_1, t) f_j(z_1, t + \tau) \rangle = W(y_1, z_1) R_{ij}(\Delta, \tau) \quad (2.15)$$

where $\Delta = y_1 - z_1$, and the tensor R_{ij} is analogous to the space-time correlation in homogeneous turbulence. Mollo-Christensen (1967) has suggested general analytic forms for $W(y_1, z_1)$. In this analysis it will be assumed that $W(y_1, z_1) = \alpha^2 y_1, z_1 e^{-(y_1 + z_1)/L}$, where L is a characteristic decay length of the jet^{††} and α is a constant with dimensions of inverse length; i.e. the jet builds up to a maximum value at $y_1 = z_1 = L$, and then decays exponentially. The maximum value will scale with α . Eq. (2.15) requires an assumption of local axial homogeneity of the turbulence. That is, the characteristic correlation length scale ℓ (length scale of R_{ij}) is much smaller than the jet decay length scale L (length scale of W). Therefore, at any given point $W(y_1, z_1)$ is essentially constant over one correlation length scale, and the flow appears to have local axial homogeneity. Clearly the tensor R_{ij} must obey laws of symmetry, being axisymmetric about a unit vector $\underline{\lambda}$ along the line source, and invariant with respect to reflection into any point on the line source. The form of such a tensor is given in Bachelor (1967)

^{††} In Section IV.3 it will be shown that $L \propto \nu/u_j$. To normalize W we would usually set $W(L, L) = 1$, (which implies $\alpha = e/L$) so that the maximum value of $\langle f_i(y_1, t) f_j(z_1, t + \tau) \rangle$ is identical with the maximum value of $R_{ij}(\Delta, \tau)$ and the remainder is scaled downward.

$$R_{ij}(\underline{\Delta}, \tau) = A \Delta_i \Delta_j + B \lambda_i \lambda_j + C \delta_{ij} + D \Delta_i \lambda_j + E \Delta_j \lambda_i .$$

where A,B, etc. are arbitrary functions of Δ^2 and $\Delta_i \lambda_i$. In the model presented here, $\underline{\Delta} = (\Delta, 0, 0)$ and $\underline{\lambda} = (1, 0, 0)$. In addition we only consider stresses normal to the wall of the artery, so $i, j = 2, 3$ only. Then the above equation simplifies to

$$R_{ij}(\Delta, \tau) = R(\Delta, \tau) \delta_{ij} , \quad i, j = 2, 3 \quad \text{only} \quad (2.16)$$

$R(\Delta, \tau)$ is the homogeneous space-time correlation. Fig. 5 represents a typical space-time correlation obtained in turbulent flows. Corcos (1964) shows that the cross spectral density $\Gamma(\Delta, \omega)$, the temporal Fourier transform of $R(\Delta, \tau)$, can be approximately represented as a function of the similarity variable $\frac{\omega \Delta}{U_c}$ by

$$\Gamma(\Delta, \omega) = \phi(\omega) A\left(\frac{\omega \Delta}{U_c}\right) \cos \frac{\omega \Delta}{U_c} \quad (2.17)$$

where $\phi(\omega)$ is the force spectral density at the source, U_c is the convection velocity which can be taken as a .61 times the center line velocity of the flow (Clinch, 1969). The fractional value is not critical to the argument so long as it does not vary widely. The data reported by Clinch (1969) applies to fully developed turbulent pipe flow, and reflects the fact that large eddies close in size to the pipe diameter must convect with nearly the mean velocity, while small eddies close to the wall (and the laminar sublayer), convect considerably slower. When

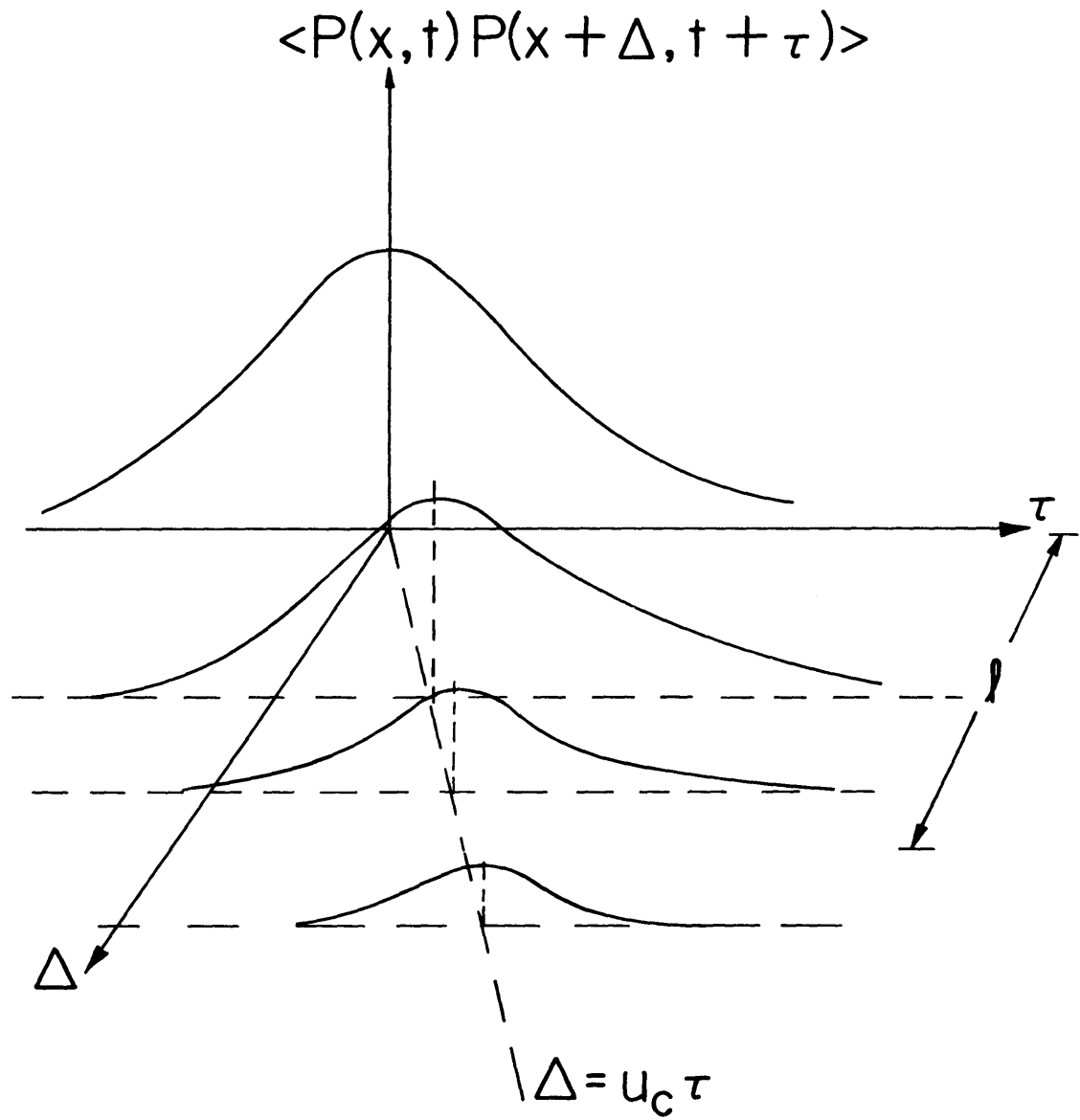


Fig.5. A typical space-time correlation.

the average over all eddies is taken, the convection velocity of the pressure field must be a fraction of the centerline velocity of order unity. The turbulent pressure field downstream of an orifice would be expected to behave in a similar manner.

A is a monotonically decreasing function which takes into account that the correlation decays. It can easily be shown that (2.17) follows from the assumption $R(\Delta, \tau) = AR(0, \tau - \Delta/U_c)$, i.e. that the eddies convect and decay, where $R(\Delta, \tau) : \Gamma(\Delta, \omega)$ and $\phi(\omega) \cos \frac{\omega \Delta}{U_c} : R(0, \tau - \frac{\Delta}{U_c})$ are Fourier transform pairs. Willmarth and Roos (1965) found that for turbulent boundary layers the similarity hypothesis of Corcos is not valid for $\frac{\omega \delta^*}{U_\infty} > 3$. No similar criterion is available for pipe flow, but by introducing an analogous displacement thickness for turbulent pipe flow,

and assuming $u/U_o = (\frac{R-r}{R})^{1/7}$, the above condition becomes $\frac{fD}{U} \geq 10$.

This excludes only a small part of the turbulent spectrum. Of course this is a crude estimate at best, and the true limits of validity of the similarity assumption will have to be demonstrated experimentally.

It is reasonable to fit data for A by an exponential (Willmarth and Roos 1965) of the form

$$\exp \left[- \frac{|\Delta|}{\ell(\omega)} \right] \quad \text{where} \quad \ell(\omega) \propto \frac{U}{\omega} \quad (2.18)$$

which implies that turbulence is a phenomenon that tends to erase the fluid's "memory" as distance (or time) passes, and that large eddies stay correlated longer than small eddies. Assuming that the homogeneous cross spectral density (17) is valid, we apply these considerations to (2.14), perform the temporal Fourier transform and obtain

$$\pi(\underline{x}, \omega) = 4\hat{E}^2 \phi(\omega) \int_0^\infty \int_0^\infty \left\{ \frac{\cos \theta_i \cos \theta'_j}{r^2 r'^2} \right. \\ \left. \delta_{ij} W(y_1, z_1) e^{-|\Delta|/\ell} \cos \left(\frac{\omega \Delta}{U_c} \right) \right\} dy_1 dz_1 \quad (2.19)$$

$$i, j = 2, 3$$

where $\pi(\underline{x}, \omega)$ is the power spectrum of the pressure observed at the point \underline{x} . Defining a correction factor $C(\underline{x}, \omega)$

$$C(\underline{x}, \omega) = \frac{\pi(\underline{x}, \omega) L^2}{4\hat{E}^2 \phi(\omega)} \quad (2.20)$$

and changing coordinates

$$C(\underline{x}, \omega) = L^2 \int_0^\infty dy_1 \int_{-\infty}^\infty d\Delta \left\{ \frac{\cos \theta_i \cos \theta'_j}{r^2 r'^2} \right. \\ \left. \delta_{ij} W(y_1, y_1 - \Delta) e^{-|\Delta|/\ell} \cos \left(\frac{\omega \Delta}{U_c} \right) \right\} \quad (2.21)$$

$$i, j = 2, 3$$

The inner integral now represents the contribution to the signal at the observer due to one correlation length centered at y_1 . Clearly the only part of this integral that contributes is the region over which the signal is well correlated (i.e. when $e^{-|\Delta|/\ell}$ is of order 1). The outer integral represents the summation of all these contributions along the line source. If we limit our attention to the frequency range given by $\frac{\ell(\omega)}{H}$, $\frac{\ell(\omega)}{L} \ll 1$, then Eq. (2.21) may be asymptotically evaluated in this limit as

$$C(\underline{x}, \omega) = \frac{2(\ell/H)LH}{1 + \left(\frac{\omega\ell}{U_c}\right)^2} \int_0^\infty \frac{L \cos \theta_i \cos \theta_j \delta_{ij}}{r^4} W(y_1, y_1) dy_1 \quad (2.22)$$

$$i, j = 2, 3$$

This is because under these assumptions $r \approx r'$, and $\theta_i \approx \theta'_i$ (the geometrical spreading terms and W in (2.20) are nearly constant over one correlation length scale). The integral in (2.22) is denoted by I and is shown in Fig. 6 for $\frac{X}{L} = 1$ ($\frac{X}{L} = 1$ implies that the observer is above the point of maximum turbulent intensity).

Discussion

The approximation with which one goes from (2.21) to (2.22) limits the region of validity of the result to high frequencies, but the simplicity gained makes the physics of the result (2.22) quite clear. In a stiffness controlled system (i.e. as given by Eq. 2.10), an excitation of length scale ℓ will produce a region of significant stress and strain also of length scale of order ℓ . In the turbulent flow $\ell = \ell(\omega) \propto \frac{U_c}{\omega}$, thus $C(\underline{x}, \omega) \propto \frac{1}{\omega}$ (2.22) which implies that low frequencies (large ℓ) are detected at the observer much more readily than high frequency (small ℓ) excitations, as one should expect. Thus the spatial decay in the elastic system evidences itself as a low pass filter in the frequency domain. This is a first order effect that must be taken into account in analyzing spectra of bruits radiating from constricted arteries.

Looking at the interesting limits of these results, as $\ell \rightarrow 0$ we find that $C \rightarrow 0$, which should be expected. As $H/L \rightarrow \infty$ the artery looks like a point force, thus the power falls off like H^{-4} (see Eq. 2.12).

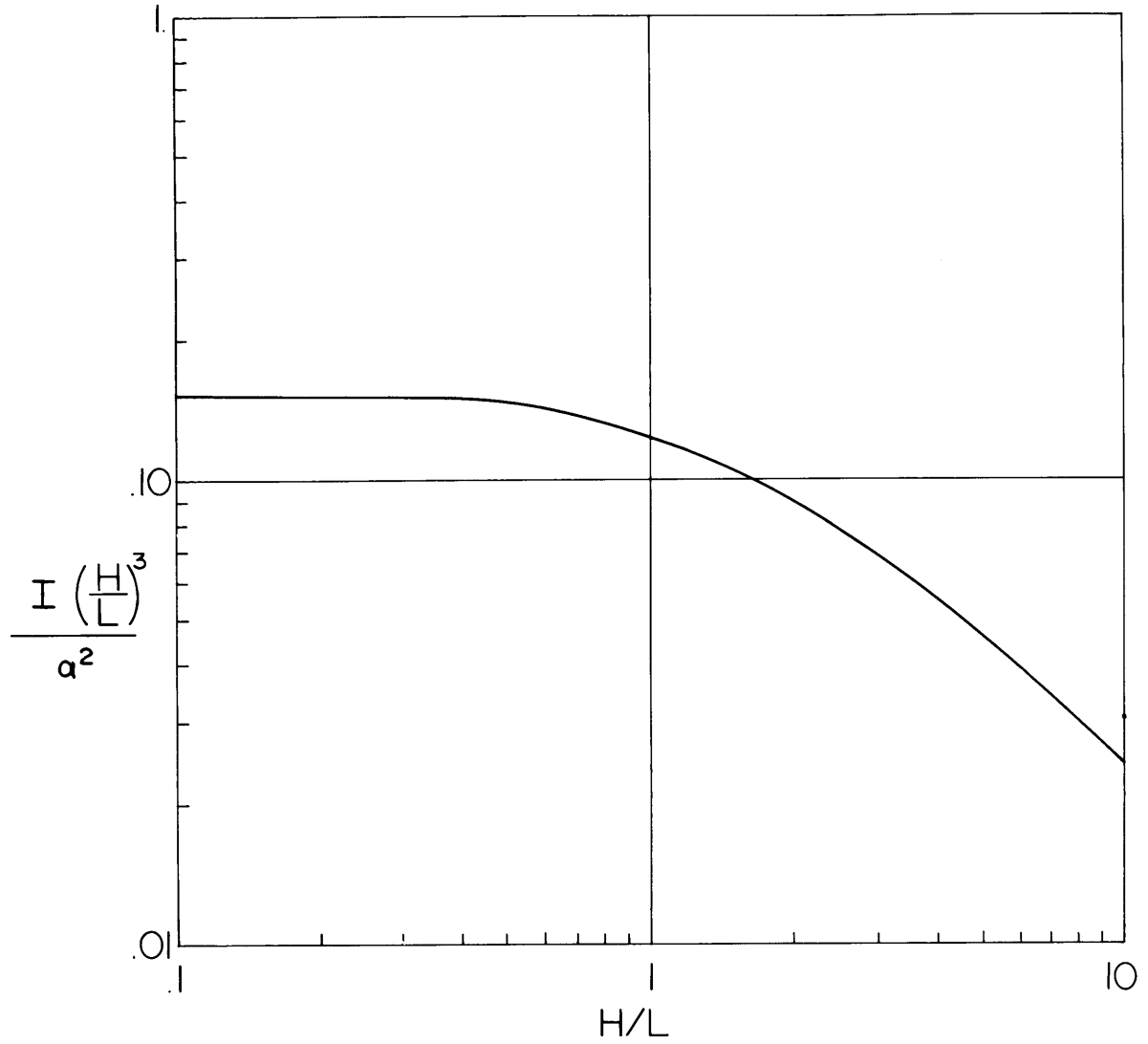


Fig.6. Intensity integral I for $X/L = 1$.

As $\ell(\omega)/H \rightarrow 1$, the asymptotic approximation (2.22) is not valid, i.e., when one is very close to the source (closer than the smallest excitation length scale) there should be no frequency correction because there is no appreciable distinction in spatial decay of the different excitation length scales. Clearly, as H/D becomes $O(1)$ the line source also becomes a questionable model. The exact solution for a cylindrical source has been obtained and is given in Appendix A. It demonstrates the same basic result with the addition of a lateral correlation length scale, η ,

$$\pi(\underline{x}, \omega) = \frac{(\ell/H)(\eta/H)\hat{E}^2 I' E(\omega)}{1 + \left(\frac{\omega \ell}{U}\right)^2} \quad (2.23)$$

In this result η as well as ℓ tend to be proportional to ω^{-1} (Willmarth and Roos, 1965), so the overall correction factor should be approximately proportional to ω^{-2} . I' represents another geometrical integral, and $E(\omega)$ represents the wall pressure spectrum at the wall of a cylinder (as distinct from $\phi(\omega)$, the force spectrum). The apparent contradiction of (2.22) and (2.23) is resolved by the detailed computation of the collapse from a cylinder to a line source which reveals that $E(\omega)$ and $\phi(\omega)$ are related by a factor of η , so that Eqs. (2.22) and (2.23) are in agreement for $H/D \gg 1$, and the overall correction between the wall pressure spectrum and the spectrum at \underline{x} is approximately proportional to ω^{-2} .

The low frequency limit below which this model is invalid is given by $\frac{\ell(\omega)}{H} = O(1)$. But since $\ell(\omega) \propto \frac{U}{f}$, the model should be valid for

$$\tilde{f}\left(\frac{H}{d}\right) \gg 1 . \quad (2.24)$$

where $\tilde{f} = \frac{fd}{U}$ is the nondimensional frequency relevant to flows at this type. (See Chapter III.)

While this final assumption (2.25) is at variance with part of the spectrum of interest in some in vivo cases, it represents an essential mathematical simplification and should not destroy the qualitative features of the model.

It has already been mentioned that when $H/\ell(\omega) \ll 1$ the correction factor must be unity, which implies a form of the correction factor which approaches 1 as $\tilde{f}\left(\frac{H}{d}\right)$ goes to zero and approaches $1/f^2$ as $\tilde{f}\left(\frac{H}{d}\right) \gg 1$. It is not clear what the exact analytic form of this function should be in the region where $\tilde{f}\left(\frac{H}{d}\right) = O(1)$. The exact solution could be obtained by evaluation of a fourfold frequency dependent integral of Eq. (A.8) over the surface of a cylinder. However, it is felt that an empirical or experimental approach is more appropriate.

For clinical application the two asymptotic results can be combined to provide an empirical correction function. A correction of the form

$$C(\omega) \propto \frac{1}{1 + \frac{\ell(\omega)}{H} \frac{\eta(\omega)}{H}} = \frac{1}{1 + \beta^2 \tilde{f}^2 \left(\frac{H}{d}\right)^2} \quad (2.25)$$

has been found to correct Gurll's predictions of arterial velocity to within the scatter of his data, and therefore probably represents a reasonable approximation to the exact correction function. β^2 is a constant of order unity. This correction function will be discussed further in Section 5.1.

Chapter III. The Experiment

III. The Experiment

The previous sections provide an estimate of the relationship between the spectral density of pressure at the skin surface when held motionless and the spectral density of pressure at the arterial wall. In order to complete the phonoangiographic objectives of determination of parameters of the flow from sounds at the skin surface, one must relate the spectral density at the wall of the artery to the flow parameters and geometries. This is accomplished by experimental procedures described in this section.

3.1 Experimental Objective

The task of correlating the quantitative nature (spectral density and rms value) of the disturbances at the tissue surface with the parameters of interest (d/D and U) is greatly simplified by the knowledge of the relation of pressure fluctuations at the wall of the artery to the fluid dynamic parameters of the flow. For this reason an in vitro experiment was undertaken, the objective of which was to measure the turbulent wall pressure fluctuations downstream of an orifice under known conditions. From these data, scaling laws can be developed which can adequately permit prediction of the root mean square and spectral pressure distribution downstream of a stenosis in a human artery. In addition, one obtains a clearer understanding of relevant physics of the problem.

To this end one must preserve dynamic and geometric similarity in the experimental flows. These similarity considerations are discussed in the following section.

3.2. Similarity Considerations

In designing any experiment, one must identify the relevant non-dimensional parameters of the flow. Once all of these parameters have been identified the experiment can be designed such that the experimental range of these parameters coincides as closely as possible with the range of interest. In this way one can scale up the experimental results to fit the real world (in vivo) problem.

Assuming that the arterial compliance does not significantly alter the internal turbulent flow, the spectral distribution of the turbulent pressure fluctuations at some point on the wall a distance z downstream of the orifice can be expressed as:

$$E(\omega) = F[f, f_H, D, d, U, \rho, \mu, z, \text{stenosis shape}] \quad (3.2.1)$$

where f_H is the heart rate and U is the peak systolic velocity (see Fig. 7). By means of the continuity equation the jet velocity u , could have been specified instead of U , since $\frac{U\pi D^2}{4} = \frac{u\pi d^2}{4}$. The shape of the stenosis is not quantified at this time because there are many families of shapes that one might study. This will be discussed in later sections.

If the power spectral density of the pressure is expressed non-dimensionally, it cannot be a function of any parameters with dimensions. Thus

$$\frac{E(\omega)}{\rho^2 U^3 D} = F\left[\frac{f}{f_H}, \frac{fD}{U}, \frac{d}{D}, \frac{UD}{v}, \frac{z}{D}, \text{stenosis shape}\right] \quad (3.2.2)$$

This is a sufficient set of parameters to uniquely specify the flow, and all other parameters can be formed from them. For example, from the

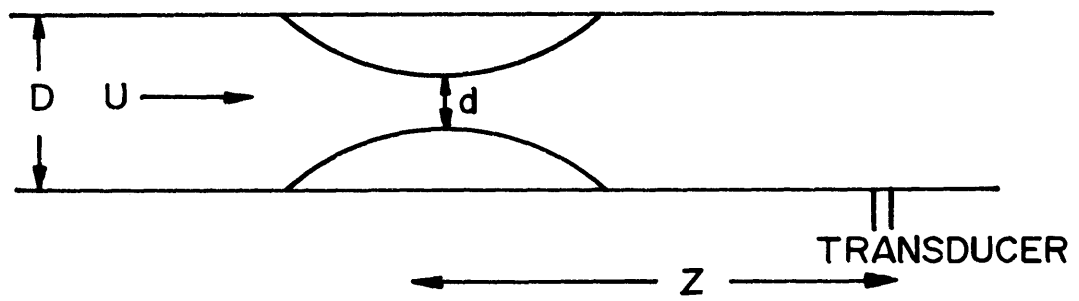


Fig.7. Idealized geometry of a stenosed artery.

parameters of Eq. (3.2.2) one can form the so-called Wormsley parameter for pulsatile flow

$$\frac{D^2 \omega_H}{4\nu} \propto \frac{fD}{U} \cdot \frac{f_H}{f} \cdot \frac{UD}{\nu} \quad (3.2.3)$$

The parameters as represented in Eq. (3.2.2.) may not be in the form which is most meaningful physically. The experiment itself will hopefully lead to new parameters which will reveal the physical mechanisms at work in a clearer manner. Of course, these new parameters are just combinations of the old ones of Eq. (3.2.2).

If attention is restricted to that part of the cardiac cycle when the velocities are high and the rate of change of velocity is small (peak systole), then turbulent frequencies will be high (since the frequency scales with the velocity in turbulent flow) compared with the heart rate f_H , and $f/f_H \gg 1$. This implies that the heart rate is not an important feature of the turbulent flow, at least for the period of large arterial velocity. Equivalently, during systole eddies are created, cascaded down the energy ladder, and dissipated, before the mean velocity has changed appreciably. Hence the physical laws which govern the eddy motion should be independent of cardiac frequency. By assuming that the flow is quasi-steady, and using maximum systolic velocity as the relevant velocity scale in the unobstructed portion of the artery, one can adequately model the physics occurring at systole by a steady flow experiment. Therefore the dependence in Eq. (3.2.2) on the parameter f/f_H will be ignored, and all experiments referred to in this work will be steady flow experiments.

However, it should be noted that the stability of the jet and the transition from laminar to turbulent flow at the beginning of systole,

when velocities are rapidly changing with time, will in fact be dependent not only on the fundamental frequency f_H , but also on its harmonics, which must be summed in a Fourier series to represent the velocity-time profile. It has been noticed that the amplitude-time traces of a bruit observed in vivo tend to have regular deterministic upbeats and oscillations for the first ten percent of systole. In addition, the very low-frequency components of the flow can be sensitive to changes in velocity during systole, but these components do not contain a significant amount of energy. By restricting attention to the period of peak systole this problem is minimized.

Up to this point little has been said about stenosis shape (other than the diameter ratio d/D). Assuming an axially symmetric stenosis, the most important characteristic of the shape of any stenosis is the radius of curvature, a , at the minimum cross-section, normalized by the diameter at that point, d (see Fig. 8). Using an inviscid model and assuming that the curvature of the streamlines varies linearly from zero at the center line of the flow to a value of a^{-1} at the stenosis boundary, one can show that the velocity at this cross-section is a decreasing function of the distance y from the stenosis surface. This is required in order for the centrifugal acceleration of the fluid to be balanced by the radial pressure gradient. The resulting expression is

$$v(y) \propto \exp\left[-\frac{1}{ad} (dy - y^2)\right] \quad (3.2.4)$$

which leads to

$$\frac{v(y = 0)}{v(y = d/2)} = e^{d/4a} \quad (3.2.5)$$

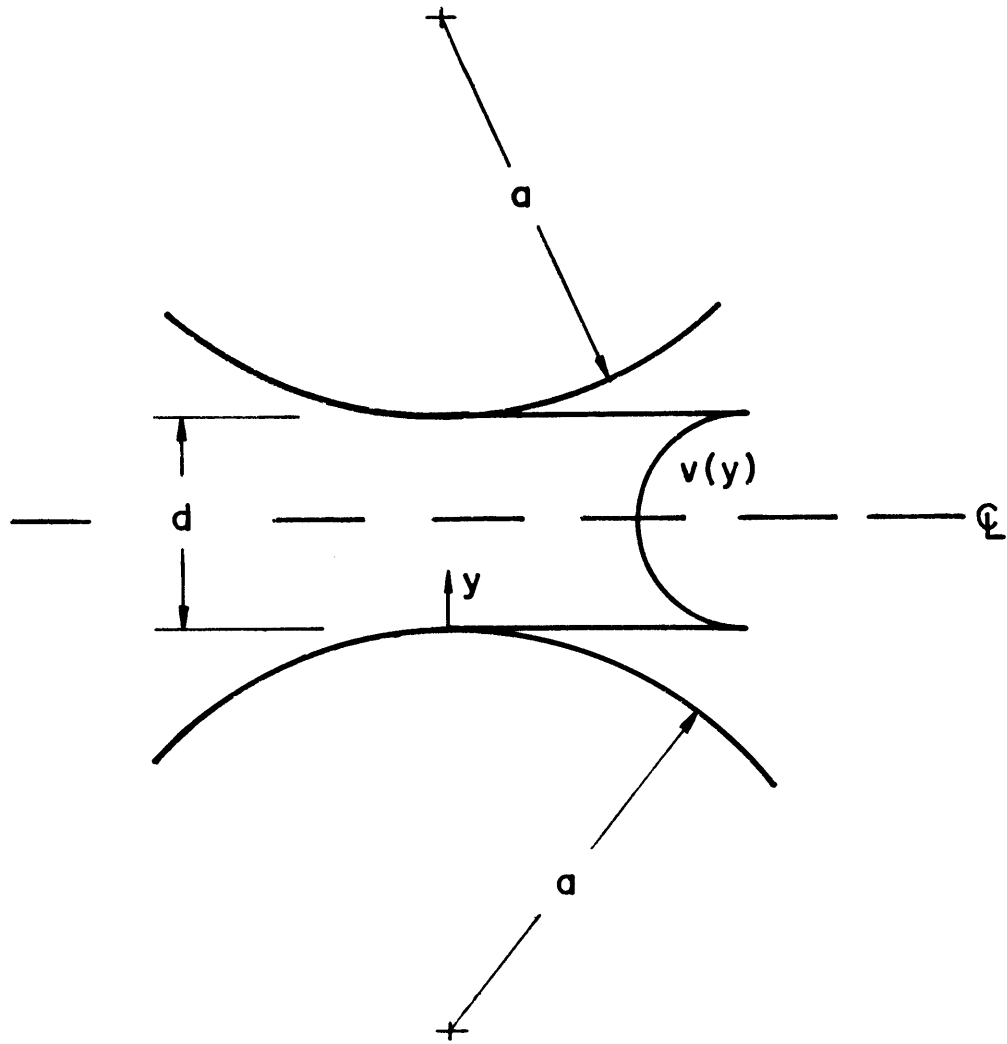


Fig.8. Velocity profile for inviscid flow through a converging channel.

Therefore the velocity near the lip is larger than the centerline velocity by an exponential factor of $d/4a$. Because the jet separates from the stenosis wall, a shear layer is created at the interface of the separated jet and the region of recirculatory flow. It is this shear layer that becomes unstable and causes the jet to become turbulent. The stability of this shear layer will be dependent upon the velocity gradient across the layer, which in turn depends on the velocity excess at the stenosis lip as compared to the centerline. Therefore, the radius of curvature of the stenosis lip can be a critical design parameter, whose neglect could lead to exponential error as regards stability and incipient turbulence.

There are two conditions under which the radius of curvature can be neglected as a variable of the problem: a) when $a = 0$, or b) $d/4a \ll 1$. The condition that $a = 0$ implies the use of a sharp edged orifice. By ensuring extreme sharpness at the lip, no ambiguity will exist in normalizing data from different orifice plates. The condition that $d/4a \ll 1$ implies that the radius of curvature is large enough so that the velocity excess at the stenosis lip is small and is a very weak function of $d/4a$. However, if $d/4a$ is of order 1 or greater, and is not held fixed, one can expect some difficulty in normalizing data and relating it to in vivo observations.

However, this line of reasoning is a bit idealistic, and some ambiguity still remains regarding this point. Stenoses found at autopsy tend to be close to the condition $d/4a \ll 1$ if one neglects small scale roughness. However, this roughness can have very small local radii of curvature, which could lead to high velocity gradients locally. In this work the stenoses were designed such that $d/4a \ll 1$, which lead to velocity ratios (Eq. 3.2.5)

in the range 1.1 to 1.2. Thus, radius of curvature should not be an important parameter in these experimental results. However, in comparing these results to in vivo observation one should bear in mind that the surface roughness at the stenosis throat could lead to transition to turbulence at a lower value of Reynolds number than that found in this work. At Reynolds numbers significantly above the critical Reynolds number the surface roughness should not significantly alter the spectral nature of the turbulent pressure fluctuations at the wall.

The velocity profile at the entrance to the stenosis must also be considered. In vivo flow through major arteries is a developing flow (neither a fully developed parabolic profile, nor a plug flow). This arises because the flow is unsteady. During each systolic period vorticity diffuses into the flow from the walls. If the time available for this diffusion process were much less than D^2/ν the flow would appear to be uniform. If the characteristic time is much greater D^2/ν the flow becomes parabolic. This effect is usually discussed in terms of the Wormsley parameter

$$\alpha = \frac{D^2 \omega}{4\nu}$$

In the coronary arteries α becomes as low as 3, while in the major arteries, such as abdominal aorta or femorals, α is as large as 15. Therefore the physiological flows of interest are, in general, developing flows. The experimental entrance length in the steady flow experiments was designed to have a similar type of developing flow.

It is felt that nonuniformity of the entrance flow is not a critical factor in the flow because the convective acceleration in the converging

section of the orifice tends to flatten nonuniformities in the entrance flow profile. Vorticity in the entrance flow is reduced by a factor of d/D at the jet because the circumferential vortex lines are shortened by the same factor d/D (following Helmholtz's vortex laws). Thus, while some variation in the velocity profile at the jet may exist as a result of the upstream nonuniformity, it is felt that these variations are unimportant.

The effects of eccentricity of the stenosis were not studied in this work. However, it is felt that this is not a major factor because the turbulent jet will tend to spread and fill the entire arterial cross-section before it has convected many diameters downstream.*

Another interesting design consideration occurs because of similarity requirements. The free stream Reynolds number at systole is about 1000 or less in the arteries of interest. This is a low Reynolds number in terms of familiar turbulent phenomena. The question arises, how does one maintain a low Reynolds number in the model while maximizing to turbulent pressure fluctuations at the wall in order to increase the signal to noise ratio? The pressure fluctuations scale roughly as ρU^2 , and $U = \nu \text{Re} D^{-1}$. This implies that one should increase the kinematic viscosity ν while decreasing the diameter D , with a resulting increase in the rms pressure and flow rate. The limiting considerations for increasing the viscosity are

- 1) non-Newtonian behavior
- 2) pump flow rate
- 3) pressure drop ($\Delta p \sim \rho U^2$ because most of the pressure drop occurs at the stenosis).

* Anomalous phenomena such as the Coanda effect are exceptions to this statement. Robbins and Bentov (1967) showed that the wall can produce a stabilizing effect on wall jets.

- 4) dissipation heating $\sim \Delta P Q \approx \rho U^2 Q \sim U^3$
- 5) cavitation
- 6) transducer size

The dissipative heating becomes important because of the temperature-viscosity relation of most fluids. (This will be discussed in III F).

The limiting small value of the tube diameter is set by the size of the pressure transducer. This will be discussed in Section III D.

Cavitation also becomes a serious limitation. Because the pressure at the orifice throat becomes very small for small values of d/D , cavitation, or equally bad, expansion of very small bubbles in the working fluid, radiates sound which can render results meaningless. This was in fact encountered in the experiment with high flow rates and large area reductions.

Weighing these tradeoffs the experiment was designed as follows:

Fluids: Dow Corning 210 H silicone oil 100 cs

Dow Corning 200 silicone oil 20 cs

Tube diameter: ID = 3/4 inch (1.91 cm)

Once the diameter and viscosity are fixed the design process follows simply from the similarity laws.

It should be noted that increasing v and U and decreasing D has the beneficial effect of increasing the frequency range of the experiment because $f \sim U/D$ for turbulent phenomena. This higher frequency range allows data collection in the audio band without the use of frequency modulated equipment, and also simplifies data analysis because it decreases the required averaging times.

3.3. The Fluid Loop

Fig. 9 depicts the fluid system loop used to provide flow through the test section. A reservoir acts as a capacitor and supplies the pump. The exit from the pump flows into a tank enclosing a given mass of air. The function of this tank is to provide an "air spring", or compliance to filter out fluctuations in the pressure and flow generated at the pump, thus acting as a low pass filter. The fluid flows from the capacitor into the settling chamber-flow straightener by way of a flexible tube. This flexible tube serves a two-fold function since it does not transmit axial compressional waves in the wall, and helps to decouple the test section from the rest of the system, the object being to isolate the test section from unwanted structural vibrations generated at the motor or pump. The settling chamber-flow straightener and test section are rigidly mounted to a vertical steel I beam. The return from the test section to the reservoir is again via flexible tubing. The I beam is mounted on vibration isolators which are in turn mounted on the floor. Lead weights were bolted to the I beam to increase its inertia and decrease its resonant frequency.

The system is depicted in lumped parameters in an analogous circuit diagram in Fig. 10. The system as shown has three independent energy storage elements, two capacitors, and the fluid inertance (thus three state variables exist). The dominant resistance in the system is the stenosis, so the resistance is nonlinear due to the nonlinear pressure-flow relations in turbulent flow. The actual experimental system was found to be over-damped for all flow rates and stenoses. Upon starting the pump and thus charging capacitor c_2 , and also upon stopping the pump and running off

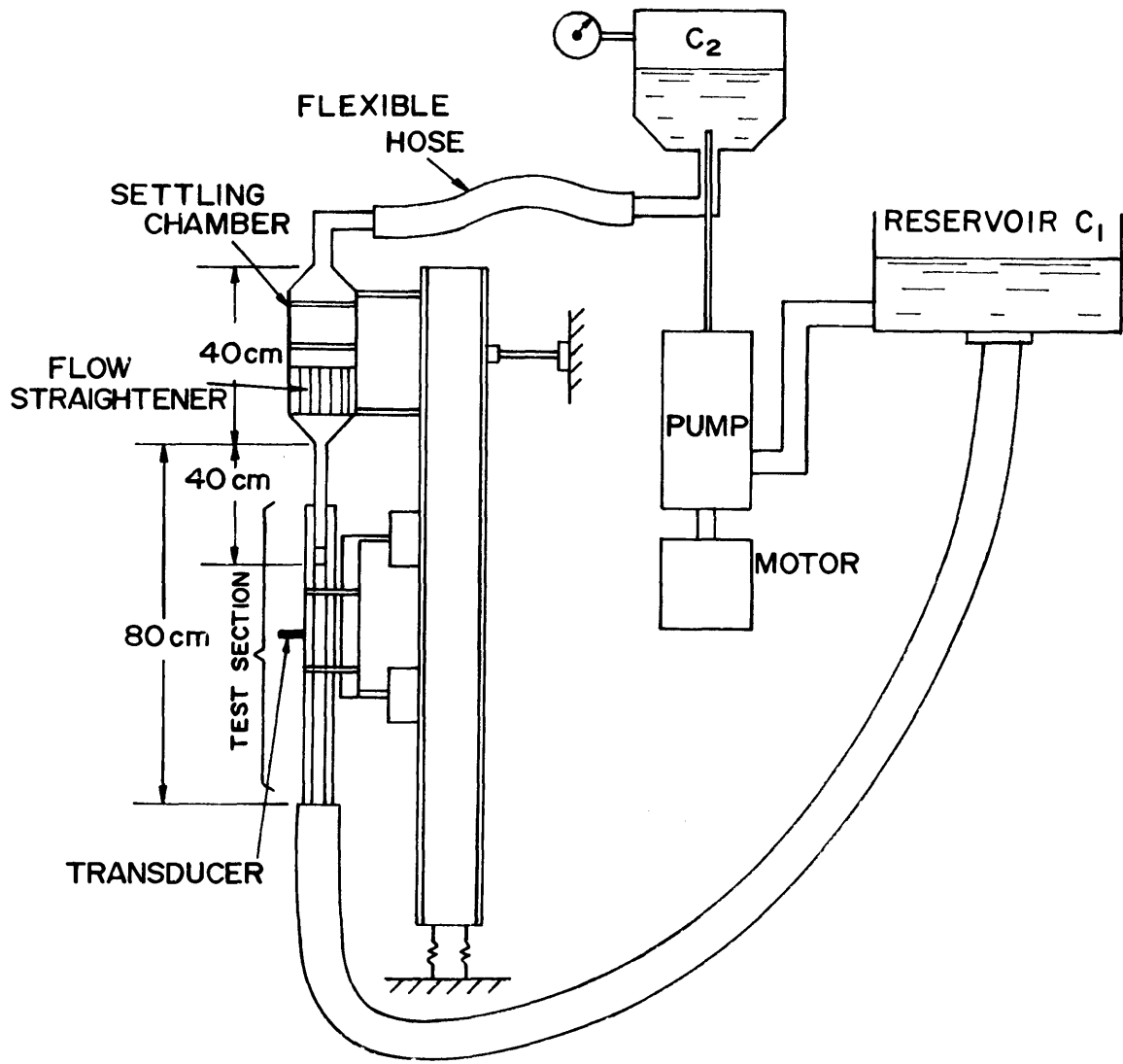


Fig.9. The experimental fluid loop.

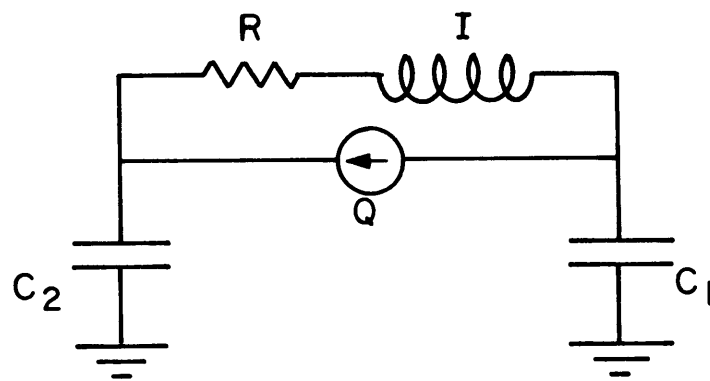


Fig.10. Electrical analog of fluid loop.

energy stored in capacitor c_2 , no oscillations of pressure or flow were observed. All pressure and fluid levels exhibited exponentially decaying response to step function inputs.

The settling chamber-flow straightener and test section are shown in Fig. 9. The settling chamber-flow straightener consists of an unobstructed settling portion followed by a honeycomb aluminum grid. Following the grid there is a severe reduction in area which reduces the fractional jet kinetic energy in any disturbance relative to the kinetic energy in the mean flow. The narrow portion of the flow straightener leads to a thin-walled brass tube 5/8" (1.59 cm) I.D. (See Fig. 11). 30 cms downstream from the flow straightener the brass stenoses are attached by soldering. Each stenoses is fitted with a groove to permit an "O"-ring seal with the 3/4" (1.91 cm) I.D. plexiglass tube which surrounds it. Because the "O"-ring seal is a sliding seal, the pressure transducer mounted in the plexiglass tube can be moved to different distances downstream of the stenosis. The mounting of the pressure transducer into the plexiglass tube is discussed in Section D.

The stenosis shape is shown in Fig. 12, with dimensions shown. The additional dimensions are shown below:

% area reduction	d/D	d(cm)	L(cm)
55	.67	.765	1.14
64	.602	.554	1.46
72	.521	.358	1.57
82	.423	.193	1.84
91	.305	.071	2.73

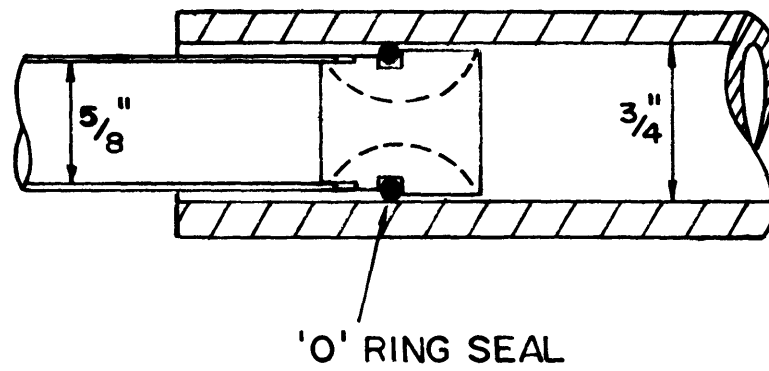


Fig. II. Mounting of the stenosis in the test section.

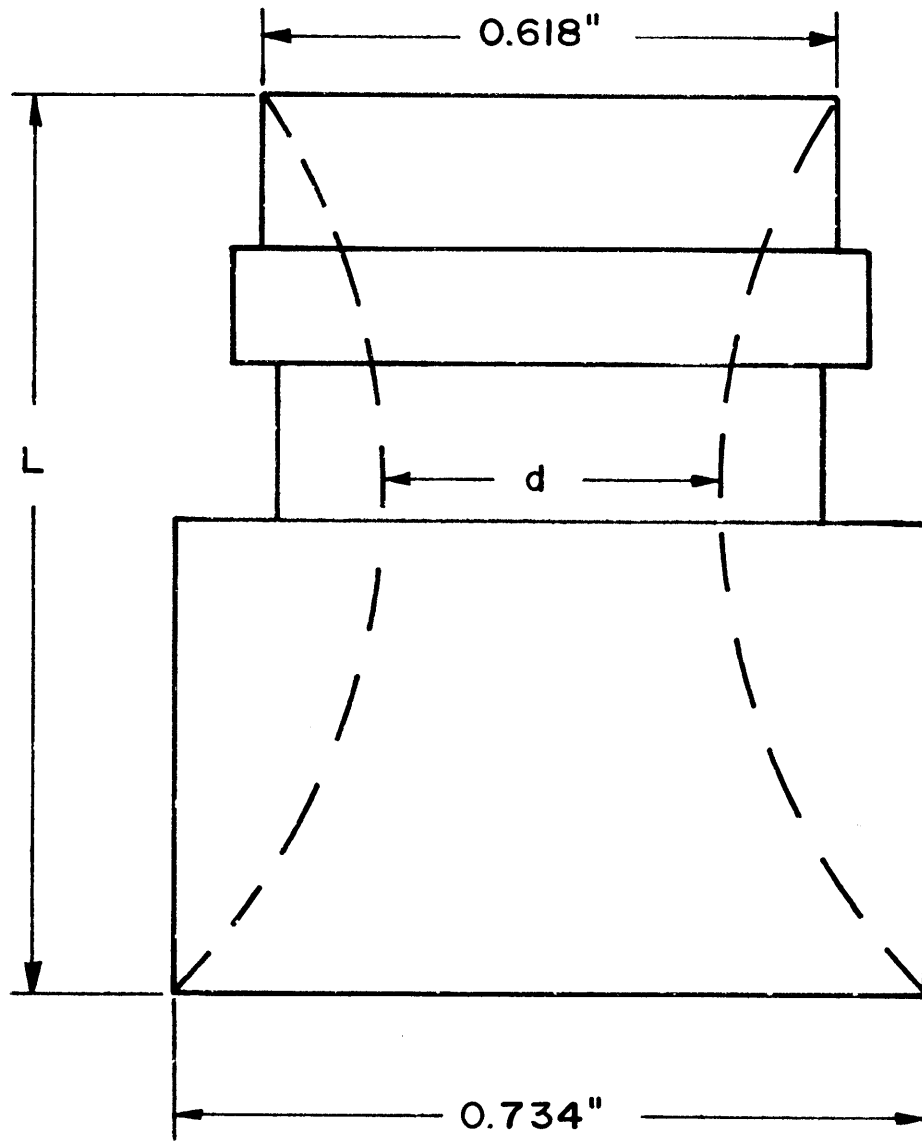


Fig.12. Stenosis dimensions.

As mentioned before, these stenoses were designed to have $d/4a$ approximately constant and substantially less than unity.

The flow rates were calculated by means of a pump calibration. The pressure-flow characteristic of the pump was measured for different values of the tachometer voltage (Fig. 13) with a stopwatch and bucket. Then, knowing the pressure in the capacitor tank and the tach voltage, one can simply calculate the flow rate.

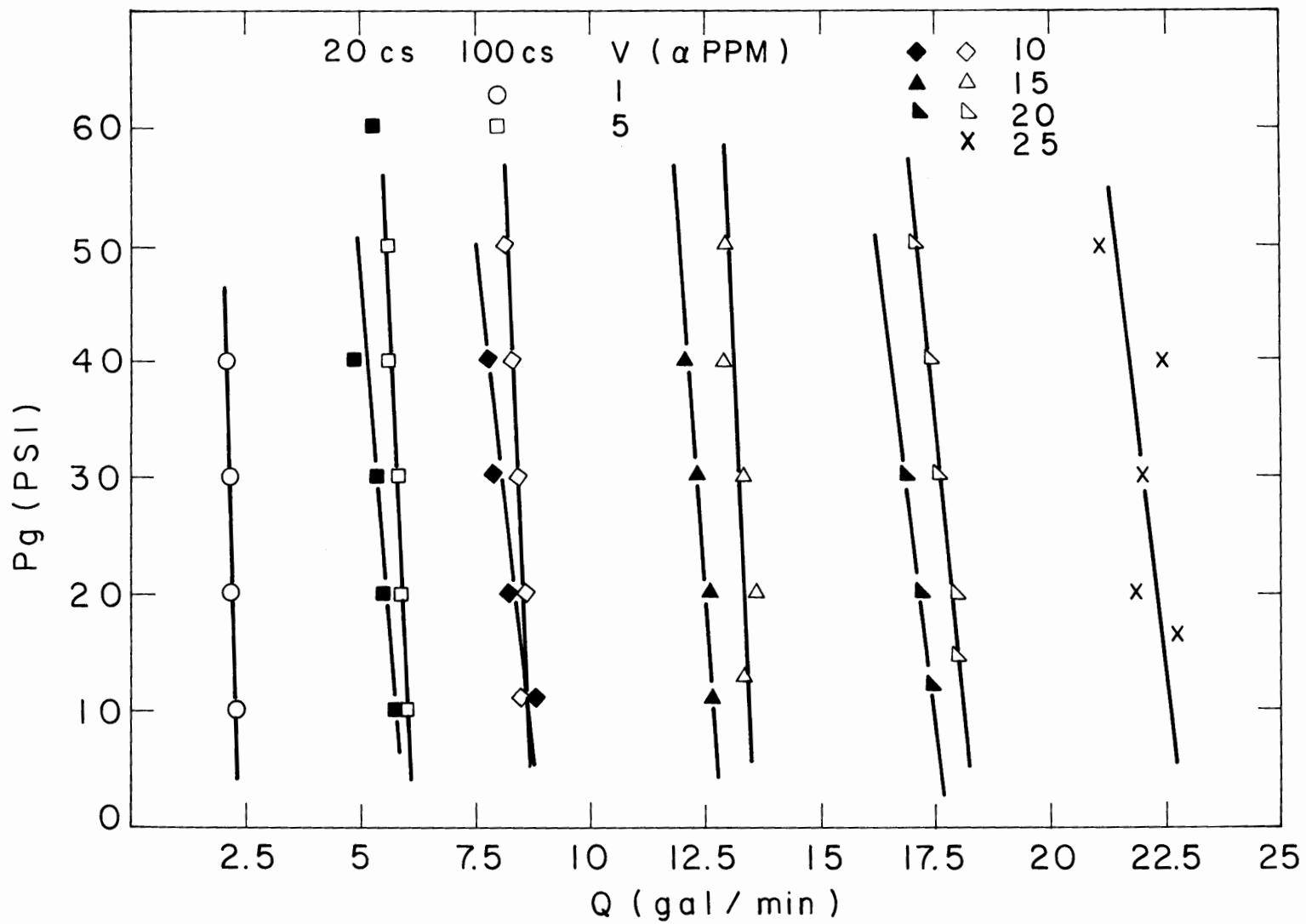


Fig.13. Pump calibration.

3.4. The Pressure Transducer

1. Description

The pressure transducer used in this experiment was a modified Bolt Beranek and Newman, Inc., miniature pressure sensor, model 377 (see Fig. 14 for dimensions). The transducer incorporates a Helmholtz resonator such that the diameter of the active sensing area exposed to the flow is small.

The specifications of the crystal (lead zirconate) and associated electronics are as follows:

Sensitivity	-114.5 dB re 1 volt/ μ bar ($1.88 \frac{\mu\text{V}}{\mu}$)
Pressure range	<100 PSI
Rise time	<3 μ SEC
Resonant crystal frequency	>100 KHz
Output impedance	1500 ohms
Vibration sensitivity	<.002 PSI/g
Noise level	<10 μ V rms in 10 KHz band

The transducer housing contains both the piezo-electro crystal and the first stage of signal processing (a unity gain field effect transistor circuit).

2. Size Considerations

The measurement of pressure in a turbulent flow is sensitive to the size of the transducer used. In order to resolve a spatial scale that is convecting past the active transducer surface, the transducer must be smaller than that length scale. When the transducer is of the same order or larger than the length scale to be resolved, the transducer output represents a spatial average of the pressure field, and does not accurately

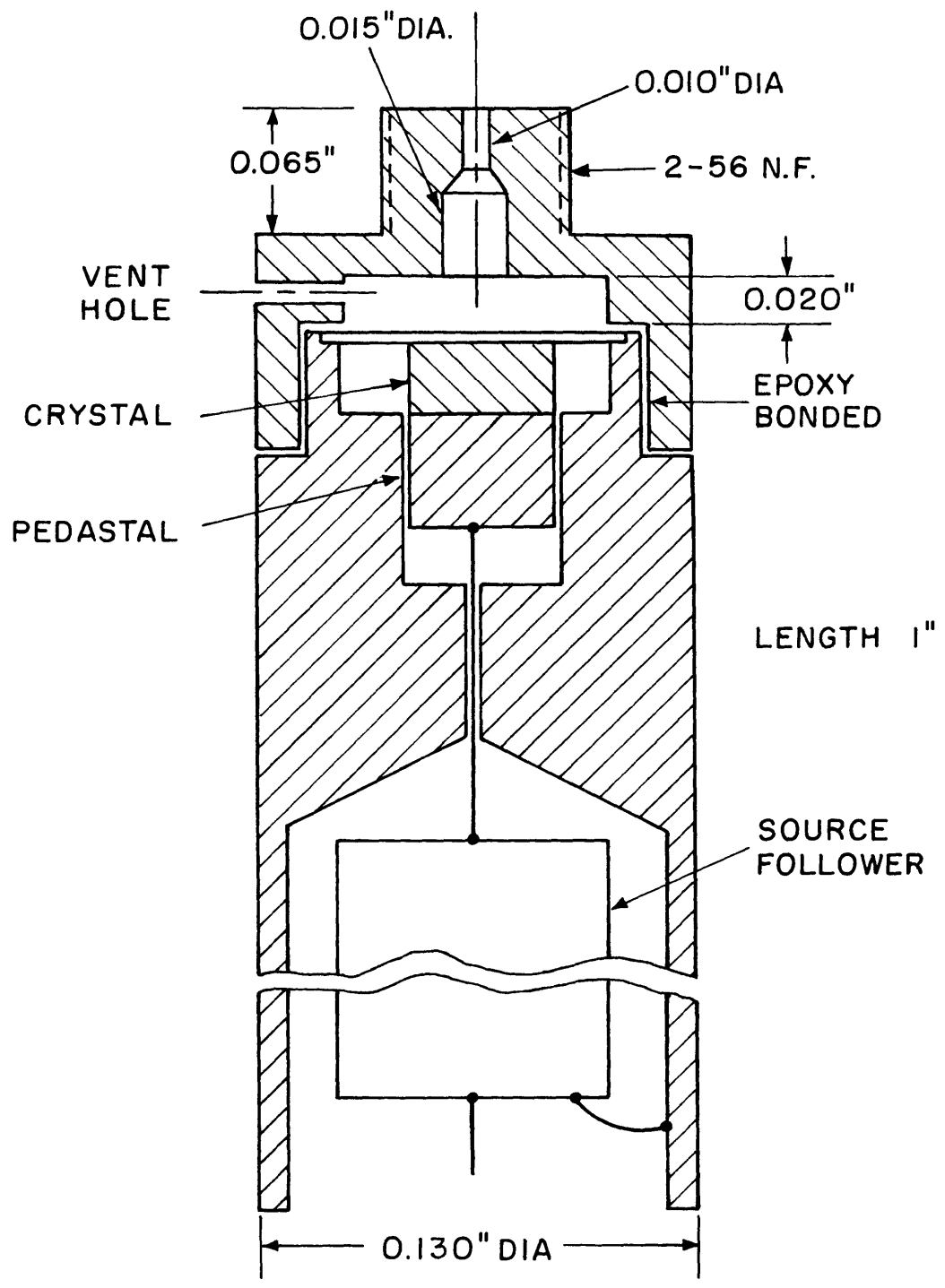


Fig.14. Diagram of pressure sensor.

represent the pressure at a point. The effect of finite size of flush wall mounted transducers in turbulent boundary layer flows has been studied extensively by Corcos (1963) and Willmarth and Roos (1965). As a result of these studies, correction factors for finite transducer size have been developed. However, these corrections are dependent upon the structure of the turbulent boundary layer field and some ambiguity exists in applying these corrections to other types of flows.

The simplest way to avoid this ambiguity is to ensure that the active sensing area of transducer is smaller than the smallest turbulent length scale of interest, thus eliminating the need for finite transducer size corrections. Willmarth and Roos (1965) showed that measurements of the present type will not be subject to large error if the highest frequency of interest is less than U/d_t , where U is a characteristic convection speed, and d_t is the diameter of the active sensing area of the transducer (.010 in). In the present experiment $U/d_t \sim 20$ KHz, whereas the highest frequency component of the wall pressure fluctuation which is of interest is 3Khz. Therefore no finite transducer correction was used. Some error always exists, the magnitude depending on $\omega d_t/U_c$. When $\omega d_t/U_c < 1$, Corcos' (1963) correction formula can be used. If $\omega d_t/U_c \ll 1$, the error becomes small enough that it need not be considered (Willmarth & Roos, 1965). Equivalently, in this experiment the finite transducer size should not become important until

$$\underline{f} = \frac{fd}{U} = \frac{d}{d_t} \approx 40 \quad (3.4.1)$$

Another possible source of error arises if the pressure is measured at a recessed port, as is done with this transducer. Franklin and Wallace (1970) found that errors arise in measurement of the static pressure at

the wall of a turbulent flow if one uses recessed ports. Reynolds stresses at the mouth of the port change the static pressure from what one would observe at a solid boundary by an amount of the order of the shear stress when the hole diameter is of the order of 250 viscous length scales ($v\sqrt{\rho/\tau}$). In the present experiment

$$d_t^+ = \frac{d_t}{v\sqrt{\rho/\tau}} \approx 0(1) \quad (3.4.2)$$

Thus the pressure port is smaller than the viscous sublayer ($\frac{y}{v\sqrt{\rho/\tau}} = 5$) and is not subjected to Reynolds stresses. Therefore errors of this nature are not expected.

3. The Helmholtz-Resonator

The Helmholtz resonator provides a convenient method for reducing the active sensing area of the transducer, but also introduces a resonant frequency into the overall transducer response. The origin of this resonance is mechanical sharing of energy. The energy oscillates between kinetic energy of the fluid in the resonator throat and the compressional potential energy due to the compliance of the fluid in the cavity and the crystal (it was found that fluid and crystal compliance were of the same order). The height of the resonant peak is limited by the viscous damping. Below resonance, the system is stiffness-controlled, resulting in a one to one correspondence between the pressure at the resonator throat and the pressure at the crystal-liquid interface. Above resonance the system response must fall off due to the combination of mass controlled response and breakdown of the lumped parameter model. It is important to ensure that the resonant frequency occurs above the highest frequency of interest

because resonant response tends to be variable. Therefore, the larger the resonant peak, the farther one would like it from the frequency range of interest. The calibration procedure and results are discussed in the next section.

4. Calibration Procedure and Results

Before calibrating or using the transducer, all gas bubbles must be removed from the resonator cavity. The smallest bubble would greatly increase the compliance of the Helmholtz resonator system, and thus decrease the resonant frequency. The purge was accomplished by submerging the transducer tip in the working fluid (silicone oil) and then reducing the ambient pressure to the vapor pressure of the oil. This procedure removed all dissolved and undissolved gases from the resonator. After allowing the resonator to "boil" for one hour, the ambient pressure is returned to atmospheric, whereby the vapor cavity in the resonator becomes insignificantly small. Such a procedure was followed before each use of the transducer. Surface tension prevents bubbles from entering the cavity during mounting procedure.

The actual calibration procedure was accomplished by rigidly attaching the transducer to a fixed body (see Fig. 15). Then a container of oil is raised to submerge the transducer tip to a depth h . Then the oil bath is oscillated and swept through the frequency band of interest. The pressure at the tip of the transducer is simply related to the acceleration of the fluid by the relation:

$$p = \rho a h \quad (2.4.3)$$

Thus by suitably instrumenting the oscillating bath a calibration can be performed. The details of this procedure will not be discussed. Those interested are referred to the Ph.D. thesis of Victor Nedzilnitsky (M.I.T.; to be published) where a detailed account of this procedure is described.

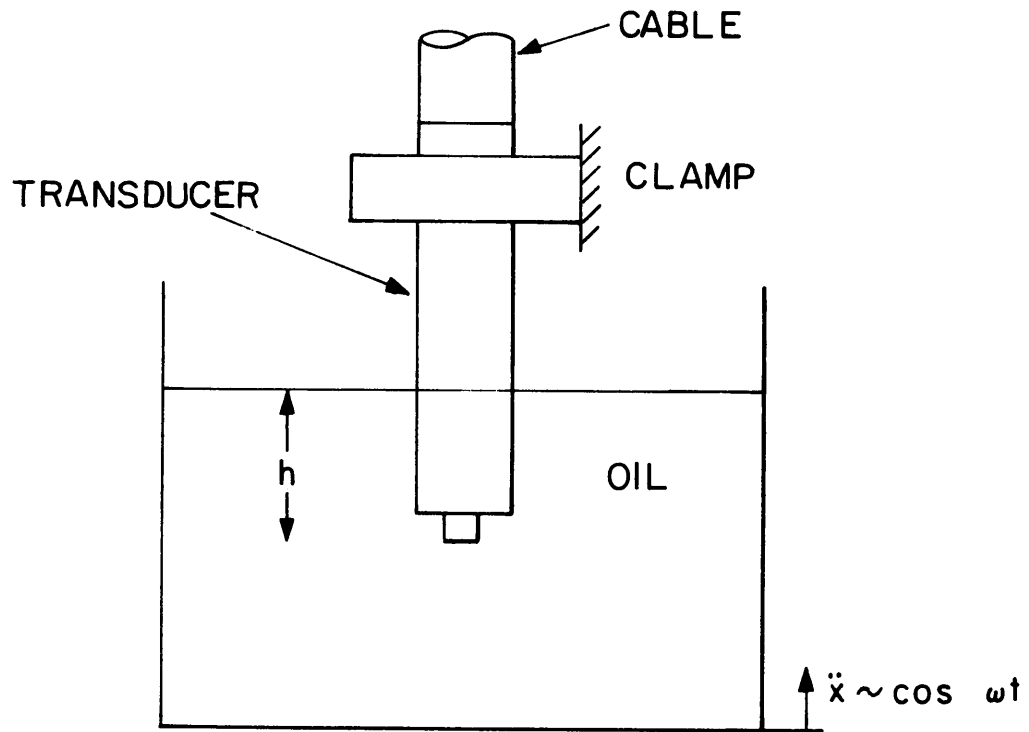


Fig. 15. Transducer calibration procedure .

These results were double checked independently by comparing the response of the transducer with the response of a similar transducer whose response characteristics were determined by means of pistonphone calibration.

The curves of Fig. 16 represent inverse frequency response calibrations hence resonance appears as a depression in the curves. The difference in absolute level of the two curves is attributed to an error in the depth of the probe in the oil bath. When the error is compensated for, the following overall sensitivity is obtained

$$-114.5 \text{ dB re } 1 \text{ volt}/\mu \text{ bar}$$

or

$$1.88 \mu \text{ volts}/\mu \text{ bar} .$$

As can be seen, a resonance occurs at approximately 5KHz and 10 KHz , respectively for the two different viscosity oils. The resonant peak clearly depends upon fluid damping. Since the resonant peaks are relatively small (highly damped system) and are above the highest frequency of interest (3KHz) their presence does not pose a problem in data reduction.

5. Transducer Mounting

The transducer, as shown in Fig. 14, is threaded to allow for easy mounting and dismounting. The transducer is mounted in the test section as shown in Fig. 17. A brass mounting plate is built into the tube wall. The inner surface of this brass plate is tangent and flush with the inner radius to within .002". The transducer is screwed into this mounting plate with the active sensing area flush with the inner radius.

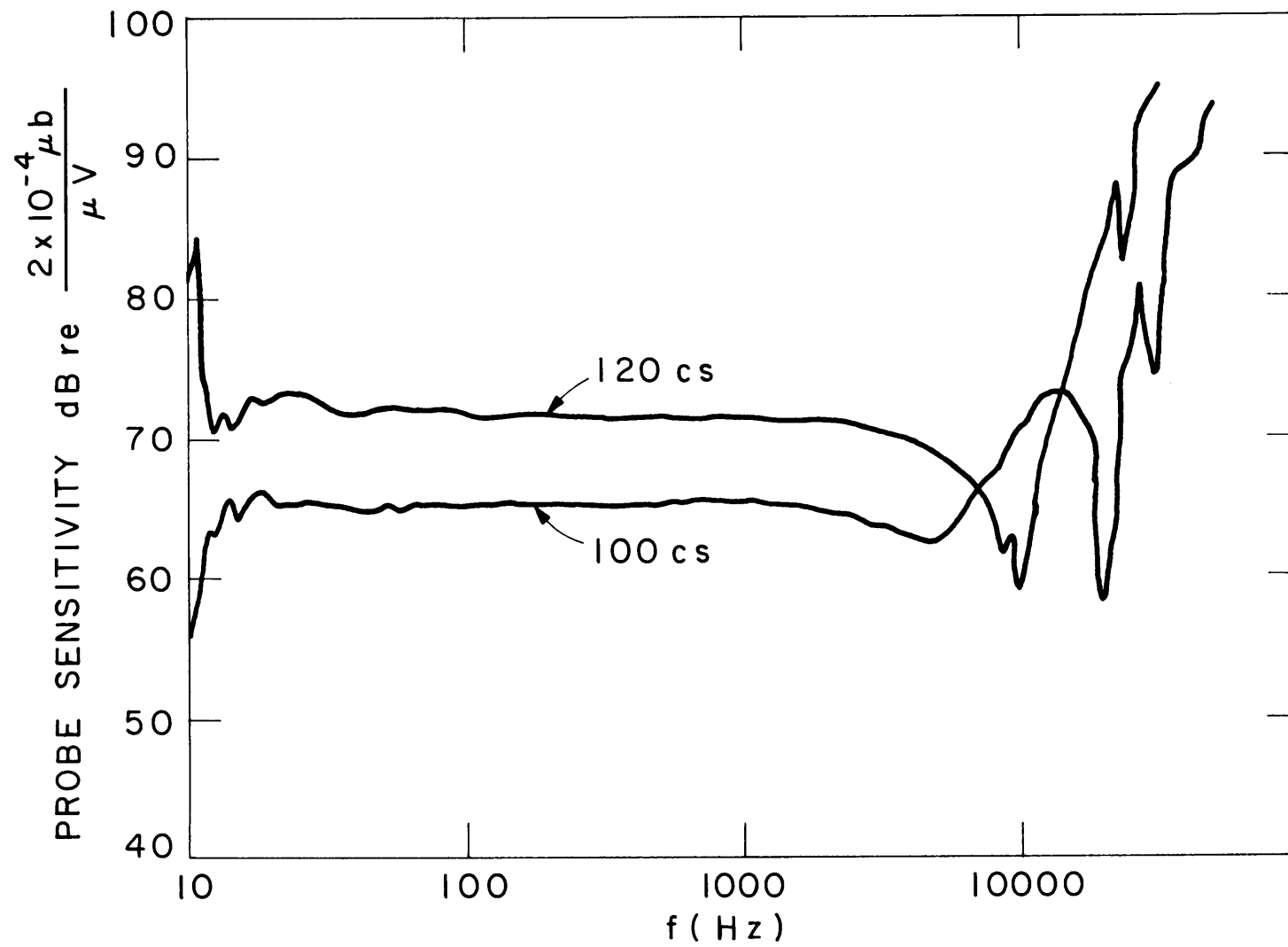


Fig. 16. Transducer calibration.

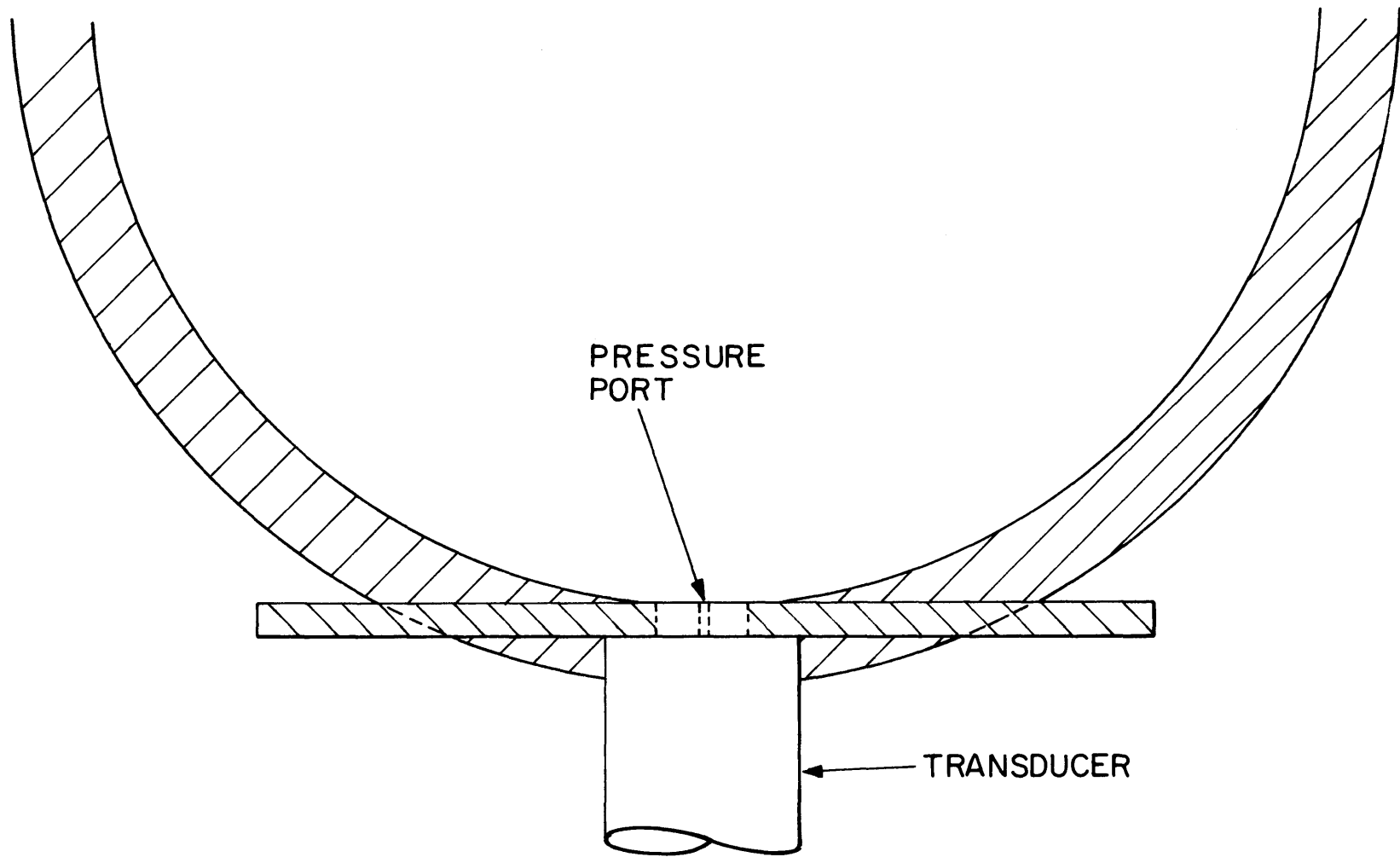


Fig.17. Transducer mounting in the test section.

3.5 Artifact Checks

1. Pump Noise

The transmission of noise from the pump to the test section is the limiting factor in determining the maximum signal to noise ratio possible for any flow condition. Below or at critical Reynolds number, when the turbulent pressure fluctuations are vanishingly small, the signal from the pressure transducer can be amplified and shown to consist solely of conducted pump noise ($S/N = 0$). As the flow conditions are changed so that the turbulent wall pressure fluctuations become larger, the S/N becomes larger. In the cases where the S/N is thought to be large, a simple check can be performed to test this hypothesis.

One can shut off the pump and run the experiment from the charged capacitor for a short time. Comparing signals immediately before and after pump shutdown showed no difference in total intensity or spectral distribution, indicating that pump noise was not contributing a significant amount of energy to the signal.

2. Vibration Sensitivity

Another possible source of error is that a significant fraction of the transducer signal could be due to vibration of the tube wall accelerating the transducer. To estimate the fraction of the transducer signal caused by acceleration sensitivity a dummy transducer was mounted in the test section. The real transducer was rigidly attached to the dummy transducer. In this configuration the real transducer is subject only to vibration, with no pressure fluctuations present at the active sensing port. Upon running the pump, it was found that the transducer output in this configuration, normalized by the signal obtained when the transducer is properly

mounted and exposed to the same turbulent flow, was less than -60 dB.

Thus vibration response can be neglected.

3.6. Viscosity-Temperature Calibration

The viscosity of the working fluid should be fixed and well known for any one experiment. In the flow loop described in Section III C, the rate of increase of viscosity of the working fluid depends on the power being dissipated in the fluid loop, the volume of fluid in the loop, the specific heat, and the viscosity-temperature relation of the fluid. Since temperature does not change significantly over the period of data sampling, or spatially through the loop, the temperature of the fluid provides a convenient running measure of the viscosity if the temperature-viscosity relation is known. This relation was measured for the working fluids with a Saybolt-Tag thermostatic viscometer. The results are shown in Fig. 18. The solid line represents the manufacturer's claimed viscosity-temperature relation.

3.7. Data Collection and Processing

The scheme used for data collection is depicted in Fig. 19. A unity gain field effect transistor circuit is incorporated in the transducer assembly so that the piezo-electric crystal drives into a high impedance without intermediate transmission lines. The transducer output is connected to a Princeton Applied Research 113 preamplifier, 110 megohm input impedance in parallel with 15 picofarads. The output of the first preamp leads to a high pass filter circuit. Since the signals of interest are heavily weighted towards low frequency, the high frequency part of the spectrum can be lost below noise in the tape recording process. Therefore the signal is filtered,

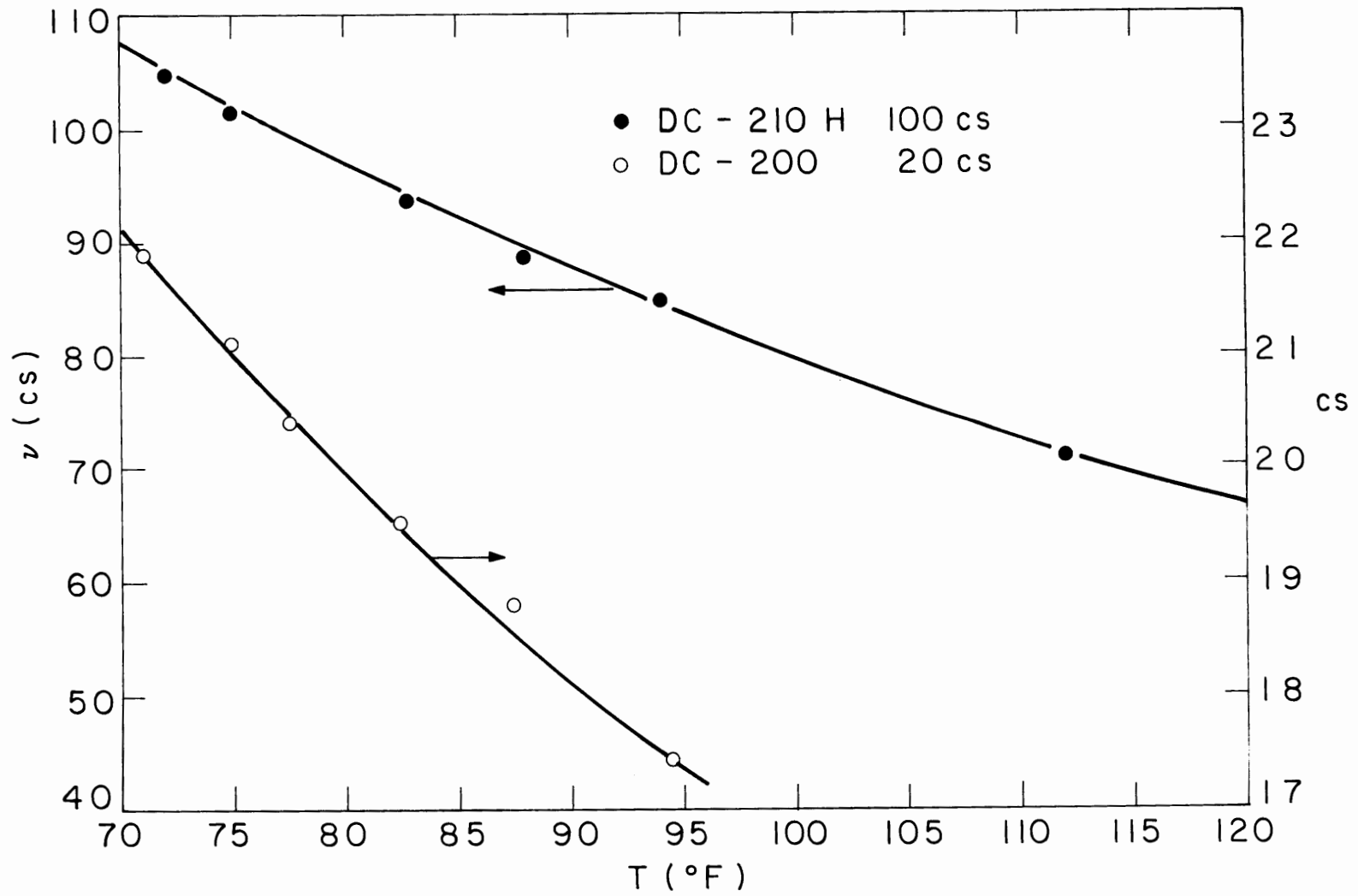


Fig.18. Temperature -viscosity relations for the working fluids.

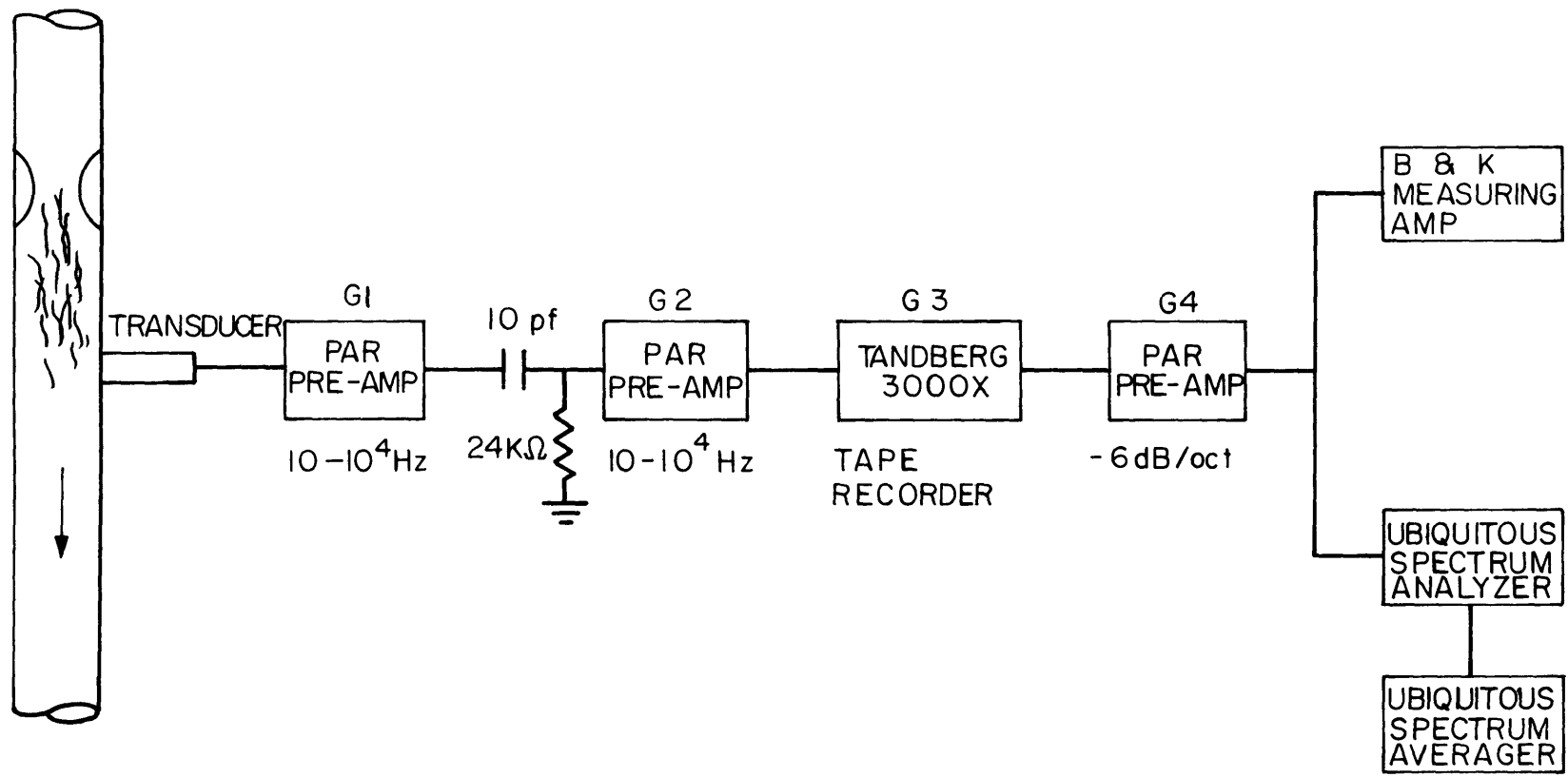


Fig. 19. Data processing scheme.

or "pre-whitened" so that the high frequency side is boosted relative to the low frequency side. This allows the entire spectrum to be recorded on tape without as much loss of high frequency information. Of course, the effect of this filtering is corrected in a later stage of processing.

The high pass filter leads to another PAR 113 preamp, which in turn leads to a Tandberg 3000x tape recorder. The overall system response from the first preamplifier through the tape recorder is shown in Fig. 20, which is a gain-dependent normalization of the output voltage of the tape recorder divided by the input voltage to the first preamplifier.

The output of the tape recorder is again connected to a PAR 113 preamp, whose output can be connected to analysis equipment. The amplifier high pass 3 dB rolloff point is set at 30 Hz. This provides 6 dB/octave attenuation, and restores the spectral distribution of energy to its condition before prewhitening.

Rms measurements were made on a B&K 2607 measuring amplifier, bandwidth 22.5 Hz - 22.5 KHz . This measuring device permitted averaging times of up to 15 sec.

Spectral analysis was accomplished with a Federal Scientific model UA-15A Ubiquitous Spectrum Analyzer, and Model 1015 Spectrum Averager. The amplitude calibration of the spectrum analyzer as outlined by the manufacturer was found to be faulty. Spectra of white and filtered noise were graphically integrated to determine if the rms value so measured agreed with the rms value of the same signals measured with a B&K true rms meter and a B&K measuring amplifier.

It was found that the integrated spectra did not sum to the proper rms value. By carefully plotting and integrating the spectra of signals

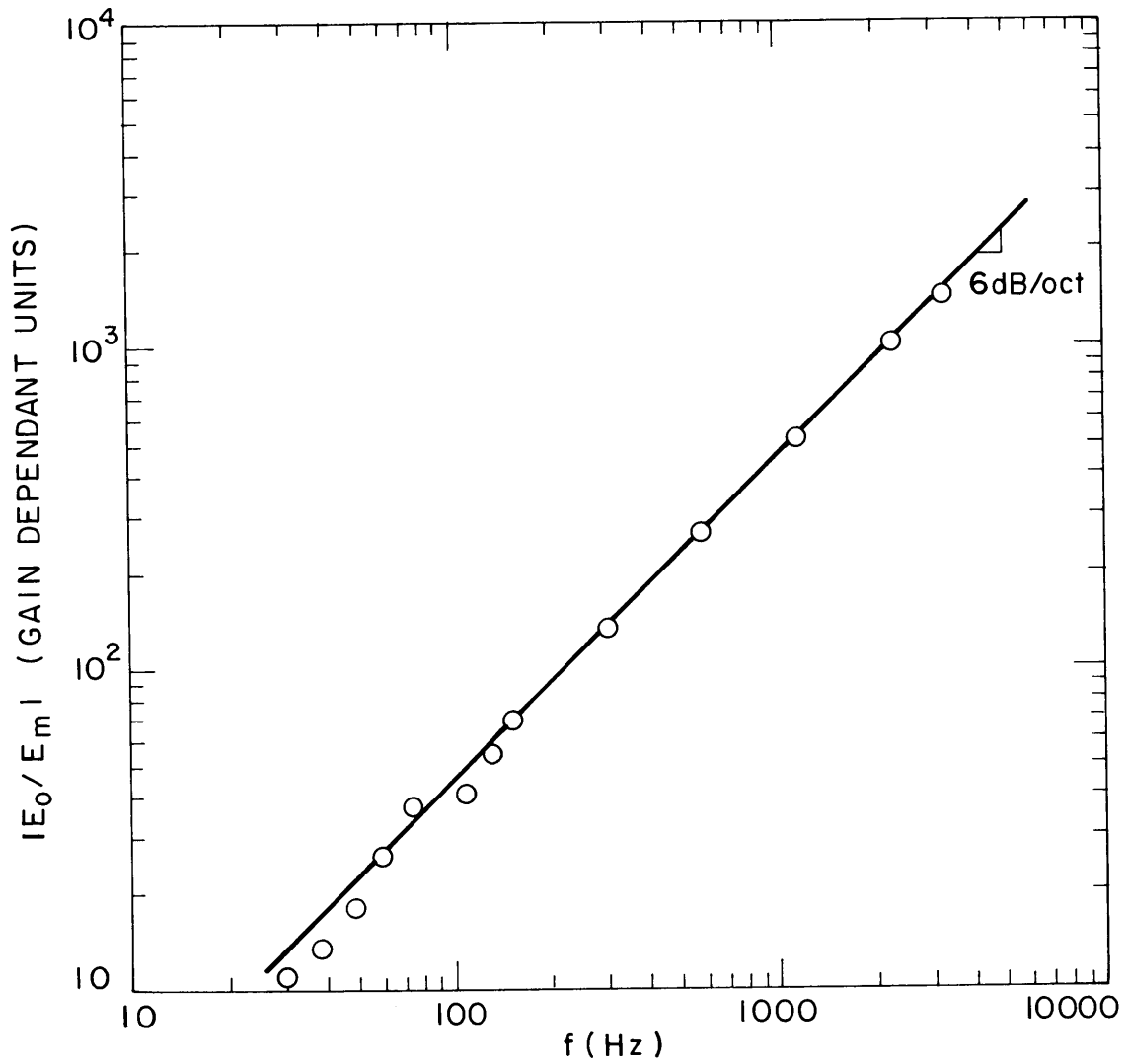


Fig. 20. Output voltage of tape recorder divided by input voltage to first (variable gain) preamplifier.

of known power spectral densities it was determined that the output of the spectrum analyzer was low by a constant multiplicative factor. This attenuation was accounted for in the data reduction.

The effective bandwidth of the analyzing filter was found by plotting the response to a pure tone input signal as its frequency changed. It was found that the effective bandwidth of the analyzing filter was 16 Hz when the analyzing bandwidth was set at 5 KHz.

3.8 Previous Investigations

A number of investigations of various aspects of relatively low Reynolds number flow through constricted tubes are reported in the literature. The emphasis in most of these reports is placed on development of pressure-flow characteristics, while to a lesser extent separation and reattachment data, visualization studies, and pressure fluctuation data are reported. In addition there have been a number of investigations into the origin of vascular murmurs.

Among this body of literature, one of the earliest and most definitive reports, by Johansen (1929), was intended to provide data for use in orifice plate flowmeters. To a large extent the remainder of the relevant work in the area of flow through constricted tubes is found in the medical literature and was motivated by desire to understand flow through constricted arteries.

The relevant conclusions and observations reported in this body of literature will be briefly reviewed and divided into two categories:

1) flow through constricted tubes, and 2) origin and onset of vascular murmurs.

1) Flow through constricted tubes. Johansen (1929) performed a series of flow visualization and pressure drop studies on flow through a sharp edged circular orifice in a pipe. From these visual studies he provides an excellent qualitative description of the sequence of events that occur as the jet Reynolds number increases. These qualitative descriptions will be summarized because of their relevance to the present work:

$Re_j < 10$	Axisymmetric, laminar, steady flow, no separation.
$Re_j \approx 30$	Separation begins to occur, laminar steady
$Re_j \approx 100$	Separation region becomes longer, laminar steady flow persists. A permanent stationary captured eddy appears.
$Re_j \approx 150$	Separation region extends 5-6 diameters (maximum value), laminar, steady flow, becomes unstable to external disturbances.
$Re_j \approx 250$	Regularly spaced instabilities begin to appear at the boundary of the jet.
$Re_j \approx 1000$	Ring vortices convect approximately 5 pipe diameters, then become unstable and break down into general turbulent motion.
$Re_j \approx 2000$	Fully turbulent, separation region rapidly decreases to approximately 1 diameter.

Johansen also stated that "the phenomena described occurred with all sizes of orifice, and in the same order, though not quite at the same (jet) Reynolds number. The value of (jet) Reynolds number for a given event or type of flow was found to increase progressively as d/D was increased".

Young and Tsai (1970), performed pressure drop measurements and visualization studies for steady flow through a smooth (as opposed to sharp) edged circular orifice. The data shows the tendency for the separation region to grow with increasing Re_j for $Re_j < 1000$, but does

not extend enough in Re_j to see the separation region attain a maximum value and then become smaller. They report transition to turbulence at $Re_j = 1200 - 1400$, which is similar to the range reported by Johansen.

Golia and Evans (1973) performed visualization studies on the onset of separation and the separation region downstream of a circular smooth edge orifice, and studied the effects of varying the radius of curvature of the orifice lip. Their experiments extend to Re_j up to approximately 1500, and show a similar increase in length of the separation region as reported by Young and Tsai. The data appears to be relatively insensitive to changes of orifice radius of curvature for their experimental range $1/4 < d/4a < 1$. They did not observe turbulence.

Back and Roschke (1972) studied reattachment of a jet downstream of a sudden expansion for a wide range of jet Reynolds numbers, and found the maximum reattachment length of 8 diameters at $Re = 300$. Beyond this Reynolds number the reattachment length rapidly decreases to a minimum value of about 2 diameters.

Some of the most relevant work done in related areas unfortunately is also the most disappointing. Rouse and Jezdinsky (1966) performed a series of experiments on the structure of the turbulent wall pressure field downstream of a sudden expansion in area in a circular pipe. They measured the rms pressure as a function of downstream distance, and wall pressure spectra at the point of maximum intensity for 3 diameters ratios. Qualitatively their rms pressure versus d/D findings look quite similar to the findings reported in this research (Section III) both in amplitude and downstream scaling. Unfortunately Reynolds number is not reported, so

their data cannot even be plotted with the current rms data in Section III.

Rouse and Jezdinsky also report lateral and longitudinal correlations of the pressure field, not reported in the present research. Unfortunately, the spectral data reported by them is rendered useless by the fact that the transducer sensing area is not specifically noted. They quote "1/8 piezometric openings", which if intended to be the size of the active sensing element, would correspond to $\omega d_t / U_c \gg 1$, which implies huge errors in the spectral measurements. (See Section III.4.2.)

Maybe (1972) studied the wall pressure field in general separated flows, including a sudden enlargement in a pipe. He quotes a general result for separated flows

$$0.1 < \frac{P_{rms}}{\frac{1}{2}\rho u^2} < 0.04$$

which is consistent with the findings reported in Chapter III for high Reynolds number only. Unfortunately the rms and spectral results of Maybe are subject to question because he does not report Reynolds number or transducer size. As with Rouse and Jezdinsky (1966), Maybe's rms data as a function of X/D qualitatively agrees with findings in the current research.

Fricke (1971) performed a series of experiments on the turbulent wall pressure field in separated flows. Fricke concludes that wall pressure fluctuations in subsonic separated flows are an order of magnitude higher than those beneath a boundary layer. Unfortunately, Fricke also fails to report Reynolds number.

Other related investigations have been performed by Robbins and

Bentov (1967), and Young and Forrester (1970),

2) The Origin of Vascular Murmurs. The earliest work in the area of vascular murmurs was done by Bruns (1959) who felt that periodic vortex shedding was responsible for the observed sound, and Rushmer and Morgan (1960), who observed that vascular murmurs have a broad spectrum and do not have discrete frequency tones as would be expected from vortex shedding.

Yellin (1966) was the first investigator to study pressure fluctuations within the confined jet, and the first to appreciate that vascular "sounds" are not sounds at all; rather they are tissue vibrations which are perceived as sound by the pressure transduction process (see Chapter II). He also points out that the dominant mechanism for vibrating the surrounding tissue is the collision of turbulent eddies with the wall. By placing a pressure probe into the jet flow downstream of an orifice, rms and spectral distribution of the signal from the probe were obtained. Off-axis measurements showed a peak rms value occurring as far as 14 diameters downstream. The data reported were consistent with the broad spectral nature of turbulent spectra.

Sacks et al. (1971) performed a series of dog experiments to determine the conditions for onset of vascular murmurs. By implanting a square-edged circular orifice plate assembly in the aorta of dogs, and inserting a catheter tip microphone in the flow downstream of the orifice, he measured the onset of turbulence-induced pressure fluctuations. The data were fitted by the equation

$$(Re_j)_{cr} = 2384 \left(\frac{d}{D}\right) \quad (3.7.1)$$

with reasonably good agreement. As noted by Sacks, this result is consistent with Johansen's (1929) observation that the critical value of Re_j for some event to occur was found to increase progressively as d/D was increased. However the threshold criterion used to determine onset was not specified. Therefore Sacks' data actually represents an iso-intensity criteria for low intensity, but since the onset of turbulence occurs rapidly as Re_j is increased, Sacks' estimates probably only slightly overestimate the critical Reynolds number for that orifice geometry. However, the onset of turbulence-induced pressure fluctuations in the flow, as reported by Sacks, and the onset of detectability of vascular murmurs are not the same problem. This is discussed in Section 5.2.

Chapter IV Experimental Results

The results of the experiments will be discussed in three sections

- A) Normalization of rms measurements
- B) Normalization of spectral measurements
- C) Interpretation of A and B

The objective of Section C is to coalesce the scaling laws demonstrated in parts A and B into a meaningful understanding of the relevant physics.

4.1 Normalization of rms Data

The root mean square wall pressure downstream of a stenosis was measured at different distances from 5 stenoses over a wide range of Reynolds number. The result of these measurements are presented in nondimensional form in Figs. 21-25. It was observed that the distance to the peak of the rms wall pressure tends to increase as the Reynolds number decreases. In addition, the decay of intensity in the downstream direction following the peak is much steeper at high jet Reynolds number. At high Reynolds number it was found that the peak rms pressure normalized by the jet kinetic energy/volume tended to become independent of Reynolds number.

The value of the rms pressure at the downstream position where it attains its maximum value is plotted as a function of jet Reynolds number in Fig. 26. At low Re_j the peak rms pressure has disparate Re_j dependence. In addition, at low Re_j , the diameter ratio d/D , is also important, with small d/D producing a larger rms pressure. At high Re_j both Re_j and d/D become unimportant, and the total root mean square pressure scales as a simple fraction of the jet kinetic energy per unit

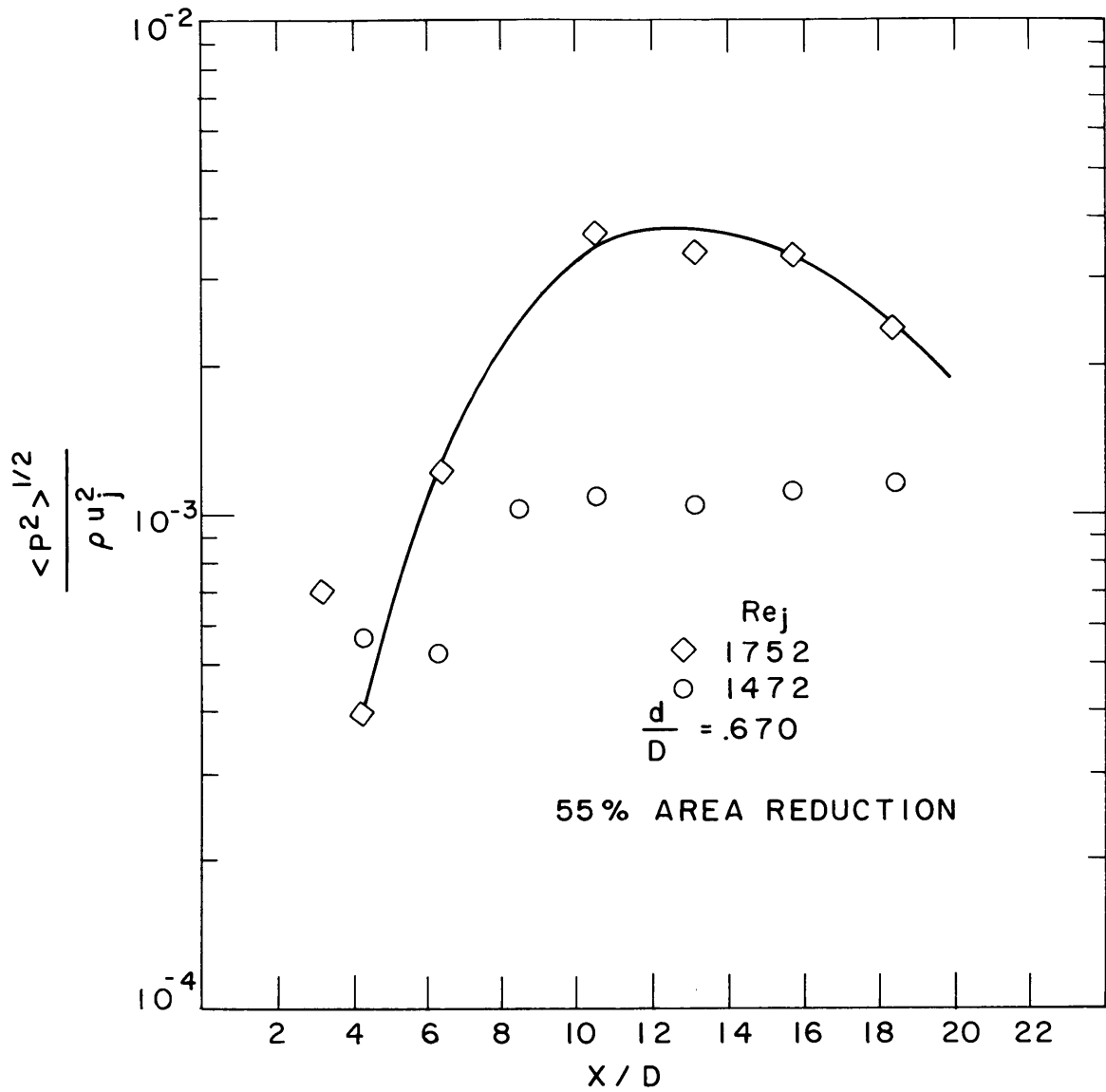


Fig. 21. Rms wall pressure vs. downstream distance with 55% area reduction.

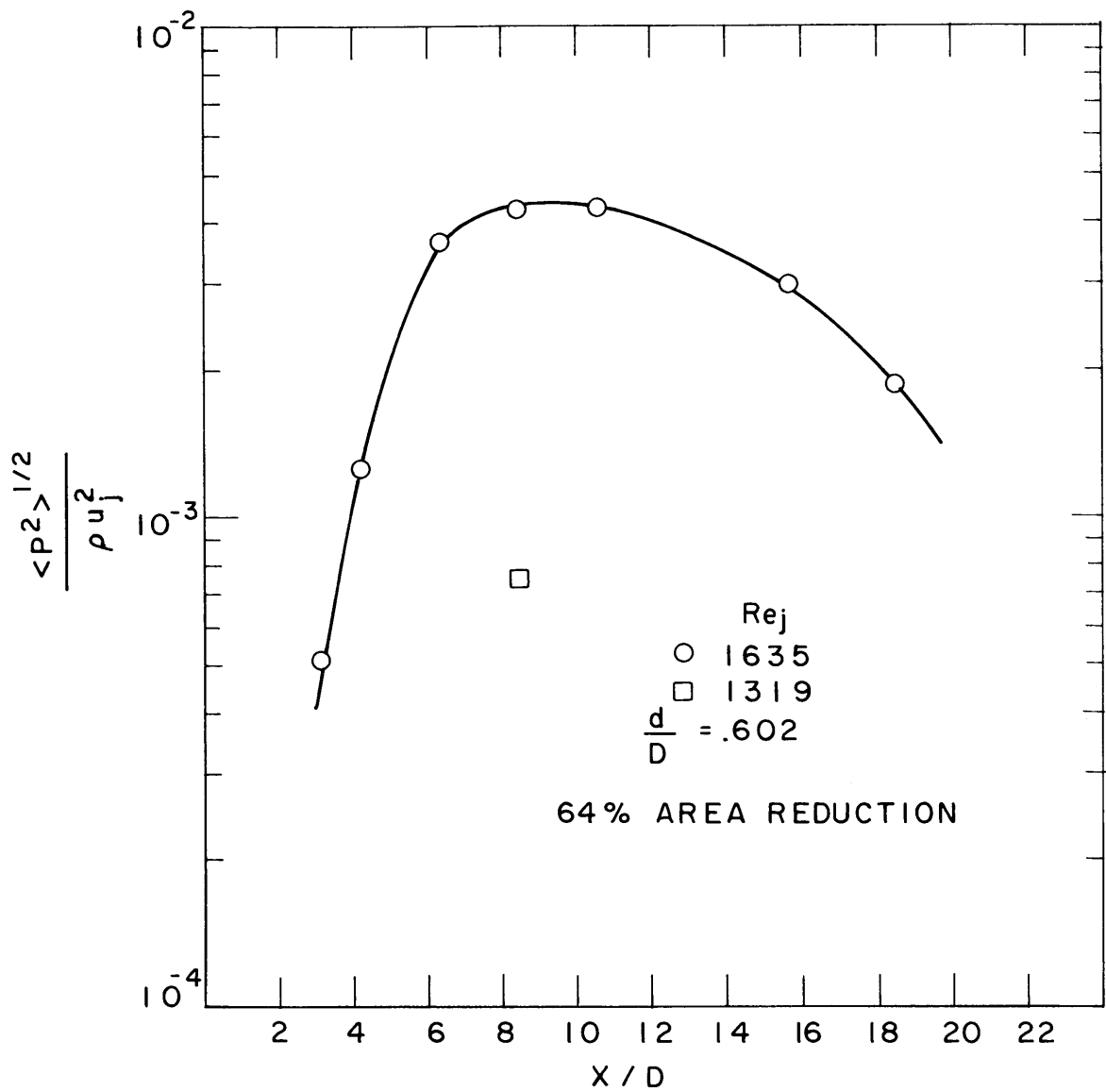


Fig. 22. Rms wall pressure vs. downstream distance with 64% area reduction.

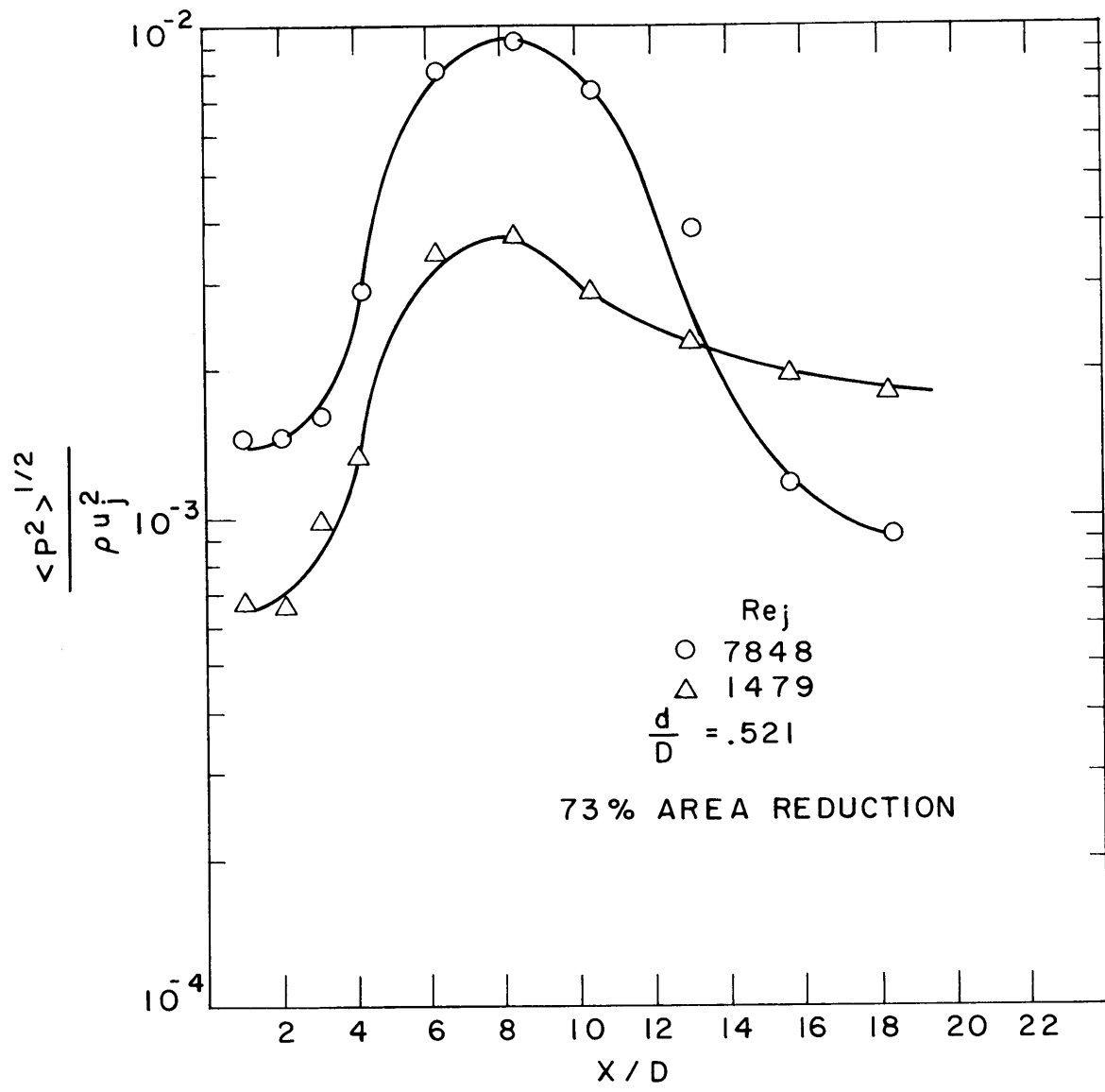


Fig. 23. Rms wall pressure vs. downstream distance with 73% area reduction.

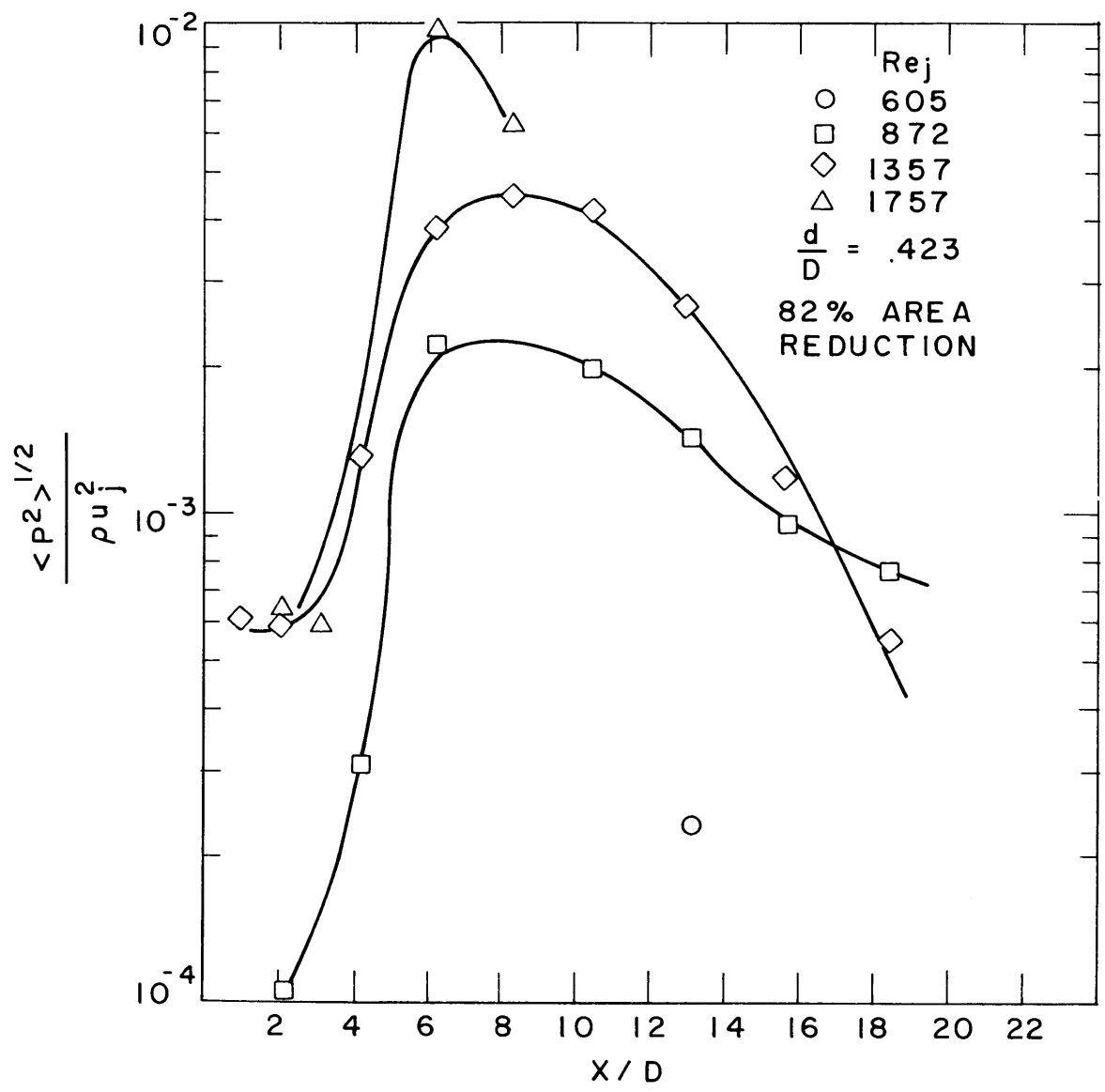


Fig.24. Rms wall pressure vs. downstream distance with 82% area reduction.

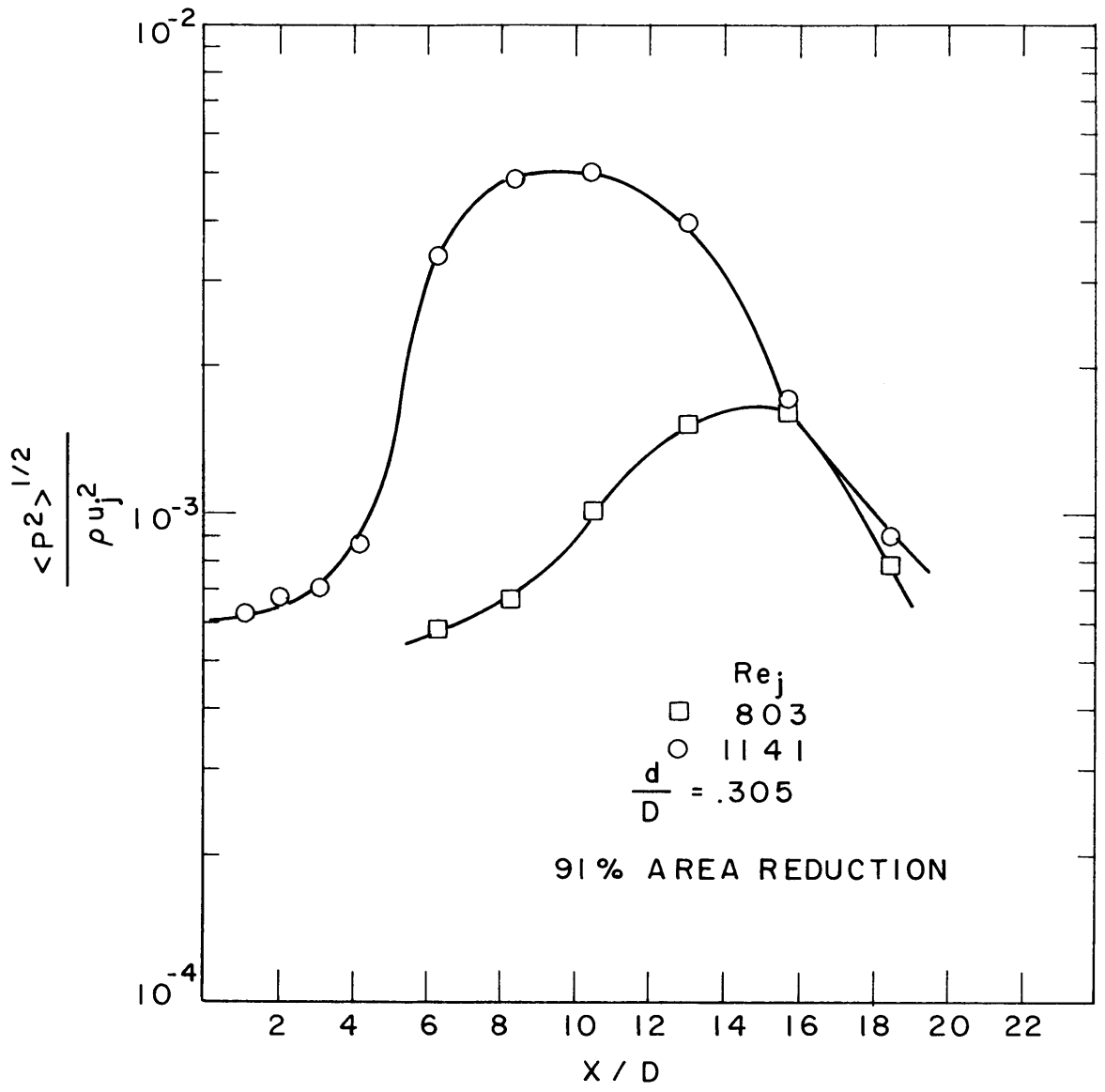


Fig.25. Rms wall pressure vs. downstream distance with 91% area reduction.

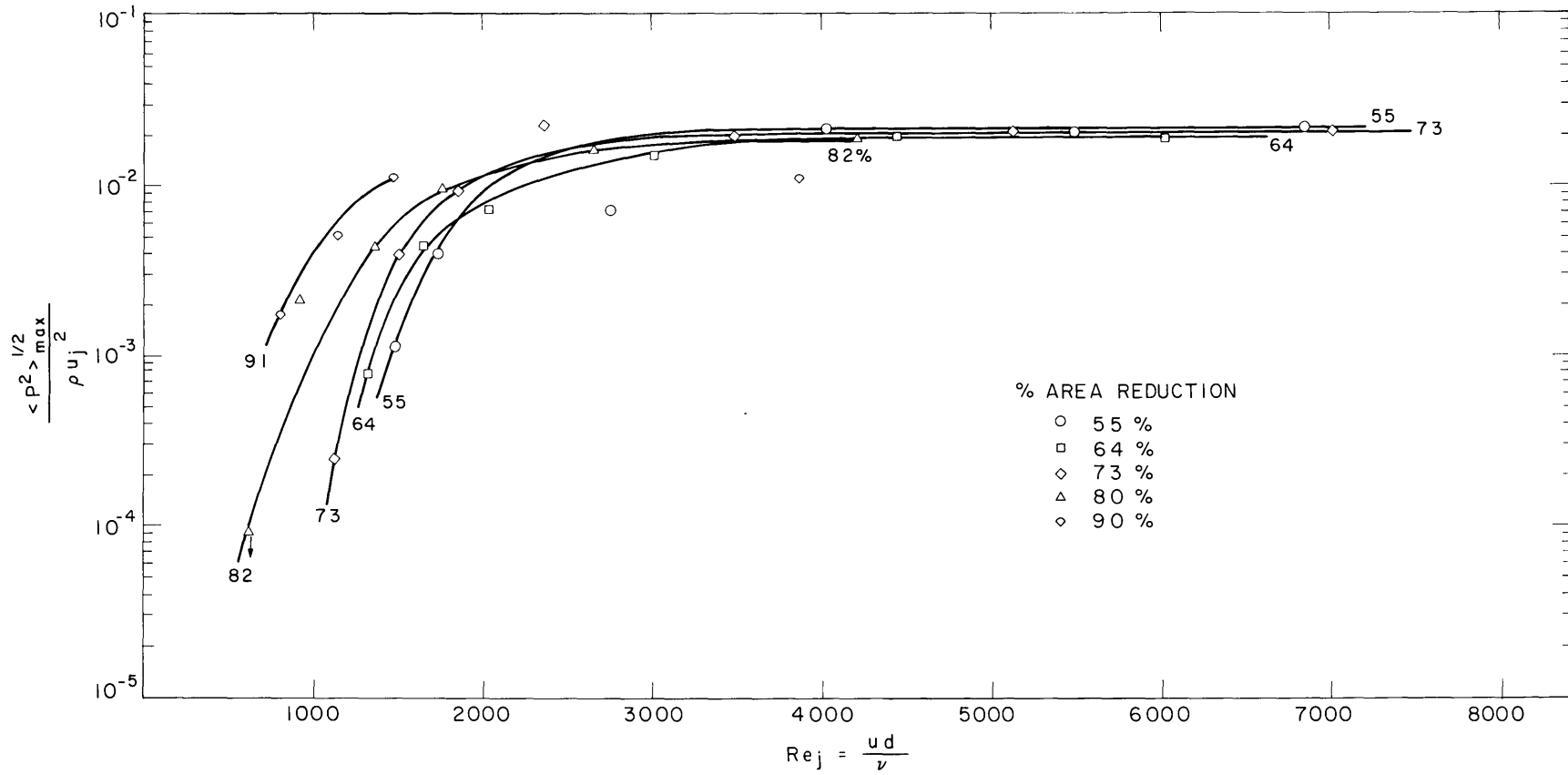


Fig.26. Spatial maximum of rms wall pressure vs. jet Reynolds number and area reduction.

volume

$$p_{\text{rms}}|_{\text{max}} = 4 \times 10^{-2} \left(\frac{1}{2} \rho u_j^2 \right) \quad (4.1.1)$$

By cross-plotting, a correlation can be found to normalize the low Reynolds number rms data. It was found that by plotting normalized rms pressure as a function of $Re_j(D/d)^{.75}$ one can obtain a universal curve, as shown in Fig. 27.

The position at which the peak rms pressure occurs is also of interest. It was found that the characteristic distance for this peak value to occur could be normalized by jet diameter. The results of this normalization are shown in Fig. 28. The implication of this result will be discussed in Section 4.3.

4.2 Normalization of Spectral Data

The power spectral density of the turbulent wall pressure fluctuations was measured at the downstream distance corresponding to the maximum rms value. Thus each of the spectra in this section represents a spectral decomposition of the total energy of each point in Fig. 26. These data are presented in Figs. 29, 30, 31, 32, and 33 for different degrees of area reduction.

It was observed that the total rms pressure was independent of Re_j for high Re_j . Likewise the spectra obtained in this experiment were found to become independent of Re_j for high Re_j . Therefore, high Reynolds number data was studied first to obtain the simplest scaling laws for the spectra.

It was found that the following scaling laws normalized the data

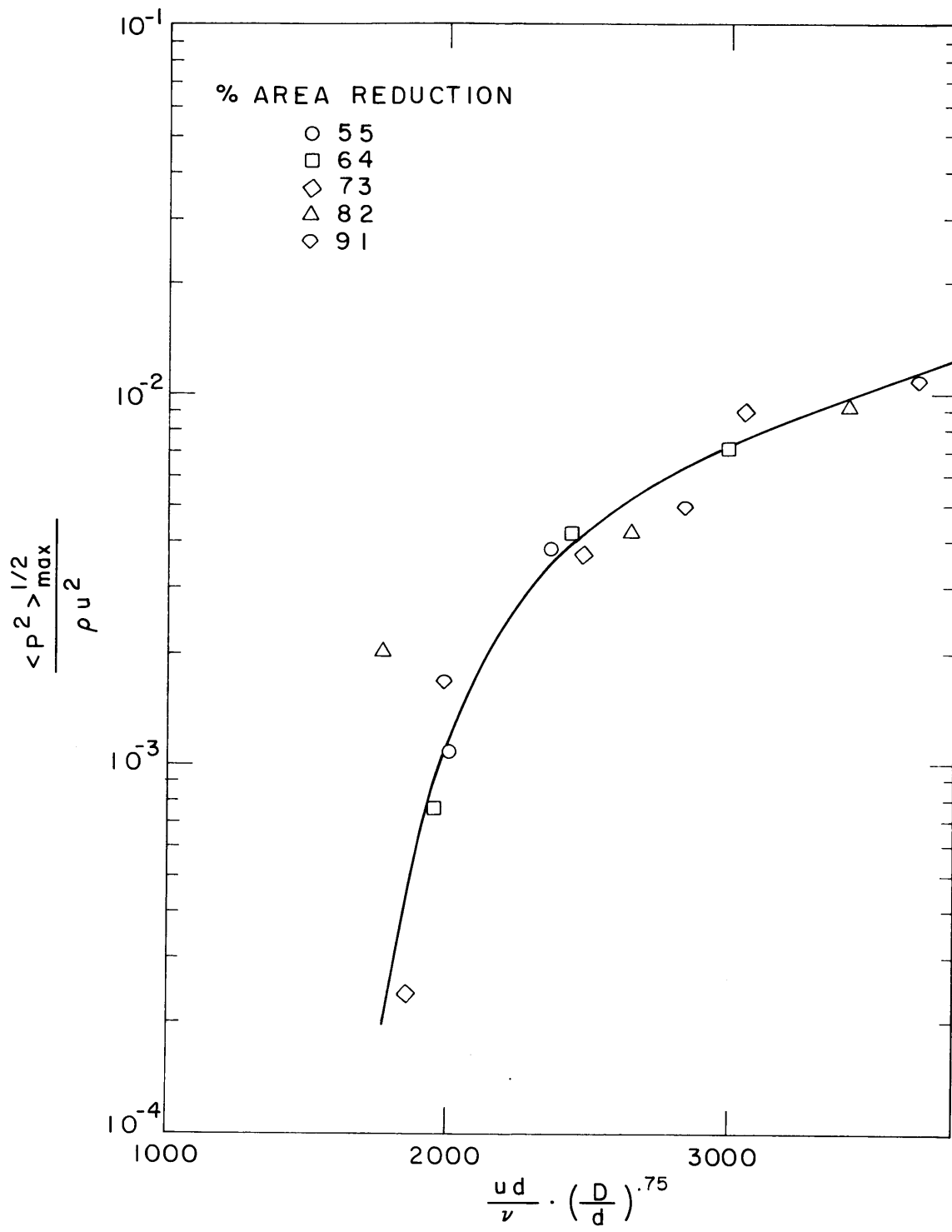


Fig.27. Spatial maximum of rms wall pressure vs. modified Reynolds number.

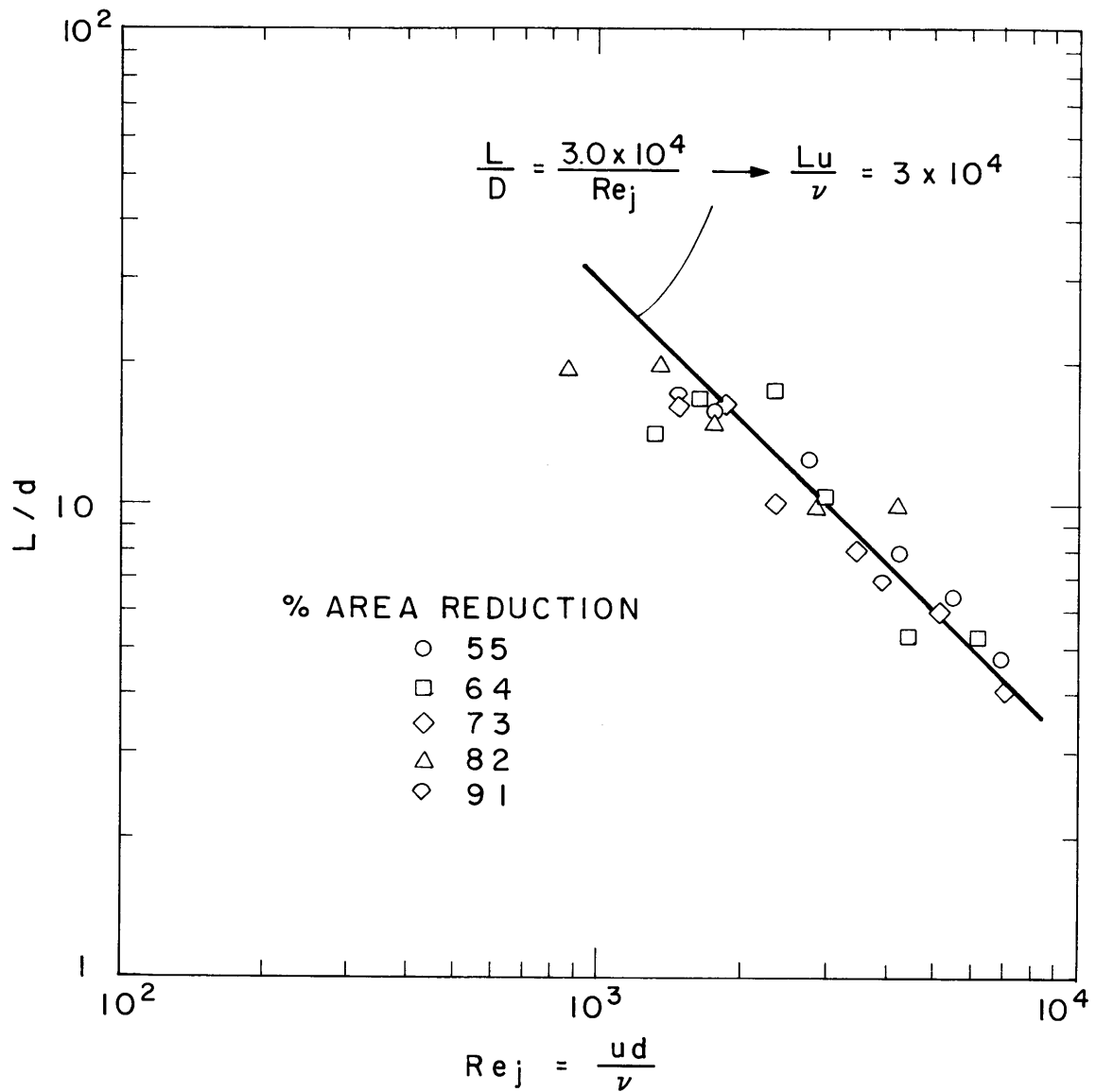


Fig.28. Distance downstream of orifice at which spatial maximum of rms wall pressure is attained, vs. jet Reynolds number.

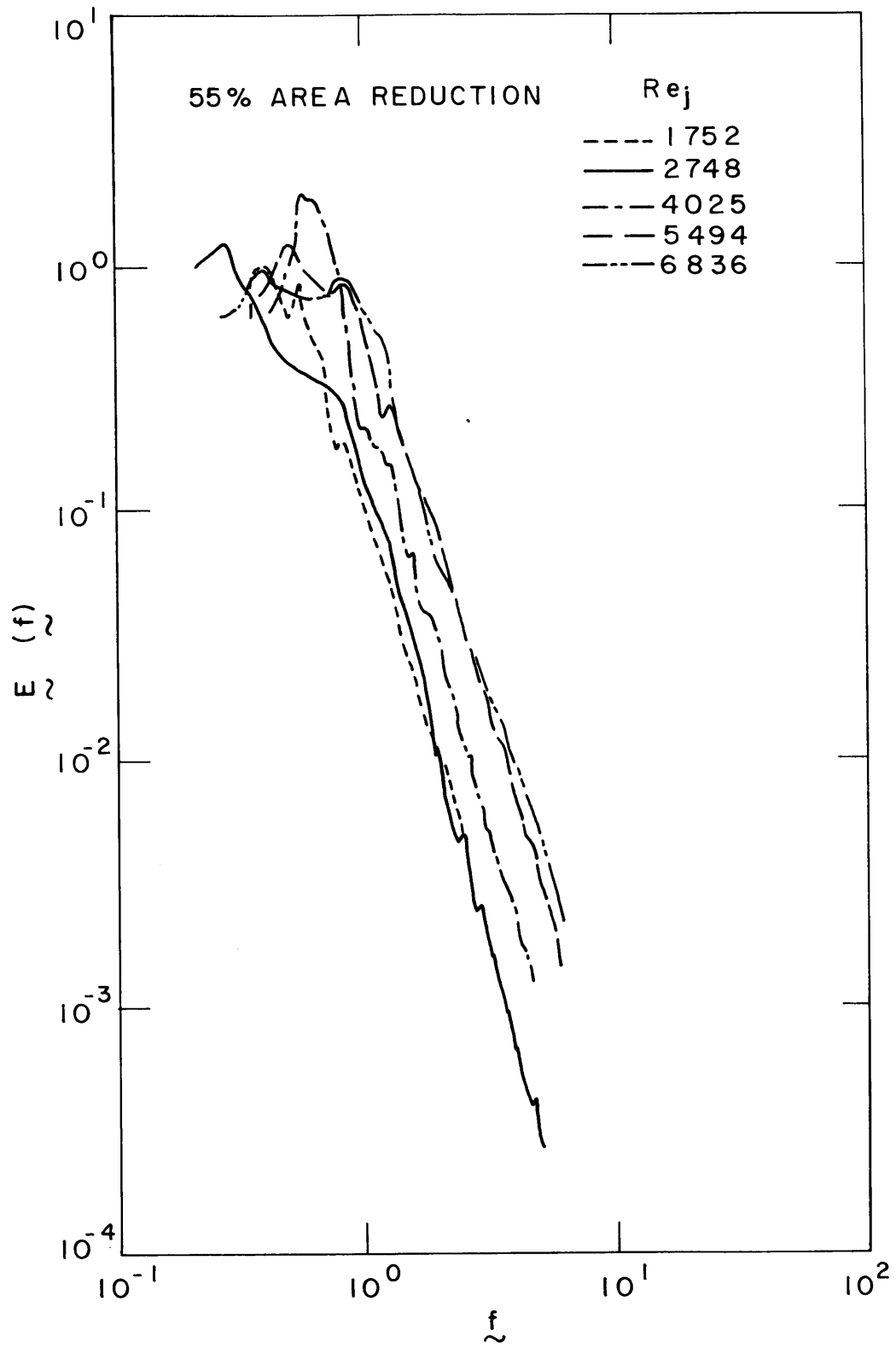


Fig. 29. Nondimensional spectral density of wall pressure for 55% area reduction.

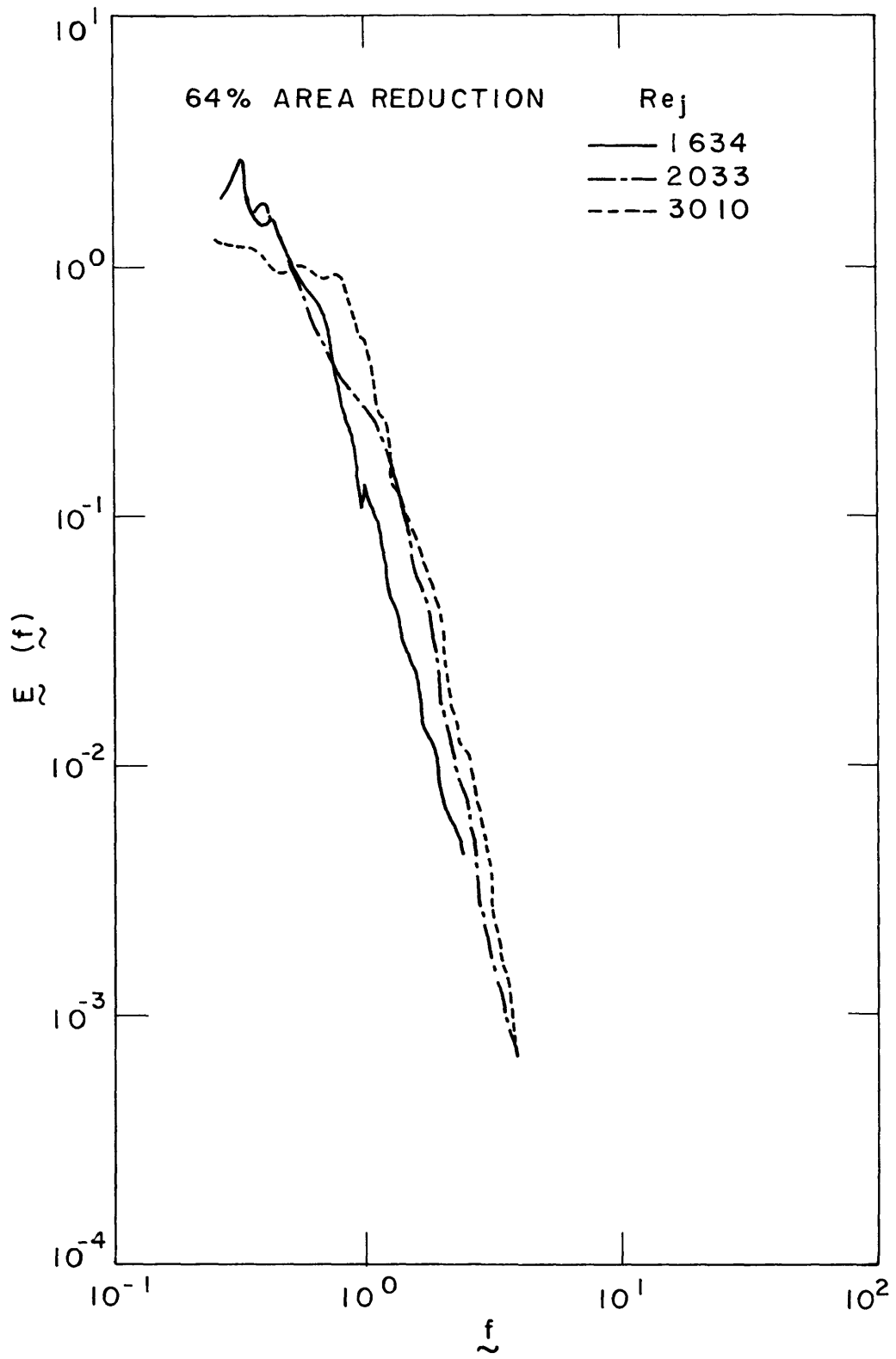


Fig. 30. Nondimensional spectral density of wall pressure for 64% area reduction.

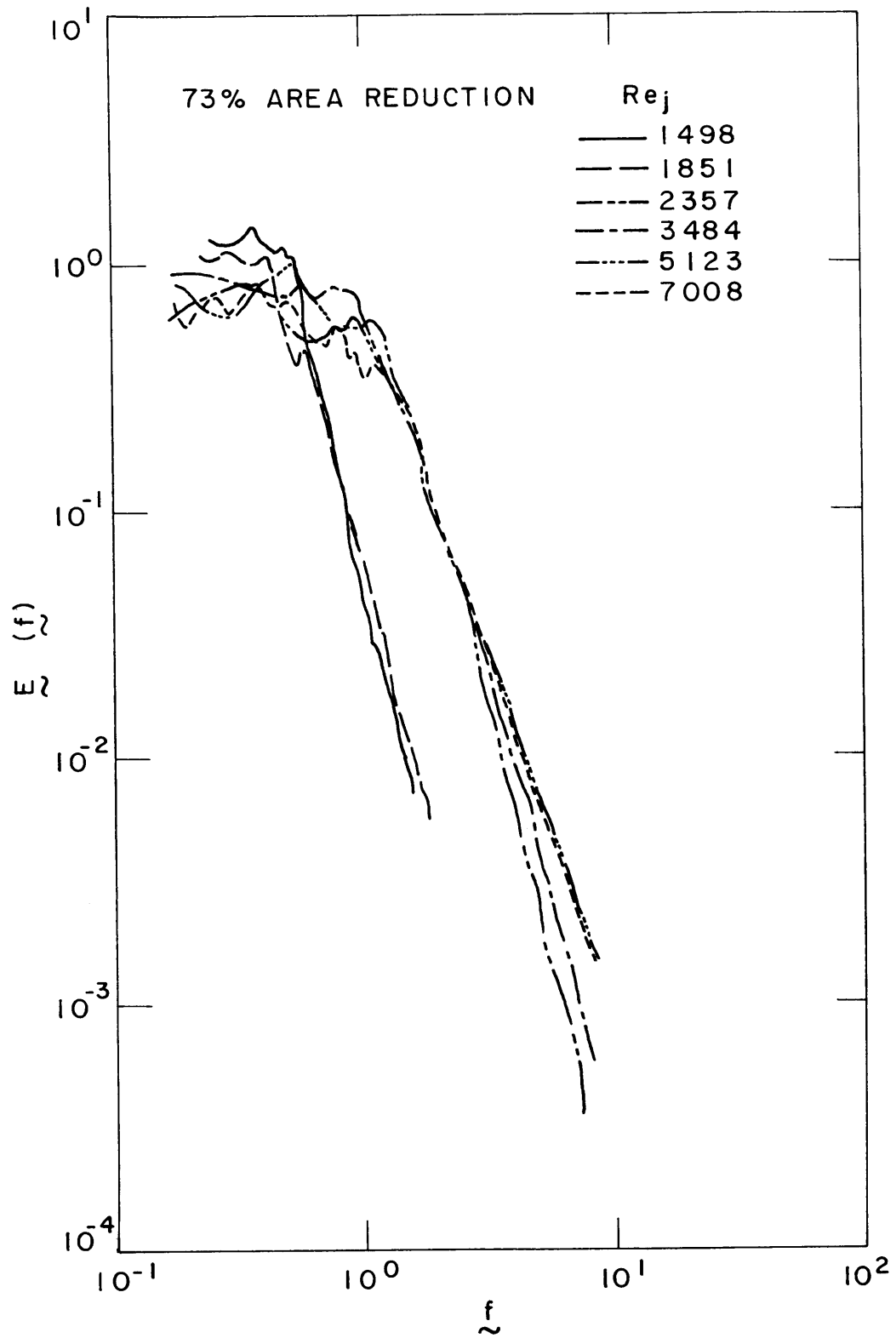


Fig. 31. Nondimensional spectral density of wall pressure for 73% area reduction.

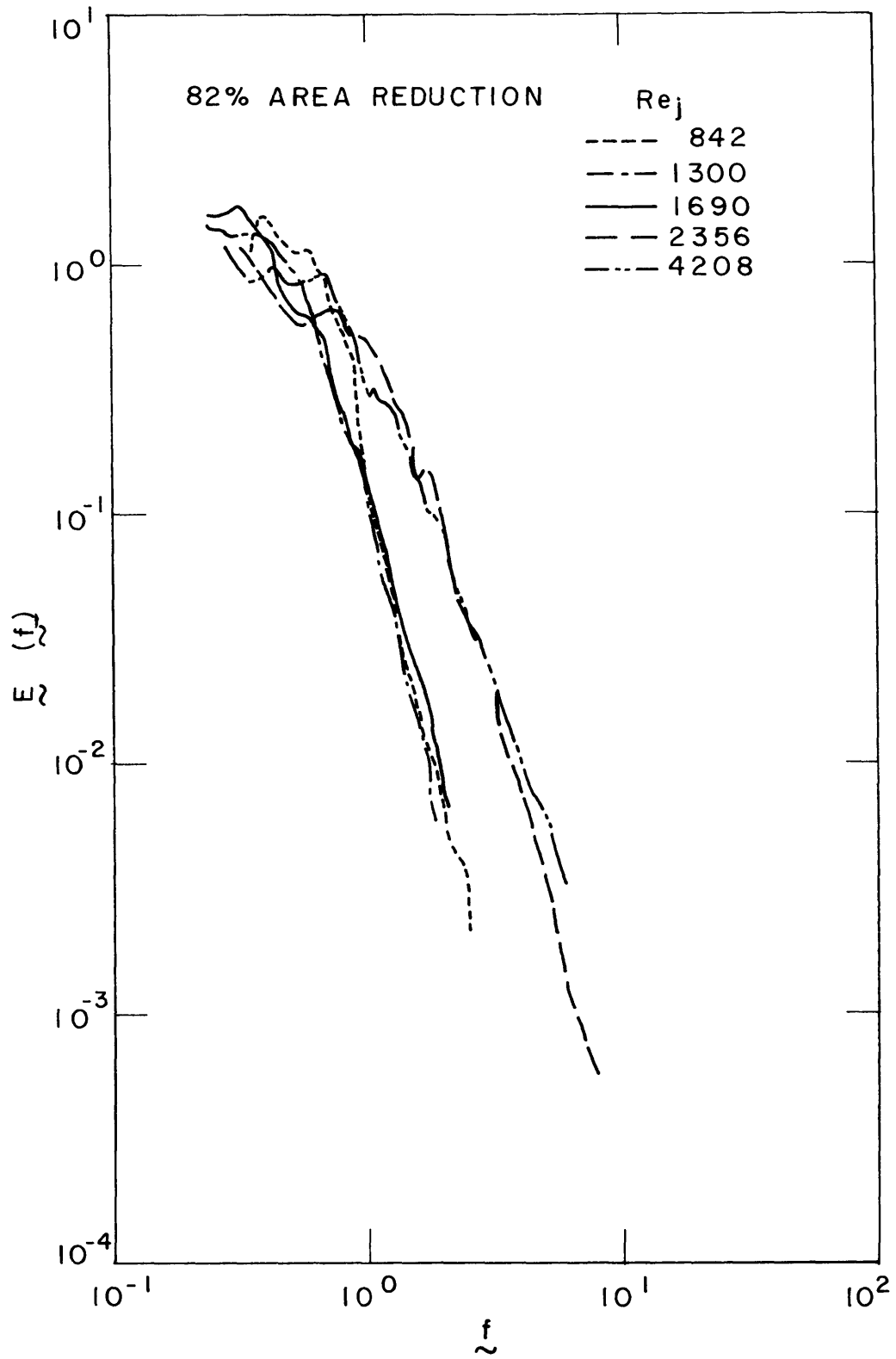


Fig. 32. Nondimensional spectral density of wall pressure for 82% area reduction.

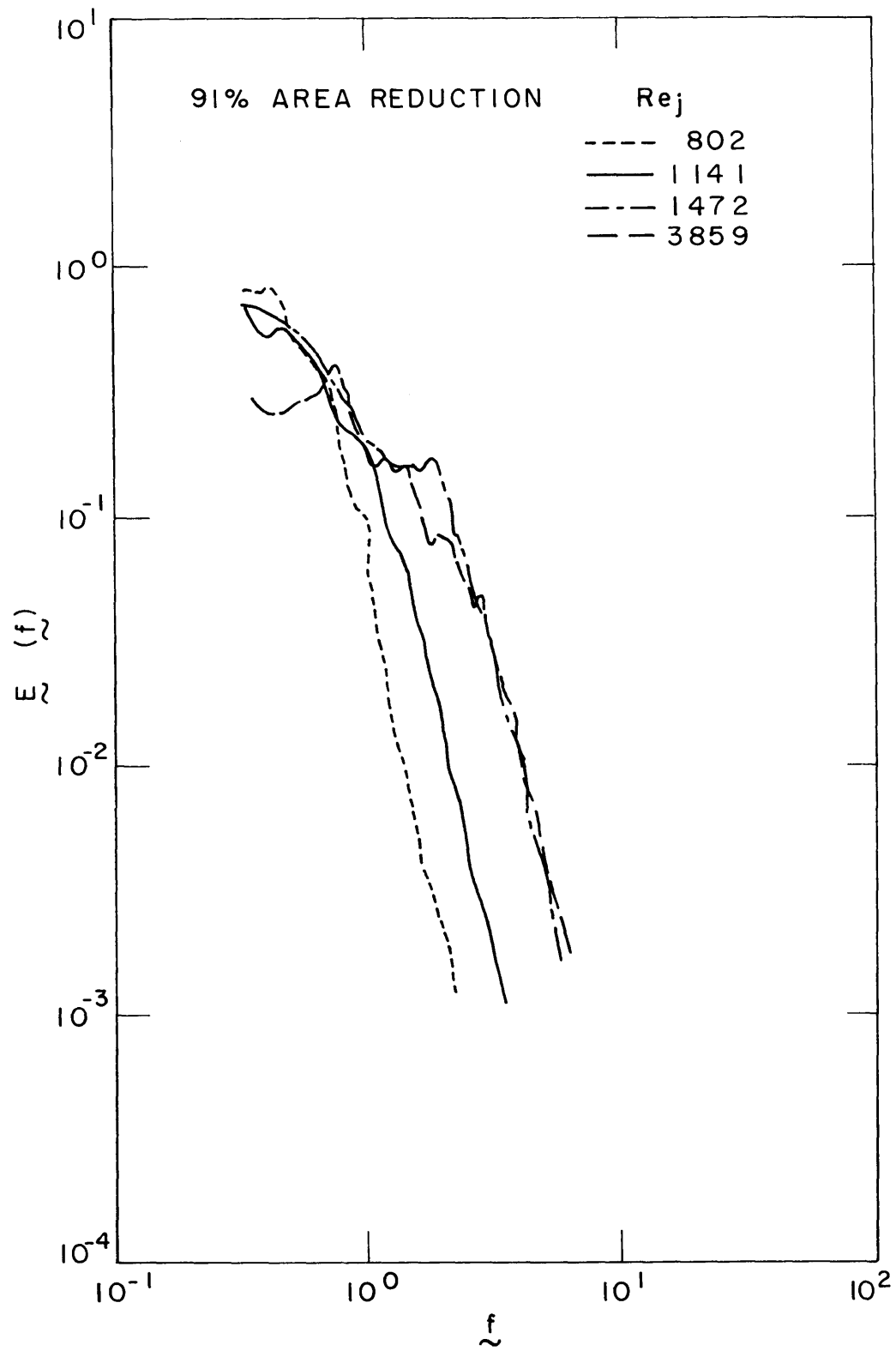


Fig. 33. Nondimensional spectral density of wall pressure for 91% area reduction.

$$E(\omega) \propto p^2 \frac{d}{U} \tag{4.2.1}$$
$$f \propto \frac{U}{d}$$

The rms value was used to normalize the spectra, rather than $p u_j^2$, because of the very strong dependence of the rms pressure on Reynolds number at low Reynolds number, which would make it difficult to put all the spectra on a single sheet of paper. Using the above normalization facilitates comparison of spectral energy distribution for flows with disparate Re_j .

If one defines

$$\tilde{E}(\omega) = \frac{E(\omega) U}{p^2 d} \tag{4.2.2}$$

$$\tilde{f} = \frac{fd}{U}$$

then

$$\int_0^\infty \tilde{E}(\tilde{f}) d\tilde{f} = 1 \tag{4.2.3}$$

The results of this normalization are shown in Figs. 29-33 for 5 diameter ratios.

A composite spectrum can be made by plotting spectra from all stenoses where the Reynolds number has become high enough so that the spectral shape is independent of Reynolds number. The shaded area in Fig. 34 represents the region in which 10 spectra from 4 stenoses lie, and is the universal high Reynolds number spectrum.

For lower Reynolds numbers a spectral normalization was made more

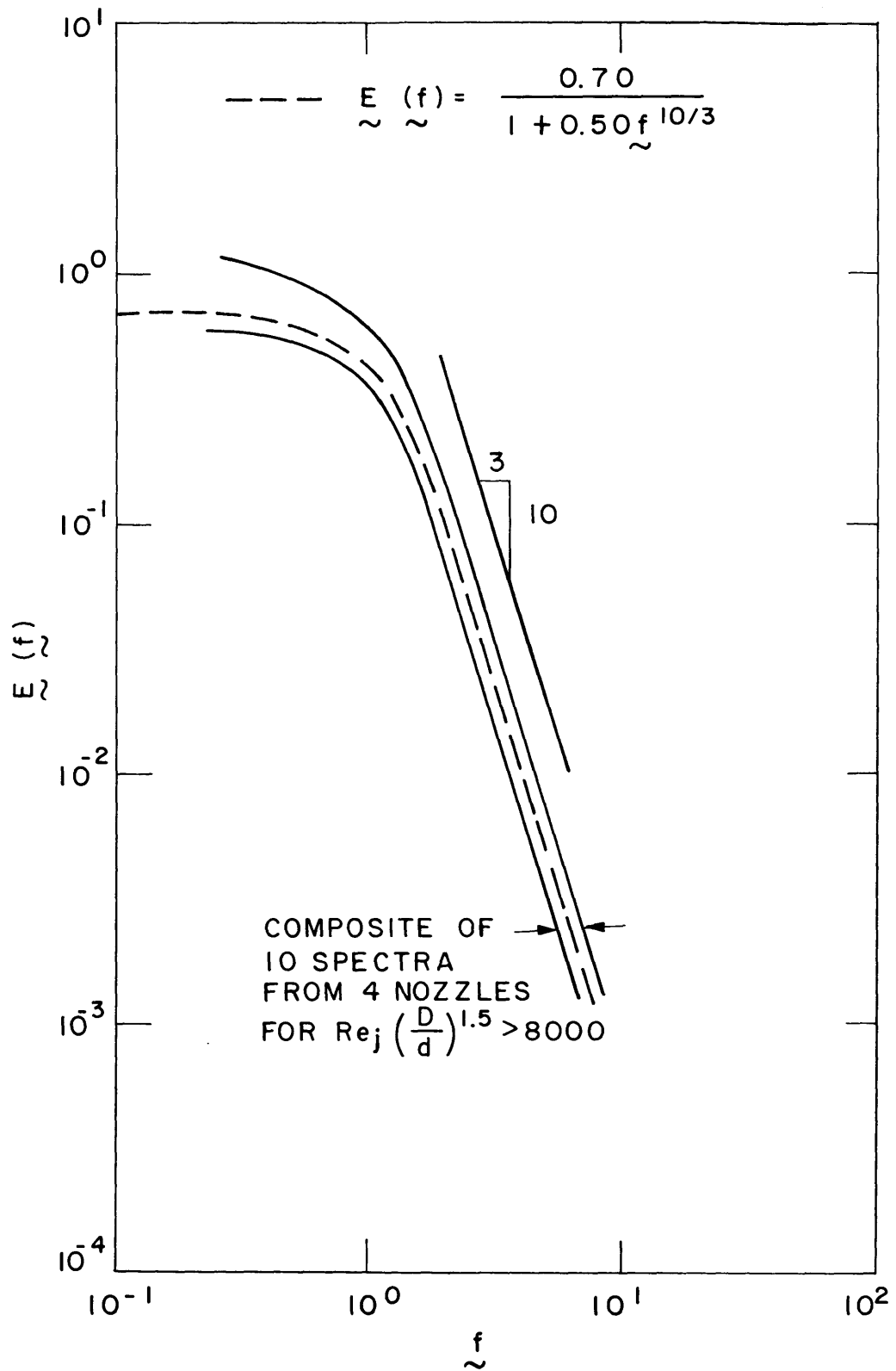


Fig. 34. Nondimensional spectral density of wall pressure for all area reductions at high Reynolds number.

difficult for two reasons. First, at lower Reynolds numbers the integrated intensity becomes quite low, as demonstrated in Fig. 26 and therefore ambient and pump noise limits the accuracy and quantity of data. Secondly, the low Reynolds number data was obtained at low flow rate, which in turn implies a low characteristic frequency of the turbulent flow ($f \sim \frac{U}{d}$). Low frequency makes signal processing more difficult for a given degree of accuracy.

However, the following observations were made from the existing data:

1. The high frequency tail of the spectra becomes steeper as Re_j decreases.
2. The value of Re_j at which Re_j becomes an important factor in spectral shape and depends upon d/D .

By cross-plotting the spectra for different diameter ratios it was found that the modified Reynolds number

$$\tilde{Re} = Re_j (D/d)^{1.5} \quad (4.2.4)$$

would reasonably normalize the spectra with different diameter ratios.

For engineering usefulness these spectra were fitted with a one parameter family of curves of the form

$$\tilde{E}(\tilde{f}) = \frac{a^{1/\gamma} \sin(\pi/\gamma)}{\pi(1 + a \tilde{f}^\gamma)} \quad (4.2.5)$$

where $a = a(\tilde{Re})$, $\gamma = \gamma(\tilde{Re})$. This family depends upon \tilde{Re} only, and integrates to unity. The question now arises of how to fit the existing data with this family of curves since a large degree of scatter, or variance exists in each low Reynolds number spectrum at low frequency.

The variance of the measured rms pressure is smaller than the

variance of the measured spectral density at an arbitrary frequency since integration is a smoothing process. Therefore, one can fit a curve through the low frequency scatter by fitting the one parameter family at high frequency and ensuring the proper integrated intensity. For example, the actual individual spectrum and the empirical correlation (Eq. 4.2.5) fit well at high frequency, and have the same total area beneath their respective curves. Therefore at lower frequency the empirical result should also be a good approximation to the spectrum.

The parameter $a(\tilde{Re})$ of Eq. (4.2.5) is tabulated in Table 1*.

Table 1

a	\tilde{Re}
53	3000
5.45	4000
1.74	5000
0.78	6000
.5	∞

The slope of the tails of the spectra was found to be a weak function of \tilde{Re} in the experimentally observable range. Furthermore, large scatter made an accurate correlation of γ with \tilde{Re} difficult. Therefore the

* The smallest value of \tilde{Re} at which reasonable signal-to-noise ratio could be obtained was $\tilde{Re} = 3000$. It should be noted that since $\tilde{Re} = Re_j (D/d)^{1.5} = Re(D/d)^{2.5}$, a diameter ratio of $D/d = 2$ (approximately a 75% area reduction) and $Re = 3000$ would correspond to a free stream Reynolds number $Re \approx 530$, which is well within the physiological range of interest.

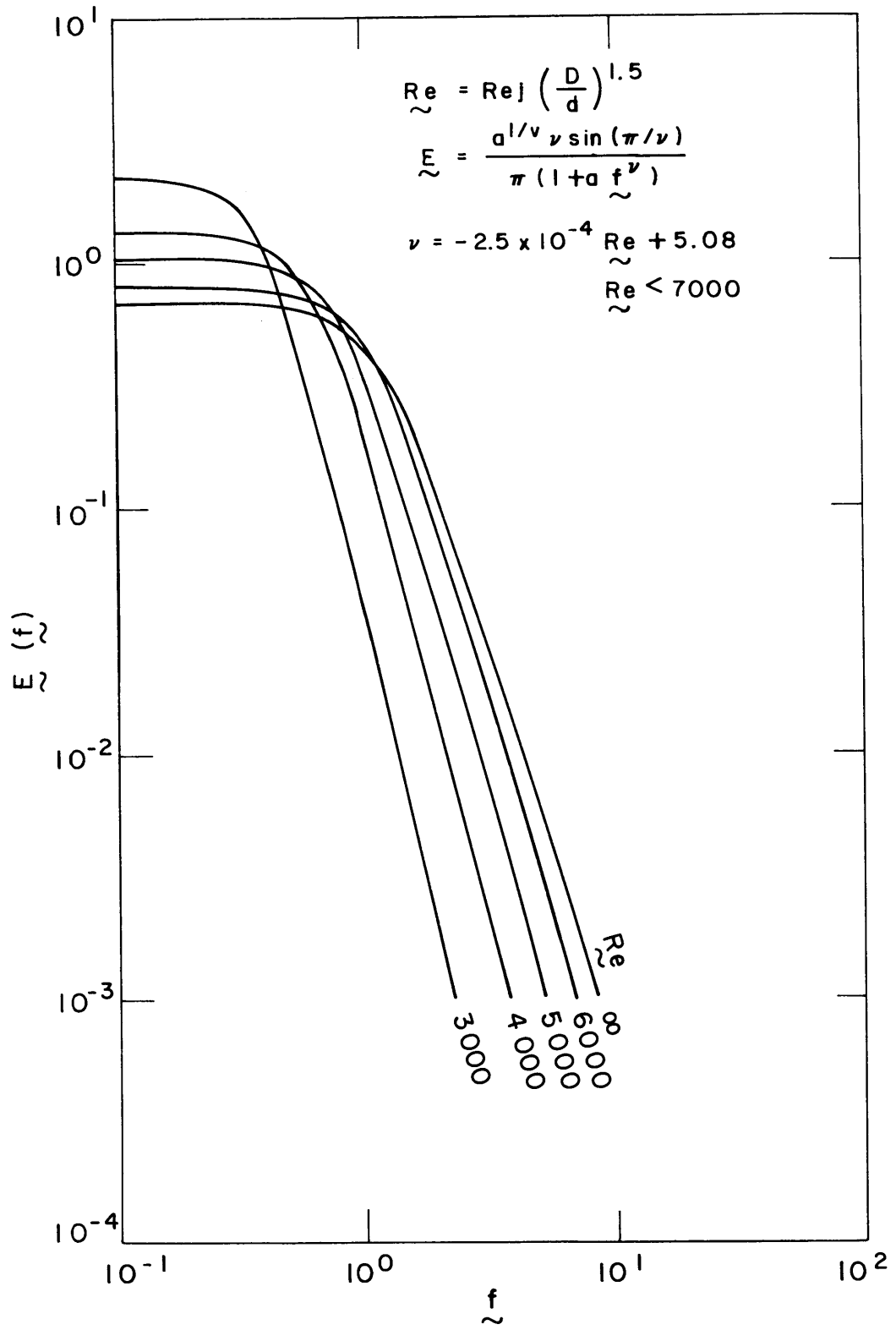


Fig. 35. A family of curves representing spectral density of wall pressure at low Reynolds number.

correlation of γ with \underline{Re} was found by cross-plotting, and was fitted with a linear approximation. Since a more detailed fit would convey a sense of accuracy that, in fact, does not exist in this data, the following correlation was used

$$\begin{aligned} \gamma(\underline{Re}) &= -2.5 \times 10^{-4} \underline{Re} + 5.08 & 3000 < \underline{Re} < 7000 \\ \gamma(\underline{Re}) &= -10/3 & \underline{Re} \geq 7000 \end{aligned} \tag{4.2.6}$$

The one parameter family of spectra is shown in Fig. 35, and is intended only as a useful engineering approximation to the truth.

4.3. Interpretation of Experimental Results

The objective of this section is to look at the results presented in the previous section, and to attempt to infer a qualitative description of the flow.

Rms Data

The dependence of peak mean square pressure on jet Reynolds number, as shown in Fig. 26, demonstrates that turbulent velocity fluctuations scale with jet velocity, at least at moderately high jet Reynolds number.

($Re_j > 2000$). As mentioned earlier, when $Re_j \leq 2000$ the mean square pressure has very strong dependence upon Re_j since the rms pressure can jump two decades as Re_j varies from 1000 to 2000.

One of the most interesting aspects of the rms pressure behavior is the distance required for p^2 to reach a maximum value. This is represented by L , is shown in Fig. 28, and leads to the following empirical law,

$$\frac{L}{d} = \frac{3 \times 10^{+4}}{Re_j} \tag{4.3.1}$$

But this result further simplifies to

$$\frac{Lu_j}{\nu} = 3 \times 10^{+4} \quad (4.3.2)$$

Figure 36 represents a replot of Fig. 28 with different coordinates.

This is an amazing result when one considers that Lu_j/ν is independent of geometry (either d or D) . It implies that if some of the jet kinetic energy is converted to turbulent motion (the amount depending on geometry), the processes which control the redistribution of this turbulent energy and its subsequent decay are not affected by the walls; before the eddies have a chance to interact with the walls, they have decayed due to inertial eddy-eddy interaction.

This geometry is similar in that respect to grid-induced turbulence in a wind tunnel, where the walls do not influence the turbulent decay. The fact that u_j is the relevant velocity again implies that the magnitude of the turbulent velocity fluctuations scale with u_j .

Unlike wind-tunnel turbulence, the observed decay does not go like x^{-1} , but falls off more rapidly (Batchelor, 1967). Even if the turbulent intensity in the pipe did follow such a law, the turbulent wall pressure fluctuations would be expected to decrease faster than x^{-1} due to the formation and growth of a boundary layer which acts as a buffer between the wall and the turbulent core.

A comparison of the characteristic length for the wall pressure fluctuations to reach a maximum to the reattachment length would be of interest. Back and Roschke (1972) report reattachment data in the Reynolds number range relevant to this work. Their data was obtained from fully

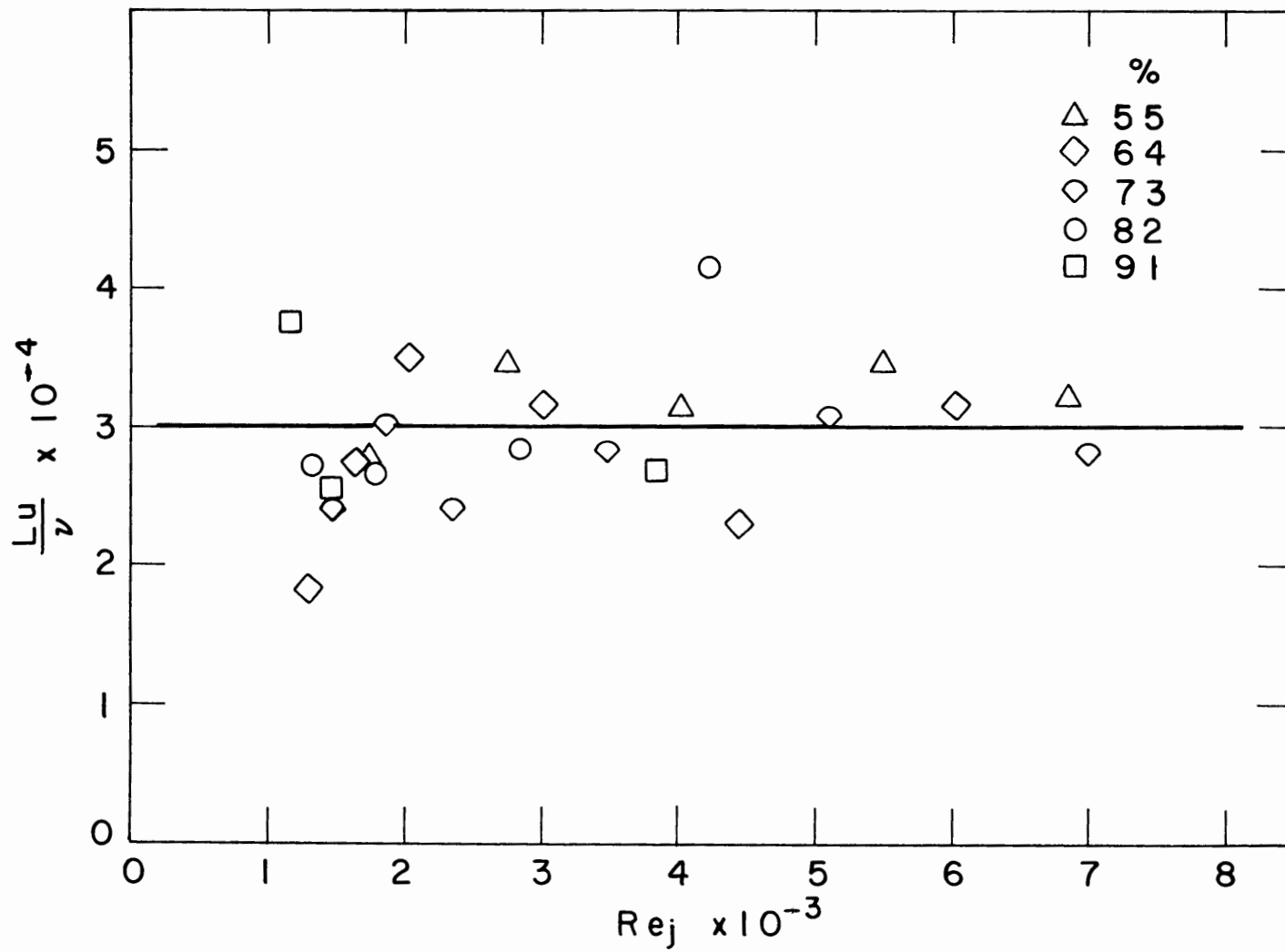


Fig. 36. Distance downstream of orifice at which spatial maximum of rms wall pressure is observed.

developed laminar flow passing through a sudden expansion. Other reattachment data can be extracted from the visual studies of Nichols (1972) and Johansen (1929), but may be subject to large error. Many other investigators have studied reattachment at lower Re_j , where L is found to be an increasing function of Re_j .

The limited amount of reattachment data in the appropriate Reynolds number range does not permit conclusive scaling of the two length scales mentioned above. The only conclusions that can be made from the data available is that the reattachment length is always smaller than the distance required for wall pressure fluctuations to reach a maximum value, with the difference decreasing as Reynolds number increases.

It was also observed that the characteristic decay length of the wall pressure tends to scale with the length L , although this was not quantified. As the jet Reynolds number increases, L becomes shorter and the jet decays more rapidly. This is consistent with the model used in Chapter II for the spatial distribution of intensity, i.e. Eq. 2.15 where $W(y_1 z_1) \propto y_1 z_1 e^{-(y_1 + z_1)/L}$, which implies at maximum intensity at $y_1 = z_1 = L$, and a decay rate proportional to L .

Spectral Data

The spectral data normalizes well for high Re_j . The scaling laws of Eq.(4.2.1) implies that: 1) the magnitude of the turbulent velocity fluctuations scale with u_j ; 2) eddy size scales with d ; and 3) eddies convect past the wall at a velocity proportion to U . Thus

$$f \sim U/d .$$

Because intensity falls off so rapidly with Reynolds number, it is difficult to obtain data at low Re_j due to poor signal/noise ratio. For Re_j on the order 1000 or less the spectral energy distribution becomes narrowed. However, it appears to be difficult to identify Re_j by spectral shape alone.

Spectral energy distribution and its integral, the total rms pressure, become Reynolds number dependent at approximately the same Reynolds number ($1000 < Re_j < 2000$) . As Re_j decreases the effective bandwidth and total intensity decrease, but the total intensity is more sensitive to Re_j than is the spectral shape.

Chapter V Conclusions

The conclusions drawn from the theory and experiment will be discussed in three sections: A) Implications for phonoangiography; B) Onset of vascular murmurs; and C) Estimates of wall shear stress.

5.1. Implications for Phonoangiography

Lees and Dewey (1970) hypothesized scaling laws for the spectral distribution of energy in a bruit. Neglecting Reynolds number and tissue transmission effects, they showed that based on these scaling laws useful information could possibly be extracted from analysis of bruits. The so-called phonoangiographic equations derived were tested by Gurll (to be published) in a series of dog experiments. Gurll exposed and banded major arteries in a number of dogs to produce localized constrictions. Both the unobstructed and obstructed diameters were measured. Flow rate through the artery of interest was measured with an electromagnetic flow meter. After closing the animal, tissue vibration at the skin surface was measured with a Hewlett Packard heart sounds microphone. Gurll performed spectral analysis on these induced bruits and compared his result with the predictions of Lees and Dewey (1970). Gurll found good qualitative agreement with these scaling laws. However, when flow rate was predicted using the phonoangiographic equations of Lees and Dewey it was found that these predictions were systematically low by a factor of two to four. As shown in the previous chapters, the scaling laws used by Lees and Dewey require modification, and tissue transmission does introduce an important modification.

The motivation of the present research was to understand "sound" generation and transmission phenomena, with application to extraction of relevant physiological measurements from physiological observables. Pursuant to this objective one must look at the results presented in the previous chapters dealing with the structure of the pressure field at the wall of a constricted tube, and look at the theory of sound transmission with an eye towards identifying characteristic phenomena or behavior that can be used to generate new quantitative relations for phonoangiographic equations.

With this in mind we shall first qualitatively describe what the spectral distribution of energy should look like in a bruit, and then briefly describe the spatial distribution of intensity at the skin surface.

From Eq. (2.20) we showed that the physiological observable $\pi(\underline{x},\omega)$ could be expressed as the product of $E(\omega)$, the spectral density of pressure at the arterial wall, and $c(\underline{x},\omega)$ the transmission correction function,

$$\pi(\underline{x},\omega) = c(\underline{x},\omega) E(\omega) \quad (5.1.1)$$

It was hypothesized that the frequency dependent part of the correction function could be approximated as a combination of asymptotic limits

$$c(\underline{x},\omega) \propto \frac{1}{1 + \frac{H}{\ell(\omega)} \cdot \frac{H}{\eta(\omega)}} \quad (2.20)$$

For turbulent pipe flow at high Reynolds number the longitudinal correlation length $\ell(\omega) \approx 0(U_c/f)$, and the lateral (circumferential) correlation length $\eta \approx \ell/5$ (Clinch, 1969). Therefore we shall assume

$$c(\underline{x}, \omega) \propto \frac{1}{1 + \beta^2 \left(\frac{fH}{u}\right)^2} \quad (5.1.2)$$

where β^2 is a constant of order unity.

For simplicity we shall assume high Reynolds number, where Reynolds number is unimportant, and \underline{E} becomes

$$\underline{E}(\underline{f}) = \frac{0.70}{1 + 0.50 \underline{f}^{3.33}} \quad (5.1.3)$$

Then from 5.1.1,2,3

$$\pi(\underline{x}, \omega) \propto \frac{1}{1 + .5 \underline{f}^{3.33}} \cdot \frac{1}{1 + \beta^2 \underline{f}^2 \left(\frac{H}{d}\right)^2} \quad (5.1.4)$$

In terms of dimensional variables this becomes

$$\pi(\underline{x}, \omega) \propto \frac{1}{1 + .5 \left(\frac{fd}{U}\right)^{3.33}} \cdot \frac{1}{1 + \beta^2 \left(\frac{fH}{U}\right)^2} \quad (5.1.5)$$

This is a particularly simple and **convenient** representation of the spectral density of a bruit. It says that the spectral density at the skin is the product of two functions, each of which has a clearly defined break frequency, i.e., a frequency at which the power law changes abruptly. We designate these frequencies as

$$f_1 = \frac{U}{\beta H} \quad (5.1.6a)$$

$$f_2 = \frac{1.2U}{d} \quad (5.1.6b)$$

Since β is of order unity and for every case conceivable $H \geq d$ one would expect

$$f_1 < f_2 \quad (5.1.7)$$

The frequency f_1 represents the frequency at which a correlation length of the turbulent pressure field equals the depth of the artery below the skin surface. The frequency f_2 represents the break frequency in $E(\omega)$, as shown in Fig. 35. Fig. 37 is a sketch of the expected spectral shape of a bruit as observed at the skin surface. If Reynolds number effects are included the slope of the high frequency tail, and f_2 are slightly variable. At low frequency ($f < f_1$) the spectrum is flat. At intermediate frequency ($f_1 < f < f_2$) the slope becomes -2 . At high frequency ($f > f_2$) the slope becomes $-2-\gamma$ ($= -5.3$ when $\text{Re} = \infty$).

At the skin surface the spatial distribution of intensity can have distinctive characteristics and can provide useful information. Thinking of the artery as a truncated line source of length L , one can imagine that if $H/L \gg 1$ the iso-intensity contours will be similar in shape to an ellipse with ratio of major to minor axis $\zeta \gg 1$. If $H/L = O(1)$ the ellipse will become rounder, and ζ will be of order unity but greater than 1. If $H/L \ll 1$, the artery appears to be a point source, and the contours of iso-intensity become a circular ($\zeta = 1$). This can be expressed functionally as

$$g\left[\frac{H}{L}, \zeta\right] = 0 \quad (5.1.8)$$

Incorporated in this equation is the fact that ζ is a strong function of H/L for $H/L < 1$, and is a very weak function of H/L for $H/L > 1$. Therefore when $H/L < 1$, ζ is a direct measure of H/L , and since $L = \text{const}/u$ (Eq.(4.3.2)) ζ is a direct measure of Hu .

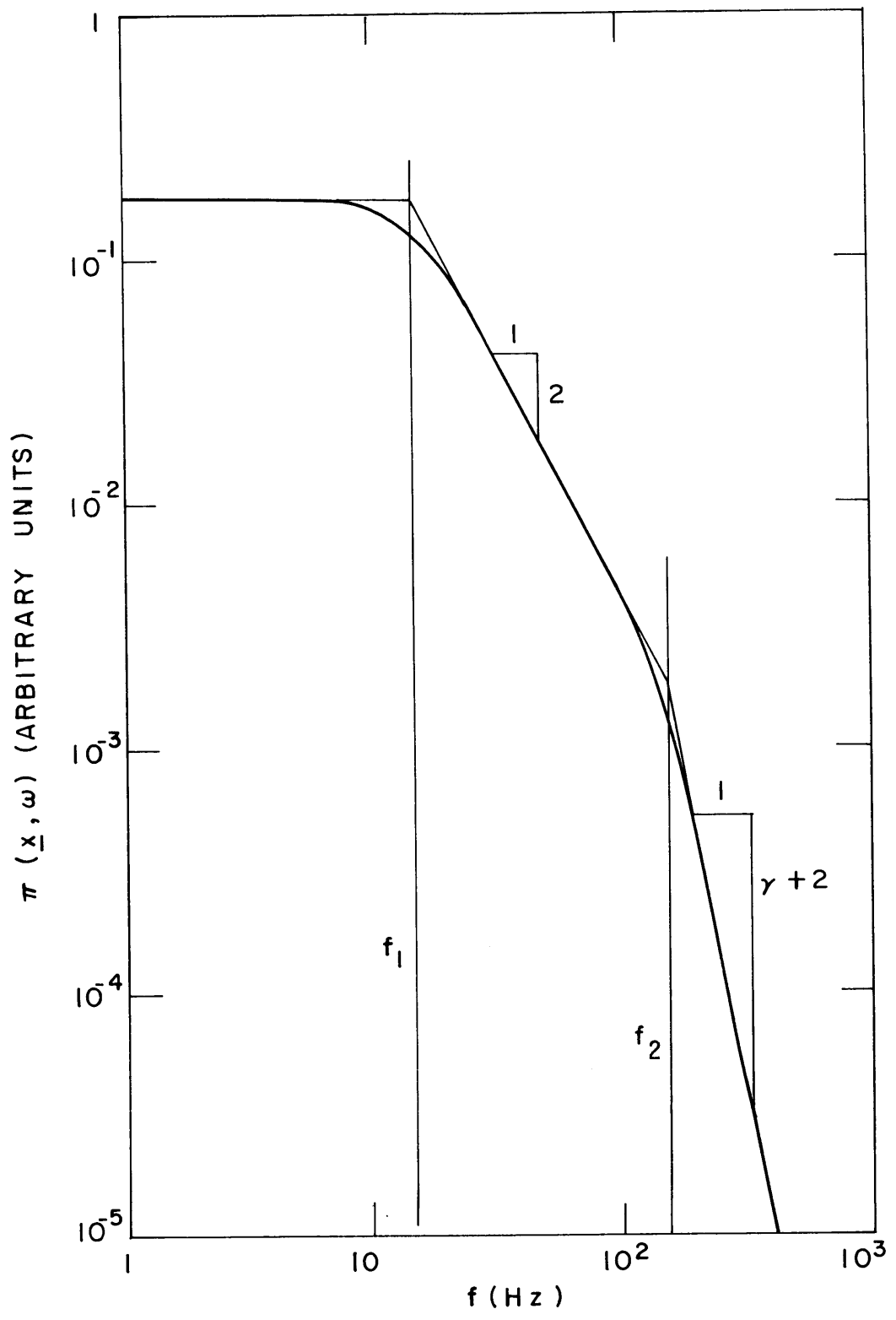


Fig.37. Idealized model of spectral density of a bruit.

Before leaving the subject of spatial intensity distribution it should be noted that the use of multiple transducers or a phased array of transducers for the purpose of scanning the artery with a device of high receptive directivity cannot succeed. The reason is that in the range of wavelength of interest in phonoangiography

$$k L_a \ll 1$$

where $k = 2\pi/\lambda$ and L_a is a typical array dimension. Since the wave lengths in the tissue are much larger than any practical array size, the array will be omnidirectional.

At this point it is advantageous to collect facts that lead to equations that might be solved for u , U , D , d .

a) A frequency exists at which the power law behavior of the wall pressure fluctuation spectra changes (Eq. 4.2.5). This occurs when

$$a \tilde{f} = a(\underline{Re}) \frac{f_2 d}{u} = 1 \quad (5.1.9a)$$

b) A frequency exists at which the transmission function changes power law dependence. This occurs when the depth of the artery approaches the correlation length, or from Eq. (5.1.2) when

$$\frac{f_1 H}{U} = 1 \quad (5.1.9b)$$

c) The slope of the spectrum at high frequency, is a unique function of \underline{Re} .

$$\gamma = \gamma(\underline{Re}) \quad (5.1.9c)$$

d) The spatial distribution of energy at the skin surface is a unique function of the depth of the artery, and the effective length

of the excitation region. This may be expressed in terms of shape factors of iso-intensity contours in the form of Eq. (5.1.8).

$$g(Hu, \zeta) = 0 \quad (5.1.9d)$$

e) The amplitude of the spectrum at the skin surface or its integral, the mean square pressure can be measured

$$\pi = E(\omega) c(\underline{x}, \omega) \quad (5.1.9e)$$

or

$$p_{rms}^2 = \int_0^{\infty} \pi d\omega = \int_0^{\infty} E(\omega) c(\underline{x}, \omega) d\omega$$

f) The continuity equation applies. The flow through the orifice is equal to the flow downstream

$$ud^2 = UD^2 \quad (5.1.9f)$$

Before proceeding one must also collect reservations and qualifications to the use of the preceding equations.

a) Equation (5.1.9c) is not well conditioned for inversion of \underline{Re} for high \underline{Re} since γ is a weak function of \underline{Re} . Small errors in measurement of γ could lead to large errors in estimation of \underline{Re} .

b) The transmission break frequency f_2 of Eq. (5.1.9b) occurs at very low frequency, on the order of 10 Hz, so unsteady effects (i.e., harmonics of the heart rate) might become important at these low frequencies. Also ambient noise such as room noise, muscle tremor, other physiological noise sources may make it impossible to make a meaningful measurement at

that low a frequency. Note that for coronary arteries $\lambda(\omega)/H \ll 1$, so f_1 will not exist. Furthermore, Eq. (5.1.2) represents nothing more than an educated guess of system transmission, and is unconfirmed by experiment. Therefore Eq. (5.1.9b), which follows from Eqs. (5.1.1), (5.1.2), and (5.1.3) is unconfirmed.

c) Eq. (5.1.9d) is not well conditioned for inversion when $H/L > 1$. Small errors in measurement of ζ would lead to large errors in estimates of H/L or H_u . Note that for coronary arteries $H/L > 1$ always.

Reservations aside for the moment, we observe that there are six equations (nonlinear) in only five unknowns. Therefore, one of the equations is redundant, but this might allow us to eliminate a single observation that is difficult to perform or measure, or subject to large error, and still solve the system of equations for all five unknowns (assuming that the system can be inverted). Therefore as a preliminary conclusion we state that total noninvasive diagnosis is possible if one is willing to work hard enough at it. The practicality of such a procedure is another question. At this point one looks for reasonable engineering tradeoffs to make the procedure simpler and more reliable. This can be accomplished by leaving out any of the six equations which are ill-conditioned for inversion, difficult to measure, or suspect for any other reason. In their stead one can supply reasonable guesses for unknowns that are not of primary interest and are reasonably well known, (such as H or D), from previous angiographic studies on that patient, from experience, or other methods.

Consider the following examples:

A. If the break frequency f_1 is unobservable and \Re cannot be obtained from inversion of $\gamma(\Re)$ with sufficient accuracy, this leaves Eqs. (5.1.9a,d,e,f). Guessing D , the unobstructed arterial diameter

leaves four equations in four unknowns.

B. If one does not want to do amplitude calibration, if $H/L > 1$ causes Eq. (5.1.9d) to be impractical, and $\gamma(\underline{Re})$ is not well conditioned, but one is willing to do analysis with very long averaging times to resolve f_1 , this leaves Eqs. (5.1.9a,b,f). Guessing H and D leaves three equations in three unknowns u, U, d .

C. If $H/L > 1$ so that surface contours are unattractive, if the low frequency break point cannot be resolved, and if $\gamma(\underline{Re})$ cannot be accurately inverted, this leaves Eqs. (5.1.9a,e,f). Guessing H and D leaves three equations in three unknowns u, U, d .

This last approach seems especially attractive since it avoids all of the serious pitfalls, and could be applied to deep arteries.

In this case the accuracy of the final predictions of the three unknown quantities would depend upon the accuracy of the estimates of H and D. Three possible approaches for estimates of H and D are:

a) Data from a previous angiogram of that patient could provide estimates of H and D with reasonable accuracy.

b) Morphological studies. Raines (1972) reports that the arterial diameter at a specific location in the lower arterial tree varies minimally from patient to patient in a group of 24 patients of normal height and weight.

c) Simple ultrasonic techniques can easily identify the depth and internal diameter of many of the major arteries of the body with good accuracy.

Of these three possibilities, the last is certainly the most reasonable since it is a direct, simple, accurate, noninvasive measure of H and D for the particular artery of the patient.

In summary, phonoangiography could in principle provide a complete noninvasive diagnosis ab initio without any additional inputs.

In practice, with minimal input of information obtained by ultrasound, it appears that phonoangiography could provide a useful clinical tool to the clinician. The phonoangiographic equations are derived in Appendix C for the case where H and D are assumed known.

5.2 Onset of Vascular Murmurs

As shown in the experimental results of Section III, the onset of turbulence induced pressure fluctuations occurs at vanishingly small values of mean square pressure (Fig. 26). Since any signal could be amplified in the absence of noise, one might conclude that the criterion for onset of detectability of vascular murmurs could be the same as the criterion for onset of pressure fluctuations. However, in all real systems the limiting factor in detectability is the signal to noise ratio. To detect a specific signal, that signal must be distinguishable from the ambient noise and noise introduced in the detection and amplification system. Establishment of a nominal threshold rms wall pressure would permit prediction of onset of detectability of a vascular murmur in a particular artery by means of Fig. 26 and an estimate of transmission loss (see Section II). The ambient noise in the location of that artery would also have to be estimated [a coronary murmur could be masked by heart sounds, while a femoral murmur of the same intensity might easily be detected]. However, this is not a practical procedure. The estimate of Sacks et al. (1971) in Eq. (3.7.1) is an oversimplification of the onset of detectability of vascular murmurs, even though it is a reasonable approximation for the onset of turbulent flow.

Many clinicians follow the rule of thumb that if a vascular murmur is audible, the artery must be at least 60% obstructed. This estimate is consistent with the experimental results found in this work, and probably represents as good a rule of thumb as possible which does not rely on detailed computations or unreliable premises.

5.3 Estimate of Mean Square Shear Stress at Arterial Wall

The fluctuating stress at the arterial wall downstream of a stenosis is thought to be a possible cause of post stenotic dilation as well as continued development of atherosclerosis (due to shear dependent mass transfer rate and/or injury to the arterial wall). The experiments reported in this work clearly define the nature of the fluctuating normal stress, but no measurements of shear stress were attempted. However, it is not unreasonable to expect the mean square shear and mean square pressure to be related to one another at the boundary of a turbulent flow. This is plausible because a) they both must depend upon the same flow parameters (Reynolds number, geometry, etc.) and thus must be dependent, or b) they are both caused by "collisions" of eddies with the wall, and on the average the normal force and shear force during such a collision will depend on the eddy trajectory and each other. Burton (Ph.D. thesis to be published, "The Connection Between Intermittent Turbulent Activity Near the Wall of a Turbulent Boundary Layer With Pressure Fluctuations at the Wall", M.I.T. Acoustics and Vibration Laboratory) found in turbulent boundary layers (with and without pressure gradients) that the ratio of the mean square pressure and mean square shear was a constant that did not vary considerably from point to point or flow to flow; given by

$$\frac{\tau_{\text{rms}}}{p_{\text{rms}}} \approx .06 \quad (5.3.1)$$

This relation would be expected to hold true to within an order of magnitude for turbulent flows in general, and therefore permits estimates of root mean square shear stress. Thus for a typical stenosed artery, $D = 5 \text{ mm}$, 85% obstructed, $U_{\text{systole}} = 50 \text{ cm/sec}$ we would expect (from Fig. 27) the maximum systolic values of rms pressure and shear to be

$$p_{\text{rms}} \approx \rho u_j^2 (2.5 \times 10^{-3}) \approx 35 \text{ dynes/cm}^2$$

$$\tau_{\text{rms}} = 2 \text{ dynes/cm}^2$$

Similar calculations could easily be repeated for other values of the parameters.

REFERENCES

- Back, L.H., Roschke, E.J., "Shear Layer Flow Regimes and Wave Instabilities and Reattachment Lengths Downstream of an Abrupt Circular Channel Expansion", J. of App. Mech., Sept. 1972, pp. 677-681.
- Bakewell, H.P., Jr., Carey, G.F., Libuha, J.L., Schloemo, H.H., Von Winkle, W.A., "Wall Pressure Correlations in Turbulent Pipe Flow", U.S.N., USL Report No. 559, 1-052-00-00, 20 Aug. 1962, AD 283683.
- Batchelor, G.K. (1967), "The Theory of Homogeneous Turbulence", Cambridge University Press, London.
- Bruns, D.L., "General Theory of the Causes of Murmurs in the Cardiovascular System", Am. J. Med., Vol. 27, p. 360 (1959).
- Caro, C.J., et al., "Arterial Wall Shear and Distribution of Early Atheroma in Man", Nature, 223, Sept. 1969, p. 1159.
- Clinch, J.M., "Prediction and Measurement of Vibration Induced in Thin Walled Pipes by Passage of an Internal Turbulent Water Flow", J. Sound Vib., (1970) 12 (4), pp. 429-451.
- Clinch, J.M., "Measurement of Wall Pressure Field for Smooth Walled Pipe Containing Turbulent Water Flow", J. Sound Vib. (1969) 9 (3), pp. 398-419.
- Corcos, G.M., "Resolution of Pressure in Turbulence, J. Acoust. Soc. Am., Vol. 35, No. 2, p. 192, (1963).
- Corcos, G.M., "The Structure of the Turbulent Pressure Field in Boundary Layer Flows", J. Fl. Mech., Vol. 18, p. 353, (1964).

- Davies, P.O.A.L. and Fisher, M.J., "Correlation Measurements in a Non-Frozen Pattern of Turbulence", J. Fl. Mech., Vol. 18, p. 97, (1964).
- Foreman, J.E.K. and Hutchinson, K.J., "Arterial Wall Vibration Distal to Stenoses in Isolated Arteries of Dog and Man", Circ. Res. Vol. 26, p. 583, (1970).
- Forrester, J.H., Young, D.F. "Flow Through a Converging-Diverging Tube and Its Implications in Occlusive Vascular Disease - I" J. Biomech., Vol. 3, p. 297 (1970).
- Franklin R.E. and Wallace, J.M., "Absolute Measurements of Static Hole Error Using Flush Mounted Transducers", J. Fl. Mech., Vol. 42:1, pp. 33-48, (1970).
- Fredberg, J.J., "Sound Generation by Turbulence at Stenoses of Human Arteries", M.S. Thesis, M.I.T. (1970).
- Frick, F.R., "Pressure Fluctuations in Separated Flows", J. Sound Vib., 17 (1), pp. 113-123, (1971).
- Fry, D.L., "Acute Vascular Endothelial Changes Associated With Increased Velocity Gradients", Circ. Res., Vol. XXII, p. 165, Feb. 1968.
- Fung, Y.C., "Foundations of Solid Mechanics, Prentice Hall, N.J., (1965).
- Garabedian, P.R., "Partial Differential Equations", John Wiley & Sons, N.Y., (1967).
- Golia, C., Evans, N.A., "Flow Separation Through Annular Constrictions in Tubes", Experimental Mechanics, Vol. 13, April 1973.
- Johansen, F.C., "Flow Through Pipe Orifices at Low Reynolds Number", Proc. Royal Soc., London, Ser. A., Vol. 126, pp. 231-245, (1929).
- Kirby, G.J., "The Effect of Transducer Size Shape, and Orientation on Resolution of Boundary Layer Pressure Fluctuations at Rigid Wall", J. Sound Vib., 10 (3), pp. 361-368 (1969).

- Klitzner, T.S., "Methods of Quantitative Analysis for Clinical Phonoangiography", M.S. Thesis, M.I.T., June 1972.
- Lees, R.S., Dewey, C.F. Jr., "Phonoangiography: A New Noninvasive Diagnostic Method for Studying Arterial Diseases", Proc. Nat. Acad. Sci., Vol. 67, No. 2, pp. 935-942, Oct. 1970.
- Lyon, R.H., Ffowcs Williams, J.E., "Sound Radiated from Turbulent Flows Near Flexible Boundaries", BBN Report No. 1054, Aug. 1963, AD 420002.
- Maybe, D.G., "Analysis and Correlation of Data on Pressure Fluctuations in Separated Flow", J. Aircraft, Vol. 9, No. 9, pp. 642-645, Sept 1972.
- McDonald, D.A., "Blood Flow in Arteries", Edward Arnold Ltd., London, 1960.
- McKusick, V.A., et al., "Spectral Phonocardiography", Johns Hopkins Hospital, Bulletin 94, 187-198, (1954).
- Mollo-Christensen, E., "Jet Noise and Shear Flow Instabilities Seen From an Experimenter's Viewpoint", J. Appl. Mech., March 1967.
- Nichol, D.S., "Measurements of Mass Transfer in Models of Atherosclerotic Arteries, M.S. Thesis, M.I.T., (1972).
- Raines, J.K., "Diagnosis and Analysis of Arteriosclerosis in the Lower Limbs From the Arterial Pressure Pulse, Ph.D. Thesis, M.I.T., (1972).
- Robbins, S.L., Bentov, I., "The Kinetics of Viscous Flow in a Model Vessel", Lab. Invest., Vol. 16, No. 6, p. 864, (1967).
- Rouse, H., Jezdinsky, V., "Fluctuation of Pressure in Conduit Expansion", J. of Hydraulics Div., Proc. of A.S.C.E., HY 3, pp 1-12, May 1966.
- Rushmer, R.G., Morgan, G., "Meaning of Murmurs", Am. J. Cardiol., Vol. 21, p. 722, (1963).

- Sacks, A.H., et al., "Criteria for the Onset of Vascular Murmurs", *Circ. Res.*, Vol. XXIX, Sept. 1971.
- Smith, R.L., Blick, E.F., Coalson, I., and Stein, P.D., "Thrombus Production by Turbulence", *J. Appl. Physiology*, Vol. 32, No. 2, Feb. 1972.
- Von Winkle, W.A., Cuthbert, J.W., Corcos, G.M., "On Measurement of Turbulent Pressure Fluctuations With a Transducer of Finite Size", *Univ. of Calif., Inst. of Eng. Research, Berkeley, Series 82, Issue No. 12*, Nov. 1959.
- Weyers, P.F.R., "Vibration and Near Field Sound of Thin Walled Cylinders Caused by Internal Turbulent Flow, NASA TND-430.
- Widnal, S.E., "Sound Radiated From Rigid Flow Spoilers Correlated With Fluctuation Forces", *J. Acoust. Soc. of Amer*, 47, 3(2), p. 924, (1970).
- Wilcutt, R.B., "Angiography: Incidence of Adverse Reactions in 282 Studies, *J. Amer. Osteopath Assn.*, Vol. 67, pp. 1414-1422.
- Willmarth, W.W., Yang, C.S., "Wall Pressure Fluctuations Beneath Turbulent Boundary Layers on a Flat Plate and A Cylinder", *J. Fl. Mech.*, Vol. 41:1, pp. 47-80.
- Willmarth, W.W., "Unsteady Force and Pressure Measurements", *Ann. Rev. Fl. Mech.*, Vol. 3, pp. 147-170, (1971).
- Willmarth, W.W., Roos, F.W., "Resolution and Structure of the Wall Pressure Field Beneath a Turbulent Boundary Layer", *J. Fl. Mech.*, Vol, 22:1, pp. 81-94, (1965).
- Wills, J.A.B., "On Convection Velocities in Turbulent Shear Flows", *J. Fl. Mech.*, Vol. 20, Part 3, p. 417.

Yellin, E.L., "Hydraulic Noise in Submerged and Bounded Liquid Jets", Biomed.

Fl. Mech., Symposium A.S.M.E., pp. 209-221, April 1966.

Young, D.F., "Effect of Time Dependent Stenosis on Flow Through a Tube",

ASME Paper No. 67-WA/BHF.

Young, D.F., Forrester, J.H., "Flow Through a Converging Diverging Tube

and Its Implications in Occlusive Vascular Disease, Parts I & II,

J. of Biomech., Vol.3, pp. 297-316, (1970).

Young, D.F., Tsai, F.Y., "Flow Through a Tube Containing an Axially-

Symmetric Constriction", Iowa State Univ., ISU-ERI-AMES-87000,

Project 843-S, Oct. 1970.

Appendix A: Exact Solution For a Cylinder of Finite Diameter

Eq. (2.13) expressed the autocorrelation of the pressure at a point in an extended medium as a result of a distributed source of force. The procedure followed in Section II assumed a line source distribution. In this appendix a cylindrical source, of radius ρ , will be considered.

The autocorrelation is given by Eq. (2.13)

$$B(\underline{x}, \tau) = \hat{E}^2 \int_{-\infty}^{\infty} \int_{-\infty}^{\infty} d\underline{y} d\underline{z} \left\{ \frac{\cos\theta_i \cos\theta'_i}{r^2 r'^2} \langle f_i(\underline{y}, t) f_j(\underline{z}, t + \tau) \rangle \right\} \quad (A.1)$$

where $f_i(\underline{y}, t)$ is the force/volume in the i th direction. On a cylinder, f_i can be expressed as

$$f_i(\underline{y}, t) = p_w(\underline{y}, t) \delta(y_2^2 + y_3^2 - \rho^2) \frac{y_i}{\sqrt{y_2^2 + y_3^2}} \quad (A.2)$$

where $p_w(\underline{y}, t)$ is the instantaneous wall pressure at the point \underline{y} on the cylinder caused by internal turbulent flow. The delta function constrains the source to the surface of an infinite cylinder of radius ρ . The term

$y_i / \sqrt{y_2^2 + y_3^2}$ represents the projection of the normal force in the i th direction. Note that the center of the cylinder is at $y_2 = y_3 = 0$.

Then

$$B(\underline{x}, \tau) = \hat{E}^2 \int_{-\infty}^{\infty} \int_{-\infty}^{\infty} dA_1 dA_2 \left\{ \frac{\cos\theta_i \cos\theta'_i}{r^2 r'^2} \frac{y_i z_i}{(y_2^2 + y_3^2)^{1/2} (z_2^2 + z_3^2)^{1/2}} \langle p(\underline{y}, t) p(\underline{z}, t + \tau) \rangle \right\} \quad (A.3)$$

where dA_1 and dA_2 are elements of area on the cylinder. Let p_w , the turbulent wall pressure be represented as

$$p_w(\underline{y}, t) = p_w(y_1, \gamma, t) \quad (\text{A.4})$$

where γ is the circumferential angle. Then the space-time correlation is given by:

$$\langle p_w(y, t) p_w(z, t + \tau) \rangle = \langle p_w(y_1, \gamma, t) p_w(z_1, \zeta, t + \tau) \rangle \quad (\text{A.5})$$

where ζ is also a circumferential angle.

Assuming angular dependence is separable, the correlation becomes

$$\langle p_w(y, t) p_w(z, t + \tau) \rangle = \theta(\gamma, \zeta) \langle p_w(0, 0, t) p_w(\Delta, 0, t + \tau) \rangle \quad (\text{A.6})$$

where W is given by Eq. (2.15), and $\theta(\gamma, \zeta)$ is a circumferential correlation function, of the form

$$\theta(\gamma, \zeta) = e^{-|\gamma - \zeta| \rho / \eta} \quad (\text{A.7})$$

if angular dependence is homogeneous. The parameter η is the circumferential correlation length. This assumes no convection in the circumferential direction.

From this point one assumes local axial homogeneity and similarity to describe $p_w(0, 0, t) p_w(\Delta, 0, t + \tau)$, and the calculation follows as in Section II. After similar asymptotic approximations as performed in Section II, the result becomes

$$\pi(\underline{x}, \omega) = \frac{(\ell/H)(\eta/H) E^2 I' E(\omega)}{1 + \left(\frac{\omega \ell}{uc}\right)^2} \quad (\text{A.8})$$

where I' represents a complicated two-fold geometrical integral. Note the dependence on the circumferential correlation length η .

If the cylinder were allowed to be close to the skin surface the asymptotic approximation would be inappropriate ($\frac{\lambda(\omega)}{H} \ll 1$), and the resulting integral would be a four-fold frequency dependent integral.

Appendix B: Effect of Transducer Size at the Skin Surface

As discussed in Chapter III, if a pressure field has spatial variations, attempts to measure the pressure at a point actually represents spatial averages over the area of the active sensing surface of the transducer. If frequencies are associated with the spatial variations (as with turbulent pressure fields) the transducer size limits the frequency response of the measuring system. This is discussed fully by Willmarth and Roos (1965).

The question that arises in physiological measurements is whether a finite transducer at the skin surface alters frequency responses in a similar fashion. For example, it is conceivable that the spatial variations in pressure at the arterial wall, when sensed at the skin surface, produce a pressure field with fine spatial structure.

Consider a semi-infinite elastic medium with a distributed source of force in a region R (See Fig. 38). Assume a coordinate system center at O , and assume that a finite rigid disc of radius r is used to sense force.

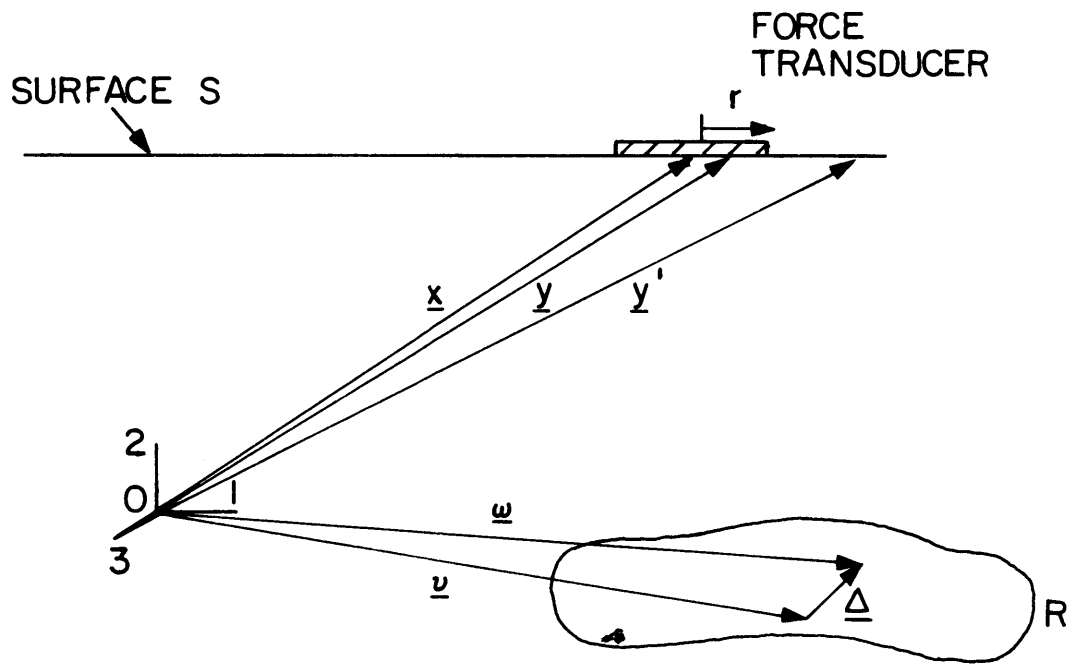


Fig.38. Excitation of a finite transducer by a source region.

Let

\underline{x} = vector from origin to center of transducer

\underline{y} = vector from origin to any point on surface S

\underline{y}' = vector from origin to any point on surface S

\underline{v} = vector from origin to any point in region R

\underline{w} = vector from origin to any point in region R

$\underline{\Delta} = \underline{w} - \underline{v}$ $d\underline{\Delta} = d\underline{w}|_{\underline{v}}$

$\underline{\zeta} = \underline{y}' - \underline{y}$

$dS(\underline{\zeta}) = dS(\underline{y}')$

$F(\underline{x}, t)$ = force exerted on stationary pressure transducer on rigid surface S . If $dS(\underline{y})$ is an element of area on the surface then

$$F(\underline{x}, t) = \int_S P(\underline{y}, t) K(\underline{x}, \underline{y}) dS(\underline{y}) \quad (B.1)$$

where $K(\underline{x}, \underline{y})$ = response Kernel = $K(\underline{x} - \underline{y})$

$$K(\underline{x} - \underline{y}) = \begin{cases} 1 & |\underline{x} - \underline{y}|^2 \\ 0 & |\underline{x} - \underline{y}|^2 > r^2 \end{cases} \quad (B.2)$$

Forming the autocorrelation function of F

$$\langle F(\underline{x}, t) F(\underline{x}, t + \tau) \rangle = \int_S dS(\underline{y}) \int_S dS(\underline{y}') \{ K(\underline{x} - \underline{y}') K(\underline{x} - \underline{y}) \langle P(\underline{y}, t) P(\underline{y}', t + \tau) \rangle \} \quad (B.3)$$

Due to appropriate Green's function and pressure doubling

$$P(\underline{y}, t) = \hat{2E} \int_{\underline{v}} \frac{f_i(\underline{v}, t) \cos \theta_i}{|\underline{y} - \underline{v}|^2} d\underline{v} \quad (B.4)$$

where \hat{E} represents elastic constants as in Chapter 2, and

$$\cos\theta_i = \frac{dr}{dx_i} = \frac{y_i - v_i}{|\underline{y} - \underline{v}|} = l_i \quad (B.5)$$

Then

$$F(\underline{x}, t) F(\underline{x}, t + \tau) > = \int_S ds(\underline{y}) \int_S ds(\underline{y}') \int_{\underline{v}} d\underline{v} \int d\underline{w} \left\{ \frac{K(\underline{x}-\underline{y})K(\underline{x}-\underline{y}') l_i l_j}{|\underline{y}-\underline{v}|^2 |\underline{y}'-\underline{w}|^2} \right\} \quad (B.6)$$

$$4\hat{E}^2 < f_i(\underline{v}, t) f_j(\underline{w}, t + \tau) > \}$$

Eliminating \underline{y}' and \underline{w}

$$\begin{aligned} < F(\underline{x}, t) F(\underline{x}, t + \tau) > = 4\hat{E}^2 \int_S ds(\underline{y}) \int_S ds(\underline{\zeta}) \int_{\underline{v}} d\underline{v} \int_{\underline{\Delta}} d\underline{\Delta} \left\{ \frac{K(\underline{x}-\underline{y})K(\underline{x}-\underline{y}-\underline{\zeta}) l_i l_j}{|\underline{y}-\underline{v}|^2 |\underline{y}+\underline{\zeta}-\underline{v}-\underline{\Delta}|^2} \right. \\ & \cdot < f_i(\underline{v}, t) f(\underline{v} + \underline{\Delta}, t + \tau) > \} \end{aligned} \quad (B.7)$$

Taking the temporal Fourier Transform

$$\pi_F(\underline{x}, \omega) = 4\hat{E}^2 \int_S dS(\underline{y}) \int_S dS(\underline{\zeta}) \int_{\underline{v}} d\underline{v} \int_{\underline{\Delta}} d\underline{\Delta} \left\{ \frac{K(\underline{x}-\underline{y})K(\underline{x}-\underline{y}-\underline{\zeta})}{|\underline{y}-\underline{v}|^2 |\underline{y}+\underline{\zeta}-\underline{v}-\underline{\Delta}|^2} \Gamma(\underline{v}, \underline{\Delta}, \omega) \right\} \quad (B.8)$$

where $\Gamma(\underline{v}, \underline{\Delta}, \omega)$ is the cross spectral density, and π_f = spectral density of force. Applying the same line model as before, with the same assumptions (see Chapter II)

$$\Gamma(\mathbf{v}_1, \Delta_1, \omega) = \phi(\omega) e^{-|\Delta|/\ell} \cos\left(\frac{\omega\Delta}{u_c}\right) W(\mathbf{v}_1, \mathbf{v}_1 + \Delta) \quad (\text{B.9})$$

which is the Corcos similarity hypothesis.

Asymptotically, as ℓ/H becomes very small, Eqs. (B.8) and (B.9) can be evaluated, and become

$$\pi_f(\underline{x}, \omega) = \frac{\hat{2}\phi(\omega)(\ell/L)}{4E \left[1 + \left(\frac{\omega\ell}{u_c}\right)^2\right]} \int_S dS(\underline{y}) \int_S dS(\underline{\zeta}) \int_0^\infty dv_1 \left\{ \frac{K(\underline{x}-\underline{y})K(\underline{x}-\underline{y}-\underline{\zeta})}{|y-\underline{v}|^2 |y+\underline{\zeta}-\underline{v}|^2} \ell_i \ell_j W(\mathbf{v}_1, \mathbf{v}_1) \right\} \quad (\text{B.10})$$

But the integrals are independent of frequency. Therefore the frequency dependence is the same as that found in Chapter II for an ideal point transducer.

This should not be unexpected because

- a) Integration is a smoothing process.
- b) The dipoles have sufficient beam width that the pressure at the two points on the transducer have nearly the same source function (i.e., the pressure at the two points depends on nearly the same region in the source).

Appendix C: Formulation of Phonoangiographic Equations

In Chapter five it was suggested that the most reasonable set of equations for phonoangiographic procedure would be continuity, frequency scaling, and amplitude scaling. In addition, the depth of the artery, H , and the unobstructed diameter D would be obtained by other means. In this appendix the actual phonoangiographic amplitude scaling equation will be derived and used to solve for the unknowns, u , U , d .

In Chapter II it was shown that

$$\pi(\underline{x}, \omega) = \frac{4E^2}{L^2} c(\underline{x}, \omega) \phi(\omega) \quad (2.20)$$

Assuming $\ell(\omega)/H \ll 1$, it was also shown that

$$c(\underline{x}, \omega) = \frac{2(\ell/H)LH I}{1 + \frac{\omega\ell}{u_c}} \quad (2.21)$$

The following observations are made:

$$\phi(\omega) \propto E(\omega) \eta D \quad (C.1)$$

$$\frac{\omega\ell}{u_c} = \text{const} \quad (C.2)$$

and from Fig. 7

$$\frac{I(H/L)^3}{\alpha^2} \approx \frac{1}{1 + H/L} \quad (C.3)$$

As suggested in Chapter II, we set $\alpha = e/L$. From empirical results (Chapter IV)

$$\frac{Lu}{\nu} = 3 \times 10^4 \quad (4.3.2)$$

and from Clinch (1969)

$$\eta \ell \propto \frac{U^2}{f^2} \quad (C.4)$$

Then the spectral density of pressure at the skin surface becomes

$$\pi = \frac{K U^2 D E(\omega)}{f^2 H^3 \left(1 + \frac{Hu}{3 \times 10^4 \nu}\right)} \quad (C.5)$$

where K is a constant to be determined empirically in vivo. K can include the system gain and elastic constants. Assuming high Reynolds number, from Fig. 37

$$E(\omega) = \tilde{E}(\tilde{f}) \frac{p_d^2}{U} = \frac{p_d^2}{U} \cdot \frac{0.70}{1 + 0.5 \left(\frac{fd}{U}\right)^{3.33}} \quad (C.6)$$

and, at high Re from Eq. 4.1.1

$$p^2 \propto \rho^2 u^4 \quad (C.7)$$

Then with continuity (C.5) becomes

$$\pi = \frac{K \rho^2 d^3 u^5}{f^2 H^3 D \left(1 + \frac{Hu}{3 \times 10^4 \nu}\right) \left(1 + 0.5 \left(\frac{fd}{U}\right)^{3.33}\right)} \quad (C.8)$$

Clearly it would be difficult to solve (C.8) for u due to the complicated nonlinearity. If we restrict our attention to carotids or femorals, then

$$\frac{H}{L} = \frac{Hu}{3 \times 10^4 v} < 1 \quad (C.9)$$

Clearly, for deep arteries the converse argument can be made that

$\frac{H}{L} \gg 1$, which also leads to simplification. Then $Hu/3 \times 10^4 v$ can be

ignored with respect to unity with small error. Thus

$$\pi = \frac{K \rho^2 d^3 u^5}{f_H^2 D^3 (1 + 0.5(\frac{fd}{U})^{3.33})} \quad (C.10)$$

Arbitrarily, we perform the amplitude scaling of the spectral density at a frequency, defined as f_3 , which falls above the transmission break frequency, but below the break frequency in the wall pressure spectrum. This is easily done by measuring the amplitude at the point where the spectrum of the bruit has a slope of -2. Then (C.9) becomes

$$\pi(f_3) = \frac{K d^2 u^3}{f_3^2 H^3 D} \quad (C.11)$$

Then, with continuity

$$ud^2 = UD^2 \quad (C.12)$$

and frequency scaling

$$\frac{f_2 d}{U} = 1 \quad (C.13)$$

a simple set of equations is obtained. Letting

$$A = \frac{K\rho^2}{f_3^2 H^3 D} \quad (C.14)$$

where K, ρ, f_3^2, H, D are all known, the system can be solved:

$$d = A^{1/2} D^5 f_2^{5/2} \pi^{-1/2}(f_3) \quad (C.15)$$

$$U = A^{1/2} D^5 f_2^{7/2} \pi^{-1/2}(f_3) \quad (C.16)$$

$$u = A^{1/2} D^7 f_2^{7/2} d^{-2} \pi^{-1/2}(f_3) \quad (C.17)$$

which are the phonoangiographic equations to be applied in the clinic.

Biographical Sketch

The author was born in Newton, Massachusetts in June, 1946. He attended public school in the Boston school system, and graduated from English High School in 1964. He then attended Tufts University from 1964 to 1968, receiving a B.S.M.E., and M.I.T. from 1968 to 1969 and 1970 to 1973 receiving the S.M.M.E., M.E., and Ph.D. degrees. The year 1969-1970 was spent in active military service.

The author was married to Ellen Orkin in 1968, and has two children, Joshua and Sheryl.

The author is now employed by Cambridge Collaborative, Inc., a research and consulting firm in the area of acoustics and applied mechanics.